# SIMULTANEOUS CHARGING AND DISCHARGING OF A LATENT HEAT ENERGY STORAGE SYSTEM FOR USE WITH SOLAR DOMESTIC HOT WATER

by

Robynne Murray

Submitted in partial fulfilment of the requirements
for the degree of Master of Applied Science

at

Dalhousie University
Halifax, Nova Scotia
July 2012

DALHOUSIE UNIVERSITY

DEPARTMENT OF MECHANICAL ENGINEERING

The undersigned hereby certify that they have read and recommend to the Faculty of Graduate Studies for acceptance a thesis entitled "Simultaneous Charging and Discharging of a Latent Heat Energy Storage System for Use with Solar Domestic Hot Water" by Robynne Murray in partial fulfilment of the requirements for the degree of Master of Applied Science.

Dated: July 26, 2012

Supervisor: _____

Readers: _____

_____

DALHOUSIE UNIVERSITY

DATE: July 26, 2012

AUTHOR: Robynne Murray

TITLE: Simultaneous Charging and Discharging of a Latent Heat Energy Storage System for Use with Solar Domestic Hot Water

DEPARTMENT OR SCHOOL: Department of Mechanical Engineering

DEGREE: MASc CONVOCATION: October YEAR: 2012



_____

Signature of Author

*To my parents, Mike and Roya Murray, and to my loving partner and best friend Braden Murphy. Thank you for your loving support and encouragement, and for always believing in me.*

# Table of Contents

## List of Tables

## List of Figures

## Abstract

Sensible energy storage for solar domestic hot water (SDHW) systems is space consuming and heavy. Latent heat energy storage systems (LHESSs) offer a solution to this problem. However, the functionality of a LHESS during simultaneous charging/discharging, an operating mode encountered when used with a SDHW, had not been studied experimentally.

A small scale vertical cylindrical LHESS, with dodecanoic acid as the phase change material (PCM), was studied during separate and simultaneous charging/discharging. Natural convection was found to have a strong influence during melting, but not during solidification. During simultaneous operation heat transfer was limited by the high thermal resistance of the solid PCM. However, when the PCM was melted, direct heat transfer occurred between the hot and cold heat transfer fluids, indicating the significance of the PCM phase on heat transfer in the system. The results of this research will lead to more optimally designed LHESS for use with SDHW.

# List of Abbreviations and Symbols Used

## *Dimensional Variables*

| | |
|---|---|
| $A$ | Heat transfer surface area ($m^2$) |
| $C_p$ | Heat capacity (J $kg^{-1}$ $K^{-1}$) |
| $h$ | Convection coefficient ( W $m^{-2}$ $K^{-1}$) |
| $k$ | Thermal conductivity (W $m^{-1}$ $K^{-1}$) |
| $m$ | Mass (kg) |
| $\dot{m}$ | Mass flow rate (kg $s^{-1}$) |
| $\rho$ | Density (kg $m^{-3}$) |
| $Q$ | Energy (kJ) |
| $\dot{Q}$ | Power (W) |
| $Q''$ | Heat Flux (W $m^{-2}$) |
| $R$ | Distance from center-point of LHESS (cm) |
| $t$ | Time (s) |
| $T$ | Temperature (K) |
| $V$ | Velocity (m $s^{-1}$) |

## *Greek Letters*

| | |
|---|---|
| $\delta$ | Uncertainty |
| $\Delta h_m$ | Latent heat of fusion (J $kg^{-1}$) |
| $\Delta T$ | Temperature difference (K) |
| $\mu$ | Viscosity (Pa s) |

## *Subscripts*

| | |
|---|---|
| $f$ | Final |
| $i$ | Initial |
| $l$ | Liquid |
| $m$ | Melting |
| $s$ | Solid |

## *Abbreviations*

| | |
|---|---|
| LHESS | Latent Heat Energy Storage System |
| HTF | Heat Transfer Fluid |
| PCM | Phase Change Material |
| SDHW | Solar Domestic Hot Water |
| TES | Thermal Energy Storage |

## *Definitions of non-dimensional variables*

| | |
|---|---|
| Nu | Nusselt number ($hD/k$) |
| Pr | Prandtl number ($C_p\mu/\ k$) |
| $Re_D$ | Reynolds number ($\rho DV/\mu$) |
| Ste | Stefan number ($C_p\Delta T/\Delta h_m$ ) |

## Acknowledgements

Foremost I would like to thank my supervisor Dr. Dominic Groulx for his guidance and encouragement. I also greatly appreciate the time, effort and support of my committee members Dr. Mary Anne White and Dr. Lukas Swan.

Thank you to the Department of Mechanical Engineering and to Angus McPherson, Mark MacDonald, Albert Murphy and Peter Jones for their time and patience. Their knowledge and expertise were greatly appreciated. Thank you also to Michelle Tougas for always being a supportive and encouraging friend and for proof-reading my work.

This research would not be possible without the generous funding from Natural Sciences and Engineering Research Council of Canada (NSERC), Dalhousie Research in Energy, Advanced Materials, and Sustainability (DREAMS) and Canada Foundation for Innovation (CFI).

# Chapter 1 Introduction

The subject of this thesis is an experimental investigation of a latent heat energy storage system (LHESS) with simultaneous charging and discharging. The experimental system was designed to replicate how a LHESS would function when used with a solar domestic hot water (SDHW) system for thermal energy storage (TES). This thesis includes a description of the experimental LHESS, the theory behind latent energy storage, as well as experimental testing and analysis of the test results.

## *1.1 Background*

Solar thermal for domestic hot water heating is one of the most cost effective and efficient areas of renewable energy exploitation. A SDHW system collects energy when solar radiation is available, and exchanges this energy to preheat domestic water for use in a building when there is a demand for hot water. However, the mismatched energy availability and demand of SDHW systems is a problem which needs to be addressed (Liu et al., 2006a). TES is commonly used to bridge this gap between energy availability and demand. Commonly used sensible energy storage systems, such as hot water storage tanks, require significant space and add weight to structural components. These space and weight requirements are a barrier to further deployment of SDHW in buildings with limited space or structural limitations to additional weight. These problems are especially prevalent when adding SDHW systems to existing buildings. Using phase change materials (PCMs) for TES can solve this problem by reducing the weight and space required for energy storage (Mehling & Cabeza, 2008). PCMs are used as energy storage mediums: energy is stored during melting and released during solidification. From an energy efficiency point of view, PCM storage systems (also called LHESS) have the advantage that their operation can be nearly isothermal (Fernandez et al., 2010).

TES can be broken into sensible and latent energy storage. Sensible energy is stored when the temperature of a material rises, and is released when the temperature of a material decreases. Sensible heat ($Q_{sensible}$) is proportional to the specific heat capacity of the material ($C_p$), the difference in temperature of the material from the initial temperature ($T_i$) to the final temperature $(T_f)$, and the mass of material ($m$) given by:

$$Q_{sensible} = mC_p(T_f - T_i). \tag{1.1}$$

Latent heat is absorbed or released when a material undergoes a change of phase at a relatively constant temperature; these materials are called PCMs. The amount of latent heat stored in a material ($Q_{latent}$) is proportional to the latent heat of fusion of the material ($\Delta h_m$) and the mass of material that undergoes a phase transition($m$) given by:

$$Q_{latent} = m\Delta h_m. \tag{1.2}$$

PCMs also store sensible heat before and after the phase transition, therefore the total storage capacity of a LHESS from an initial temperature, $T_i$, to a final temperature, $T_f$, is given by (Sharma et al., 2009):

$$Q_{PCM} = m\{C_{ps}(T_m - T_i) + \Delta h_m + C_{pl}(T_f - T_m)\}. \tag{1.3}$$

where $C_{ps}$ is the specific heat of the solid PCM, $T_m$ is the melting temperature of the PCM, and $C_{pl}$ is the specific heat of the liquid PCM. Over the small temperature range seen in most LHESS (20 to 60 ºC temperature difference), the latent heat of some PCMs is several orders of magnitude larger than the specific heat, and many PCMs can store up to 14 times more energy per volume than water over the same temperature range (Agyenim et al., 2010). Figure 1.1 shows a simple schematic of a LHESS used with a SDHW system.

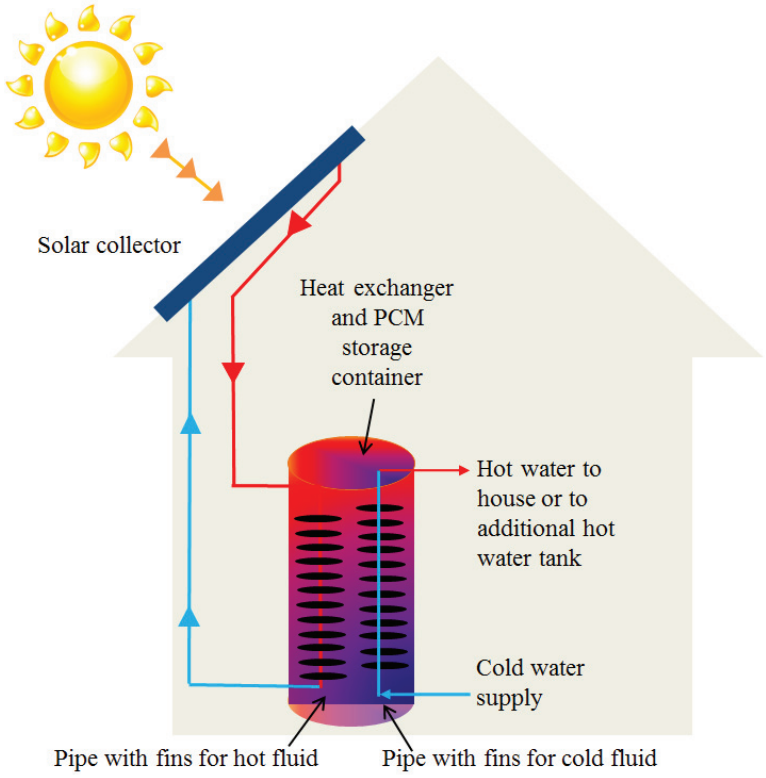


**Figure 1.1: Schematic of SDHW system with a LHESS**

The system shown in Fig. 1.1 consists of hot and cold heat transfer fluid (HTF) pipes which pass through a PCM inside a storage container. The hot HTF pipe carries the energy collected from the solar collector, and the cold HTF carries domestic water which is to be heated for use in the building. Available solar energy and hot water demands of residential homes are both time dependent and intermittent, however the energy source and demand times do not often match each other. For example, there may be a demand for domestic hot water at night when no solar energy is available. For this reason, a LHESS paired with SDHW has three possible operating modes:

1) Heat exchange from the hot HTF to the PCM, melting the PCM and charging the LHESS;
2) Heat exchange from the PCM to the domestic water, solidifying the PCM and discharging the LHESS;

3) Both 1) and 2) at the same time: Heat exchange from the hot HTF to the PCM, and heat exchange from the PCM to the domestic water at the same time, resulting in simultaneous charging and discharging.

The third operating mode occurs when there is a demand for domestic hot water at the same time that solar energy is available. Although charging and discharging is simultaneous in this operating mode, the time scales may differ, with charging times of 6 to 8 hours (*i.e.* sunshine hours) and discharging times as short as 10 minutes (*i.e.* a shower). This simultaneous operating mode makes the system suitable for various time dependent energy sources, such as solar energy (Liu et al., 2006b). Direct heat transfer from the solar HTF to the domestic water may occur during the third operating mode, with additional energy being stored in, or recovered from, the PCM.

### *1.2 Objectives*

There has been significant research done on LHESS, as will be shown in Chapter 2, however, missing from previous work is an experimental LHESS which can be used to study the simultaneously charging and discharging operating mode. This has led to the following research objectives for this project:

1) Study the heat transfer processes and phase change behavior of a PCM inside a LHESS under various modes of operating, including simultaneous charging and discharging. This includes investigating direct heat exchange from the solar HTF to the domestic water. Studying the phase change behavior of a PCM as well as the heat transfer processes of importance within a LHESS during simultaneous charging/discharging will be a contribution to the state of knowledge.
2) Study the effect of operating parameters, such as inlet HTF flow rates, on melting and solidification. This will lead to continuing development of a well-functioning LHESS.

3) Compare the experimental energy storage capacity of the PCM to the theoretical energy storage capacity. This will give an indication of how the system is functioning in comparison to theoretical expectations.
4) Compare experimental results to a reference 2D finite element numerical model of the system that has only conduction heat transfer. This simplified numerical model can be used as a starting point for future researchers to create a validated numerical model of the system.

All of these objectives aim to produce experimental data that can be used by other researchers in the future to validate a comprehensive numerical model of this system. Having an accurate numerical model of this system will lead to less time consuming and expensive optimization of LHESS designs. The outcome of an optimally designed LHESS is reduced space and weight requirements for energy storage in a SDHW system, as compared to common sensible energy storage systems.

### *1.3 Scope of Thesis*

Chapter 2 presents a literature review that includes geometries and materials used in LHESS, and experimental parameters for operating these systems. Heat transfer enhancement designs and their impact on melting and solidification are also presented. This chapter shows that there have been many experimental and numerical studies regarding the consecutive charging/discharging operating mode of a LHESS. However, no work has been published on the *simultaneous* charging/discharging operating mode. This literature review has led to an informed decision on the design of the experimental LHESS used in this thesis. The geometry of the container, heat transfer enhancement designs, equipment used in the experimental setup and experimental procedures are given in Chapter 3.

Chapter 4 presents the theory behind the theoretical and experimental energy storage calculations for the LHESS used in this thesis and the treatment of uncertainty associated with these calculations. This chapter also presents the method for calculating heat losses through the LHESS outer wall, and forced convection coefficients associated with various HTF flow rates.

Chapter 5 presents the results for consecutive charging/discharging of the LHESS. In this chapter it is shown that the experimental setup produces repeatable results and that symmetry is observed in the system. Chapter 6 presents the results obtained during simultaneous charging/discharging of the experimental LHESS. In both Chapter 5 and Chapter 6 experimental results are analyzed, and patterns in the PCM behavior are identified.

Concluding remarks and recommendations on future work are presented in Chapter 7.

Appendix A presents calibration data for the thermocouples used at the inlets/outlets of the HTF pipes, and Appendix B presents the calculations behind choosing a circulator for the hot HTF. Appendix C presents the circuit diagram used for the flow meters, and Appendix D presents temperature plots for additional experiments which show similar patterns to those presented in Chapter 6, and may be of interest to future researchers. Appendix E shows an example calculation of the energy input by the hot HTF and the uncertainty in this energy input for the first five minutes of a charging experiment.

# Chapter 2 Literature Review

Many researchers have shown the advantages of using PCMs for energy storage. Previous work has resulted in improved LHESS container geometries and heat transfer enhancement designs. LHESS operating parameters, such as flow rates and temperatures of HTFs, have been explored as well using both numerical and experimental studies. Previous work published on LHESS has guided the design of the experimental LHESS used in this thesis. As well, this literature review clearly demonstrates the need for experimental work in studying the simultaneous charging and discharging mode of a LHESS for use with a SDHW system.

## *2.1 Introduction to Heat Transfer in a Latent Heat Energy Storage System*

Better understanding of the heat transfer characteristics of a PCM inside a LHESS will lead to more efficient energy storage as a result of better LHESS designs. Heat transfer accompanied by a change of phase can be classified into three modes: conduction-controlled phase change, convection-controlled phase change, and conduction and convection-controlled phase change. Conduction has been shown to be the main heat transfer mode during solidification, and convection the main mode during melting (Agyenim et al., 2010; Jegadheeswaran & Pohekar, 2009). As well, conduction is the main mode of heat transfer early in the melting process, and is replaced by convection only once gravity effects become significant (Khodadadi & Zhang, 2001).

## *2.2 Phase Change Material Properties and Selection*

PCMs are the backbone of LHESS design, and can be broken into organic and inorganic PCM types. Organic materials, including fatty acids and paraffins, are the most commonly studied materials for PCM energy storage. Organic materials are known for congruent melting, or melting and freezing repeatedly without phase segregation or degradation of their thermal and material properties. They also self-nucleate, meaning they crystallize with little or no sub-cooling and are generally not corrosive (Sharma et al., 2009). Sub-cooling occurs when the liquid PCM reaches a

temperature below the solidification temperature before crystallizing. Paraffin wax PCMs were found to have good thermal stability after repeated cycling using a DSC, showing little to no degradation of the latent heat and phase transition temperature ranges (Zalba et al., 2003). Dodecanoic acid (also called lauric acid) has been shown to have a melting temperature range that is suitable for a LHESS used for SDHW energy storage (40 to 50 ºC for a SDHW system) (Murray et al., 2011). It also has stable thermal properties, is safe for use with domestic water, and is readily available and relatively inexpensive (Desgrosseilliers et al., 2012).

Inorganic PCMs, which include salt hydrates, have a volumetric thermal storage density higher than most organic compounds due to higher latent heat and density. As well, salt hydrates go through relatively small volume changes during melting (Kenisarin & Mahkamov, 2007). However, most salt hydrates have poor nucleating properties which results in sub-cooling of the liquid PCM prior to freezing (Abhat, 1983). In some cases, a small amount of sub-cooling may not be an issue, however, large amounts of sub-cooling which are seen in some inorganic PCMs are a problem for some systems (Farid, 2004). Also, thermal cycling studies using a DSC showed that inorganic PCMs have a high level of deviation of thermal properties from their quoted and experimental properties (Shukla et al., 2009).

PCM selection for LHESS depends on the desired application of the system. Some criteria for choosing a PCM are as follows (Abhat, 1983; Agyenim et al., 2010; Harald & Cabeza, 2008):

- Melting point in the desired temperature range for the application to assure storage and release of heat at a useful temperature;
- High latent heat of fusion to achieve high storage density;
- High specific heat so that sensible heat storage effects may play a role;
- High thermal conductivity;
- Small volume changes during phase transition;

- Exhibit little or no sub-cooling during solidification;
- Possess chemical stability, no chemical decomposition and no destructive corrosion of materials used in the LHESS;
- Contain no poisonous, flammable or explosive elements;
- Reasonable price and easily accessible.

Based on the above criteria, a PCM can be selected that meets all or most of the requirements for a LHESS. However, the selection of a PCM for a SDHW system should be done carefully in order to produce hot water in an acceptable range of temperatures, and to minimize safety concerns (such as PCM leaking into the building water supply) in the event of an accident (El-qarnia, 2009). Out of the two types discussed, organic PCMs were shown to be more advantageous for use in a LHESS because they are less corrosive (Sharma et al., 2009), have less sub-cooling, and have less deviation of thermal properties during melting and freezing cycles than inorganic PCMs (Sarı & Kaygusuz, 2002).

## *2.3 Experimental Studies*

Section 2.3 presents experimental setups commonly used by other researchers, along with the results and conclusions made concerning LHESS geometry, operating parameters, and heat transfer enhancement designs.

### 2.3.1 Experimental Setups

One of the most common experimental setups consists of a LHESS with a HTF pipe passing through the center, with hot and cold constant temperature water baths (with temperature controllers to limit fluctuations) from which the HTF is circulated to charge/discharge the system. Thermocouples are commonly placed throughout the PCM and on the storage container, while PCs and data acquisition (DAQ) systems of various kinds are used to record and save data (Agyenim et al., 2009; Ettouney et al., 2004; Jian-You, 2008; Sarı & Kaygusuz, 2002).

Centrifugal pumps are used to circulate the HTF through the PCM, and flow meters report flow rates to the DAQ (Akgun et al., 2007). Flow controls, such as throttling valves, are used to keep the HTF flow rate constant. Heat exchangers or radiators are used in some experimental setups to discharge the energy in the HTF that has not been collected by the PCM (Agyenim & Hewitt, 2010; Kaygusuz & Sari, 2005). Figure 2.1 shows a common setup for experimental studies of PCMs (Agyenim et al., 2009).

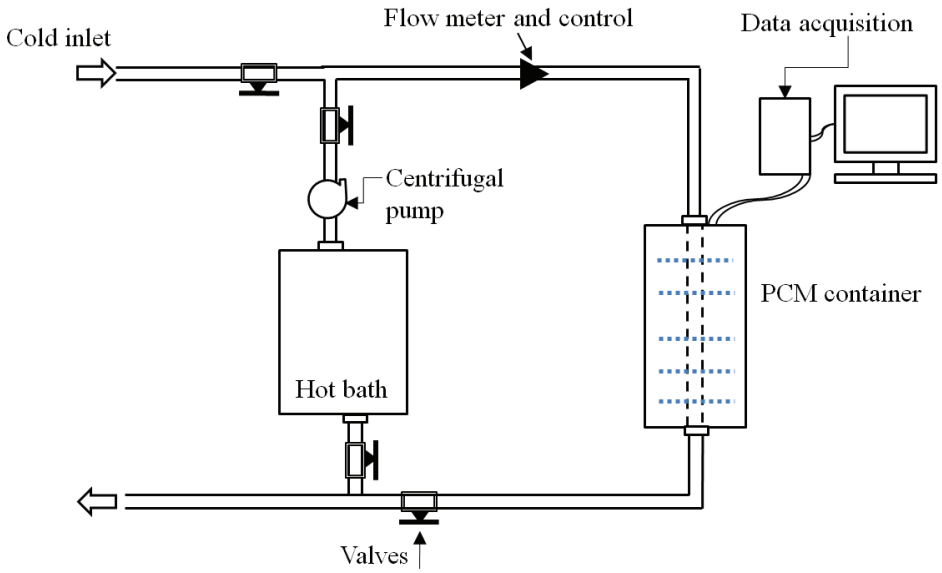


**Figure 2.1: Typical experimental setup**

All of the previously discussed experiments are designed to only study consecutive or separate charging/discharging since there is commonly only a single pass of the HTF pipe through the PCM, as shown in Fig. 2.1. However, Liu et al. performed simultaneous charging/discharging experiments on a heat pipe heat exchanger, not to be confused with a LHESS, with paraffin wax PCM storage. During simultaneous charging/discharging, heat transfer from the hot water directly to the cold water took up a major portion of the total heat recovered by the cold water, and only a small amount of heat went to, or was taken from, the paraffin wax. This is due to the small thermal resistance from the hot water to the cold water through the heat pipe (which is in direct contact with both the hot and cold water) compared with the thermal resistance from hot to cold

fluid through the paraffin wax. In this heat pipe setup, the hot and cold water are separated only by a thin wall. In a LHESS the hot and cold HTFs are separated by the high thermal resistance PCM, therefore the same results are not expected. In order to have more control over the amount of heat transferred from the hot/cold source to the PCM, an increase in the heat transfer surface area between the PCM and the heat pipe wall was recommended (Liu et al., 2006b).

### 2.3.2 Storage Geometry

Vertical cylindrical containers are the most common geometry for LHESS. A figure showing the various types of PCM container geometries is given by Agyenim et al. (2010) Vertical concentric pipe-in-pipe configurations with the HTF circulated inside the internal pipe through the PCM, which is in the annular space outside the metal HTF pipe, is a common configuration for consecutive charging/discharging experiments using the experimental setup discussed in Section 2.3.1 (Agyenim et al., 2010; Kamil & Sari, 2005). Horizontal cylindrical LHESS have been used as well. In one experiment a 1200 mm long, 375 mm diameter copper cylinder was used to hold RT-58 PCM, and a 65 mm diameter copper HTF pipe of the same length, with longitudinal fins for heat transfer, was placed centrally through the PCM (Agyenim & Hewitt, 2010). Although both vertical and horizontal cylindrical containers are common, there has been no direct comparison between the two. A less common cylindrical container design is an inclined outer shell with the PCM in the annular space, which is used for heat transfer enhancement by natural convection. Results show, using paraffin wax PCM, an approximate 30 % decrease in the total melting time using this configuration over a vertical outer shell (Akgun et al., 2007).

Multi-tube arrays involve a cylindrical PCM container with two or more HTF tubes through the container. Multi-tubes result in significantly more melting than a single pipe-in-pipe geometry, and experimental measurements have demonstrated earlier onset of natural convection resulting in multiple convective cells, which enhances melting (Agyenim et al., 2010). Multi-tube arrays were

shown to enhance heat transfer for a horizontally oriented cylindrical container with $CaCI_2.6H_2O$ as the PCM (Kaygusuz, 1995). Vertical multi-tube arrays were shown to be beneficial as well, due to the increased heat transfer surface area from the multiple HTF tubes, which results in higher heat fluxes. Higher heat fluxes in the vertically oriented container allow for increased natural convection heat transfer (Hamada, 2003). Although there are clear advantages of this geometry, due to its more complicated nature, heat transfer and phase change behavior is more difficult to study experimentally.

Rectangular flat plate containers were chosen for PCM storage by a research group because melting/solidification is symmetric about a plane at the center of the plate, and the surface area to volume ratio for heat transfer is largest compared with other geometries studied (Zalba et al., 2005). Experimental results for a stainless steel container, 100 mm wide, 100 mm thick, and 20 mm high, have shown that a rectangular container only requires half of the melting time of a cylindrical container with the same volume and heat transfer area (Zivkovic & Fujii, 2001).

Spherical containers are not as commonly used for LHESS, however research has been done on micro-encapsulated PCMs inside other LHESS geometries. Encapsulated PCMs, which have a barrier protecting the PCM from harmful interaction with the environment, provide sufficient surface area for heat transfer, and provide structural stability. Microencapsulation is not commonly used because it is more expensive and the matrix reduces the heat transfer through the PCM because it limits natural convection (Regin et al., 2008).

Researchers have also studied experimental systems in which PCMs are built directly into solar collectors (Alva et al., 2006; Mettawee & Assassa, 2006). In these cases the PCM is in direct contact with the energy source (*i.e.* the solar collector), which has been shown to increase the energy storage rate. It was found using this type of setup that having a smaller solar collector surface area for heat collection and larger PCM surface area for heat transfer results in lower

outlet HTF temperatures and more energy stored in the PCM, but an increased cost of the LHESS due to a larger amount of PCM required (Koca et al., 2008). The possible use of this design is limited to special applications, such as space and soil heating of greenhouses located in arid zone areas, during winter (Rabin et al., 1995).

### 2.3.3 System Operating Parameters

There are a number of operating parameters that can be adjusted to achieve optimum operation and storage capacity of a LHESS. These parameters include the HTF temperature at the inlet of the LHESS, and the flow rate and direction of the HTF (Castell et al., 2008).

Of the parameters studied experimentally, an increase in the HTF inlet temperature has been shown to lead to a decrease in the melting time (Akgun et al., 2007) and an increase in the amount of energy that can be stored (Agyenim et al., 2010; Jian-You, 2008). In one experiment in which dodecanoic acid filled the annular space between the PCM container and the HTF pipe, the average heat transfer rates were found to increase when the inlet HTF temperature was increased during melting, and the average heat transfer rates decreased when the inlet HTF temperature was decreased during solidification (Sarı & Kaygusuz, 2002). Also, at lower flow rates during charging the PCM temperatures took longer to increase, resulting in lower energy storage rates (Jian-You, 2008; Mettawee & Assassa, 2006).

It was shown for a vertical pipe-in-pipe LHESS configuration that natural convection effects played a major role during melting when the HTF entered the container from the bottom of the LHESS, but were not significant when the HTF entered from the top of the container (Ettouney et al., 2004). Also, in a 1200 mm long and 90 mm diameter vertically oriented pipe-in-pipe LHESS configuration, with $CaCl_2$ as the PCM, using air as the HTF was shown to increase reliability of results by allowing for longer cycle times (Bajnoczy et al., 2000).

### 2.3.4 Heat Transfer Enhancement

Due to the low thermal conductivity of PCMs, designs to enhance heat transfer were identified in order to increase energy storage rates and decrease charging/discharging times of a LHESS (Mettawee & Assassa, 2007). Many different methods of increasing heat transfer through PCMs were studied. These methods include extended fins, multi-tube arrays, bubble agitation, metal rings, metal matrixes and brushes, and encapsulation (Jegadheeswaran & Pohekar, 2009). Studies were performed to determine which of these heat transfer enhancement methods are the most advantageous, and the use of fins and high conductivity matrixes were shown to be the most attractive options (Kenisarin & Mahkamov, 2007). A comparison of three different enhancement techniques, internal longitudinal fins, lessing rings, and bubble agitation, showed that lessing rings and fins are acceptable in situations where solidification enhancement is required, and the bubble agitation is useful only when melting enhancement is required (Velraj et al., 1998).

Varieties of fin configurations were studied and found to be an effective and inexpensive way to enhance heat transfer. When heat is being transferred between the PCM and HTF, fins can either be on the PCM side or on the HTF side. Fins are usually put on the side that has the lowest thermal conductivity because this will result in a higher fin efficiency (F. P. Incropera, 2007), so normally fins extend into the PCM. Fins can be either vertical (longitudinal in the case of a cylindrical container) or horizontal (radial in the case of a cylindrical container). Radial fins were shown experimentally to aid conduction heat transfer and result in the largest increase in heat transfer rates during the solidification process, whereas longitudinal fins have the most increase in heat transfer during melting (Nagano, 2004). This is because, for the case of vertical cylindrical systems, radial fins inhibit natural convection during the melting process, whereas longitudinal fins do not (Nagano, 2004). In an analytical study, radial fins were found to be the most effective fin type (Lacroix, 1993), however most experimental results show that longitudinal fins are best for decreasing the time required for PCM melting and solidification (Agyenim et al., 2009;

Murray et al., 2011). The presence of fins also decreases the overall volume of PCM in the system, thus decreasing the total storage capacity. Therefore the advantages of fin additions may be outweighed by the disadvantages (Stritih, 2004). For example, a simple increase in the number of fins on the PCM side has been shown to result in insufficient enhancement of heat transfer to compensate for the reduced PCM volume for energy storage (Nagano, 2004). Using longer fins was also shown to decrease the solidification time of the PCM, and to promote a higher natural convection heat transfer coefficient over a smaller change in temperature (Castell et al., 2007). A combined numerical and experimental study suggested that a metallic tube fitted with four or five longitudinal fins with a radial length around twice the tube diameter is the best compromise between efficiency, increase in the heat flow rate, and loss of available storage capacity (Ismail & Abugdera, 2000). The effectiveness of fins at enhancing heat transfer also depends on the mechanism of heat transfer (melting or solidification), for example, fins were shown to be more effective during solidification than during melting in a rectangular container because natural convection, which is dominant during melting, is reduced with the addition of these fins (Stritih, 2004).

The effects of carbon fiber chips and carbon brushes as additives to a PCM used in a LHESS were studied, and results showed that the addition of carbon fiber chips (fiber diameter 10 μm, fiber length 5 mm) results in a higher effective thermal conductivity of the bulk PCM, for the case of a vertically arranged cylindrical container made of acrylic resin with n-octadecane PCM (Hamada, 2003). However, the thermal resistance near the heat transfer surface was higher than that of the carbon brushes (brush diameter 110 mm, axial length 60 mm), therefore the overall heat transfer rate for the fiber chips was lower than for the carbon brushes, even though the effective thermal conductivity of the bulk PCM with the fiber chips is higher (Hamada, 2003). Another study compared stainless steel pieces, copper pieces and a new PCM-graphite composite material, all inside a rectangular storage tank with dimensions of 107 mm height, 105 mm width, and 430 mm

length. Graphite composites were found to allow for a larger increase in heat transfer over stainless steel or copper tube. This is because the effect of inserting metal pieces into the PCM is only useful if the metallic material has very high conductivity to make up for the loss of storage capacity due to the decreased volume of PCM (Cabeza et al., 2002).

Using an experimental setup which combines storing latent and sensible heat using a combination of PCM and water inside a storage container is advantageous for SDHW applications (Canbazoglu et al., 2005). In a system with energy input from a flat plate solar collector, a combined storage system using water and paraffin wax (with the wax inside aluminum bottles in the vertical cylindrical storage container), kept the storage water temperature over 45 $^{o}$C under all operational and climatic conditions (Al-Hinti et al., 2010). However, a one hour time lag was noticed between the peak solar radiation and the peak water temperature in the tank. It was demonstrated that in cases of high domestic water consumption during evening hours, the existence of the PCM partially recovers the temperature of water, and extends the effective operational time of the system (Al-Hinti et al., 2010). As well, the rate of storage of energy, the mass of hot water produced, and the heat accumulated in the storage tank were several times greater when using PCM in the storage tank than that of conventional solar energy system using a heat storage tank with just water (Canbazoglu et al., 2005). In a system with granular PCM–graphite compound (90 vol.% of sodium acetate and 10 vol.% graphite) in aluminum bottles at the top of a water storage tank connected to flat plate solar collectors, the energy density of the storage container increased from 57 % with four PCM bottles to 78 % with six PCM bottles: more PCM inside the storage tank results in a higher energy density (Cabeza et al., 2006). Along with the advantages already discussed, thermal stratification can be employed to improve the efficiency of storage tanks. This is because the PCM at an intermediate temperature in the middle of the storage tank (not high enough temperature to heat the top layer) transfers energy to heat the lower, colder layers (Mehling et al., 2003). Energy density improvements of 20 to 45 % were

shown using a cylindrical tank with a diameter of 20 cm and a height of 120 cm. This type of heat storage is a good use of low-temperature heat and/or waste heat (Mehling et al., 2003). However, if the thermal conductivity of the PCM container material is low, the actual melting time of the PCM is longer than the theoretical melting time, and therefore, the cylindrical container materials and dimensions should be selected carefully (Kaygusuz, 2003).

One way optimize the latent heat that can be stored in a system is to use multiple PCMs with various melting temperatures so that latent energy is collected over a broader range of temperatures. If the phase change temperature of the PCM corresponds to a variety of solar conditions, a phase transition will occur on all days when the solar gain exceeds a certain value (Bajnoczy et al., 2000). An increased cumulative storage capacity was shown in a cylindrical LHESS, 1200 mm long and 90 mm in diameter, with a two-grade heat storage system (a combination of 60 to 30 $^{o}$C using $CaCl_2.4H_2O$ and 30 to 20 $^{o}$C using $CaCl_2 \cdot 6H_2O$) compared to a single-grade system (using only $CaCl_2.6H_2O$) (Bajnoczy et al., 2000). Improvements in charging and discharging rates were observed in a LHESS using three PCMs with varying melting temperatures (Watanabe et al., 1993).

### *2.4 Numerical and Analytical Methods*

Predicting the behavior of phase-change systems using numerical analysis is difficult due to its inherent non-linear nature at moving interfaces and the transient characteristics of the process. Several methods are used to solve the phase change problem, the most common being the enthalpy method (Trp et al., 2006). By introducing an enthalpy method, the phase-change problem becomes much simpler since the governing equation is the same for the two phases, interface conditions are automatically achieved and create a mushy zone between the two phases, and a fixed grid can be used. In this method the enthalpy is defined as a function of temperature

(Dutil et al., 2011; Ogoh & Groulx, 2012) and in the solid-liquid phase region physical properties vary linearly with temperature (Chen et al., 2010).

The majority of numerical and analytical studies are based on the assumption that conduction is the major mechanism of heat transfer, and convection can be neglected in the melted PCM (Godarzi et al., 2010; Trp et al., 2006). Some researchers have shown using experimental and numerical comparisons that the effects of natural convection within the liquid PCM can be ignored for the case of thin rectangular PCM containers (Zivkovic & Fujii, 2001) and for low heat fluxes (Shatikian et al., 2008). It has been shown that an analytical model gives more precise results for the solid–liquid interface location in cases when the ratio of side lengths is much smaller than unity or much bigger than unity (Lamberg, 2004). However, other researchers have shown that for the case of spherical capsules, experimental and numerical results match more closely when natural convection is numerically accounted for in the melted PCM, and a fixed temperature range (such as 1 K) for phase change is used (Regin et al., 2006). Therefore the PCM container geometry is an important consideration when deciding whether or not to model natural convection in the melted PCM, and has an influence on the accuracy of the model. Natural convection in the melted PCM can be modeled using an effective thermal conductivity which takes into account the additional heat transfer by convection (El-qarnia, 2009), or by using physical properties (viscosity and density) that vary as a function of the PCM temperature (Murray & Groulx, 2011). Using the later method, the PCM is modeled as a fluid, with the viscosity infinitely large when the PCM is below the melting temperature, which causes it to act as a solid (Murray & Groulx, 2011).

Along with the experimental setups discussed in Section 2.3.1, numerical models have been used to study LHESS designs and operating parameters. It was shown numerically that significantly more latent heat is stored during the melting process in the multi-tube arrays than the single pipe-

in-pipe configurations. This increases the energy storage capacity of the PCM (Farid, 2004; Hendra et al., 2005). Microencapsulation was studied numerically, but most work found that the matrix reduces the heat transfer through the PCM because it limits natural convection. This, along with the increased expense of microencapsulation, has made it less common (Ismail & HenrõÂquez, 2000). Similarly to the experimental case, PCMs of a variety of melting temperatures in the same storage container were studied. A five-grade PCM model was compared to a single-grade PCM model using a single pass shell and tube heat exchanger of the same length in both cases, and more isothermal operation was found with the five PCM model. Also, the five PCM model was shown to facilitate melting of the PCM at the HTF outlet, where normally less melting is observed due to the temperature drop in the HTF relative to the PCM melting temperature (Seeniraj & Narasimhan, 2008).

It was shown experimentally that at lower flow rates the temperatures of the PCM in the storage system take longer to increase and heat transfer rates are lower (Jian-You, 2008; Mettawee & Assassa, 2006). This was verified with a numerical model which showed that increasing the flow rate increased the heat transfer rate and volume fraction of melted PCM over time (Lacroix, 1993). The direction of HTF flow also has an impact on the heat transfer rates. For consecutive charging/discharging experiments it was found that introducing the hot and cold fluid from the same end of a horizontal storage container resulted in a 5 % increase in the heat transfer rate over introducing the hot and cold fluid from opposite ends of the container (Gong & Mujumdar, 1997).

Varieties of fin configurations were studied numerically as well. Numerical simulations have indicated that an optimal number of fins should be used to improve the overall system performance and proper geometrical fin design has a strong influence on the solidification rate of the PCM (Ismail et al., 2000). Numerical studies differ from experimental results when it comes to fin studies. For example, the melted volume fraction was found numerically to significantly

increase by increasing the size (thickness and height) and number of longitudinal fins on the HTF side (Zhang & Faghri, 1995). This goes against the results found experimentally, where the presence of fins decreases the overall volume of PCM in the system thus decreasing the total storage capacity (Stritih, 2003). In the model used by Zhang & Faghri, natural convection was neglected and a single melting point was used for the PCM, which could explain the differing results (Zhang & Faghri, 1995). As well, differing from experimental studies, Sasaguchi found using a numerical model that the performance of the LHESS unit is almost the same for any fin configuration with the same surface area (Sasaguchi et al., 1990). In this case natural convection was included in the numerical model, differing it from most LHESS models.

### *2.5 Significant Results from Literature*

Significant findings from the literature review are as follows:

- Organic PCMs with melting temperatures in the range suitable for the application (40 to 50 $^{o}$C for a SDHW system) are best for use in LHESS.
- Only one research group has studied the simultaneous charging and discharging mode of a heat exchanger with PCM storage. In this work a heat pipe heat exchanger was used, which differs from LHESS because the hot and cold HTFs are separated only by a thin sheet of metal instead of by a PCM. In all other experiments discussed in Chapter 2, the experimental setups only allow for consecutive or separate charging/discharging of a LHESS.
- Increasing the hot HTF inlet temperature results in an increase in the rate of energy storage.
- Longitudinal fins are best for enhancing heat transfer in vertical LHESS setups.

- Increasing the heat transfer surface area of fins is only advantageous if it does not interfere with natural convection in the melted PCM and does not take up too much PCM occupied volume (thus decreasing the storage capacity).
- The selections of hot and cold HTF inlet orientations and temperatures play a role in LHESS charging and discharging times. The hot and cold fluid entering from the same end of the container results in a 5 % increase in the heat transfer rate.

The above findings from the literature will aid in the design choices made for the LHESS used in this thesis.

# Chapter 3 Experimental Setup and Procedure

A LHESS was built in the Lab of Applied Multiphase Thermal Engineering at Dalhousie University. Because this is the first set of experiments done on such a system, the LHESS design was simple in nature to allow for characterization of the heat transfer processes inside the system. The LHESS experimental setup used in this thesis consists of a cylindrical PCM container with hot and cold HTF pipes, both pipes had external longitudinal fins to improve heat transfer through the PCM. Similar to experimental setups discussed in Section 2.3.1, in this experiment water from a constant temperature hot water bath was used to charge the system, and domestic (municipal supply) cold water was used to recover the stored energy, as shown in Fig. 3.1.

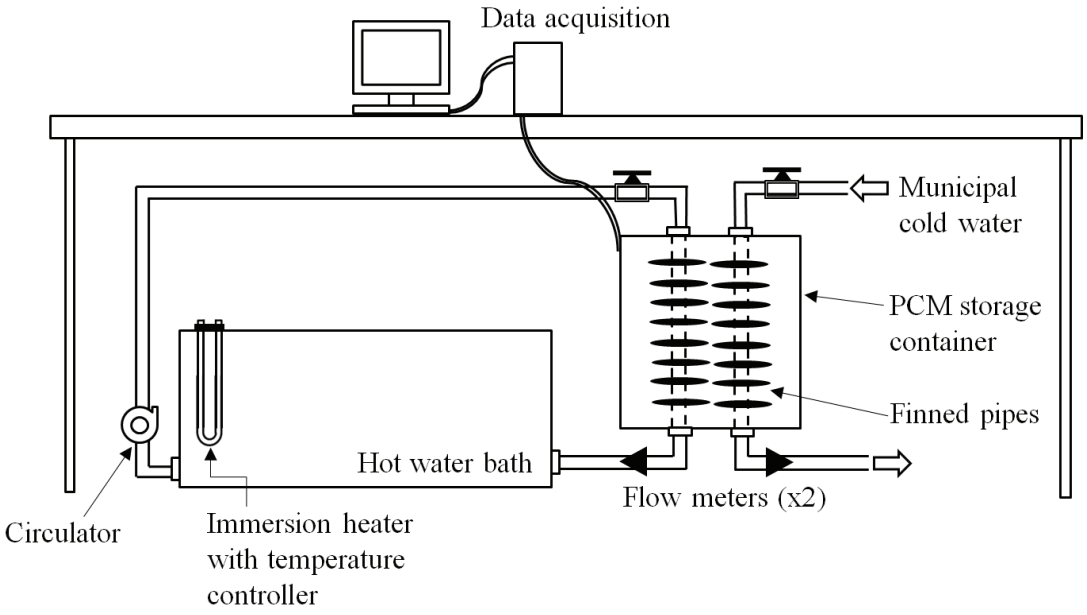


**Figure 3.1: Experimental setup including PCM container, hot water bath, pump, and DAQ**

## *3.1 Storage Container*

A 60.96 cm (2 ft) long, 20.32 cm (8 in) outer diameter container made of 0.635 cm (¼ in) thick Plexiglas was used to store the PCM. Initially the system was set up with the hot and cold HTFs entering the container from the same end, as suggested by Gong and Mujumdar to be the best inlet orientation for maximum energy storage (Gong & Mujumdar, 1996). However, the impact of

having the inlet of the hot HTF at the bottom of the container was studied as well. The total volume of the container is 19.53 L. Figure 3.2 shows a 3D CAD drawing of the Plexiglas container.

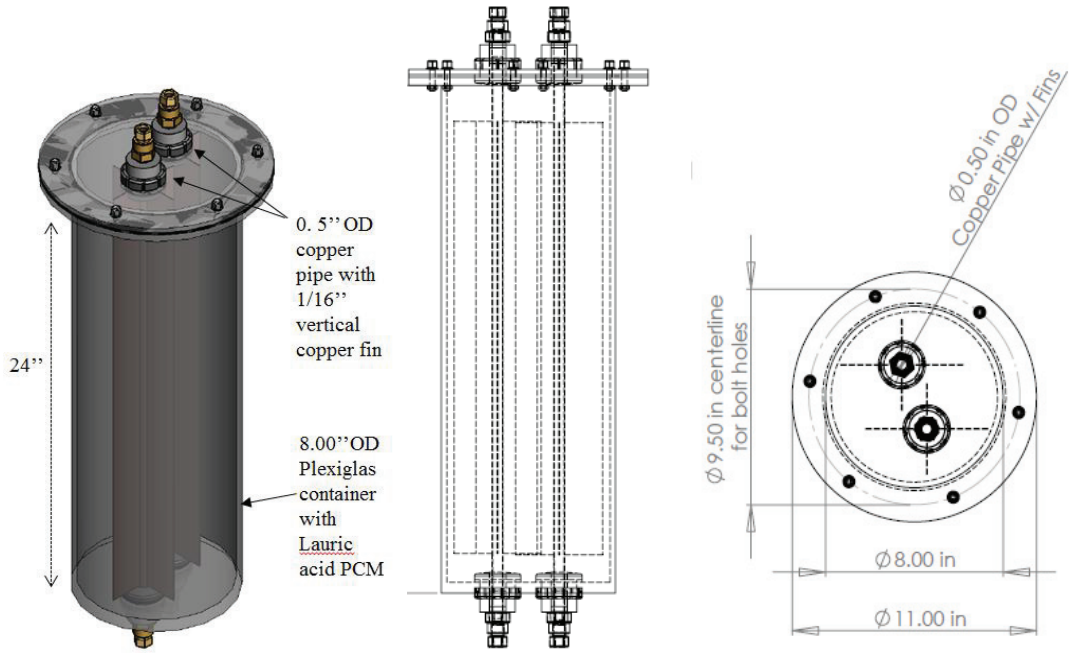


**Figure 3.2: 3D rendering and 2D cross-sectional views of the LHESS**

To build the LHESS, a 1.27 cm (½ in) thick, 27.94 cm (11 in) outer diameter Plexiglas flange was epoxy glued to the top of an 8-inch diameter Plexiglas tube. A 1.27 cm (½ in) thick and 20.32 cm (8 in) diameter circular piece of Plexiglas was attached to the bottom of the tube, and an 27.94 cm (11 in) diameter Plexiglas lid was bolted with 6 bolts to the flange, as seen in Fig. 3.2.

Two copper pipes were fixed with four 0.061 cm (0.024 in) thick longitudinal fins each of which extend the full length of the Plexiglas container. The fins vary in width from 2.54 cm to 4.45 cm (1 in to 1.75 in) wide, depending on their location, so that each fin extends to within 1.27 cm (½ in) from the inside wall of the Plexiglas. Polyvinyl chloride (PVC) tank adapters and bulkhead fittings were used to seal the pipe entry and exits. Each copper pipe had a single pass through the PCM, which will not lead to fast charging and discharging, but will make the heat transfer and

phase change processes inside the PCM easier to identify. Figure 3.3-a) and 3.3-b) show photographs of the system, including the copper fins, taken while the melted PCM was being added to the container, before insulation was put on. This photograph also shows the probe thermocouples and the bulkhead fittings (at the bottom of Fig. 3.3a).

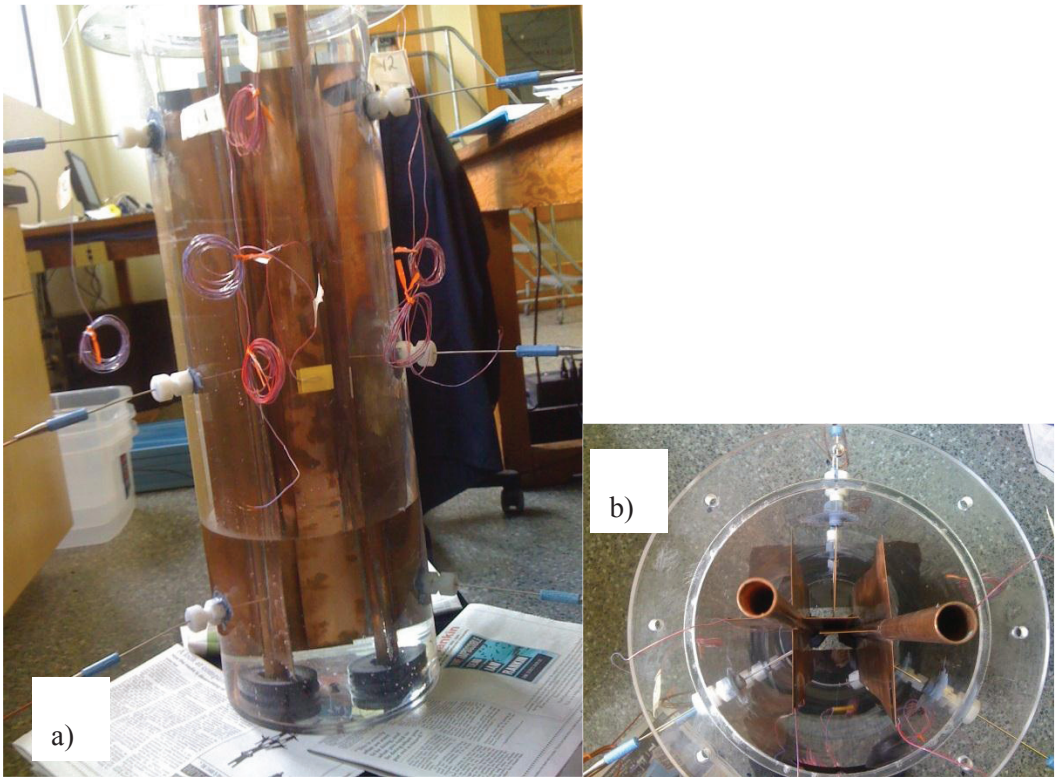


**Figure 3.3: Photograph of the PCM container, thermocouple probes, and copper finned HTF pipes a) side view b) top view**

After an initial experiment without insulation to allow visual observation of the system, the container was insulated using fiberglass insulation (thermal conductivity of $k$=0.04 W/mk). After running an experiment with only 0.635 cm (¼ in) insulation thickness, more was added to the system to reduce heat losses through the container. The experiments presented in Chapters 5 and 6 were performed using 1.9 cm (¾ in) thick fiberglass insulation.

### *3.2 Temperature Measurements*

Nineteen type-T thermocouples were connected to a National Instruments 16-channel thermocouple module (NI9213) CompactDAQ and a National Instruments 4-channel thermocouple module (NI9211). Both of these NI DAQs have 24 bit analog-to-digital converter and can measure temperature up to 0.02 $^{o}$C measurement sensitivity, which is acceptable for the experiments presented in this thesis.

Nine thermocouple probes (T1 to T9), 0.159 cm (0.0625 in) in diameter, were located inside the PCM at three heights, in the locations given in Fig. 3.4. The radial location of these thermocouple probes in the horizontal plane can be adjusted by loosening compression fittings, seen in Fig. 3.3-a), and sliding the probes in/out. The number of thermocouple probes was limited due to possible cracking of the Plexiglas.

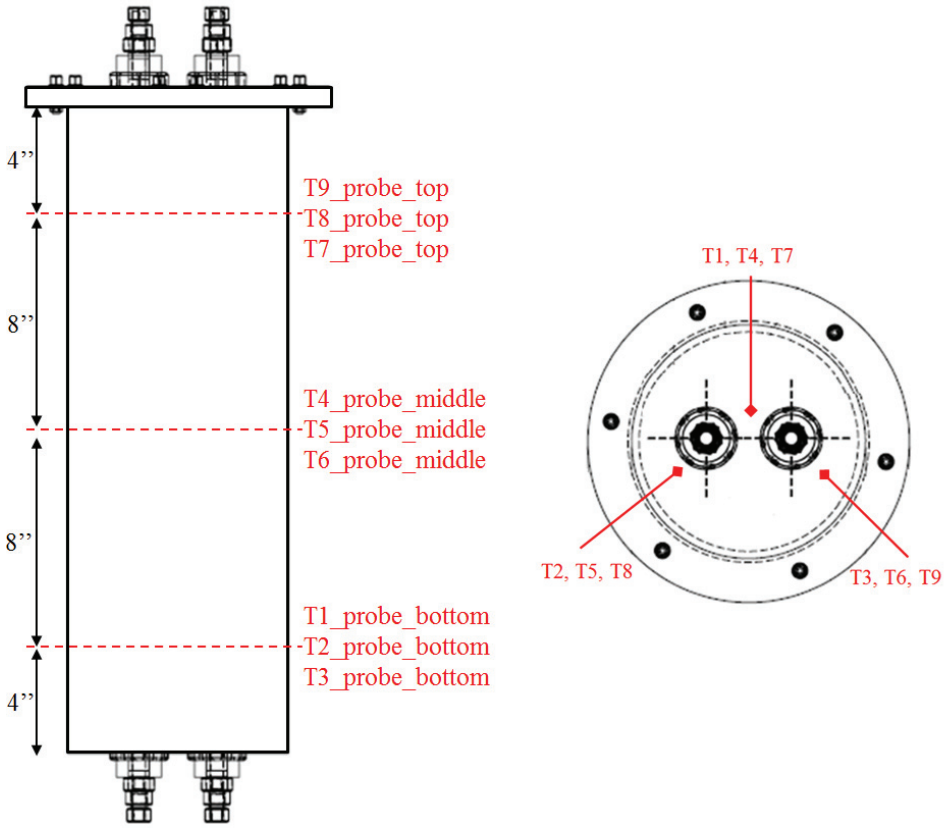


**Figure 3.4: Thermocouple probe positions**

Thermocouple probes were also placed at the inlets and outlets (T16 to T19), 0.318 cm (0.125 in) in diameter, to measure the temperature of the HTF as it enters/exits the LHESS. Four self-adhesive thermocouples (T10 to T13) were located at the same height as the top thermocouple probes (10.2 cm (4 in) below the top of the container) on the copper fins as seen in Figure 3.5. These locations were chosen so that along with the three probes at this height, a full temperature profile could be mapped in the horizontal plane at this height.

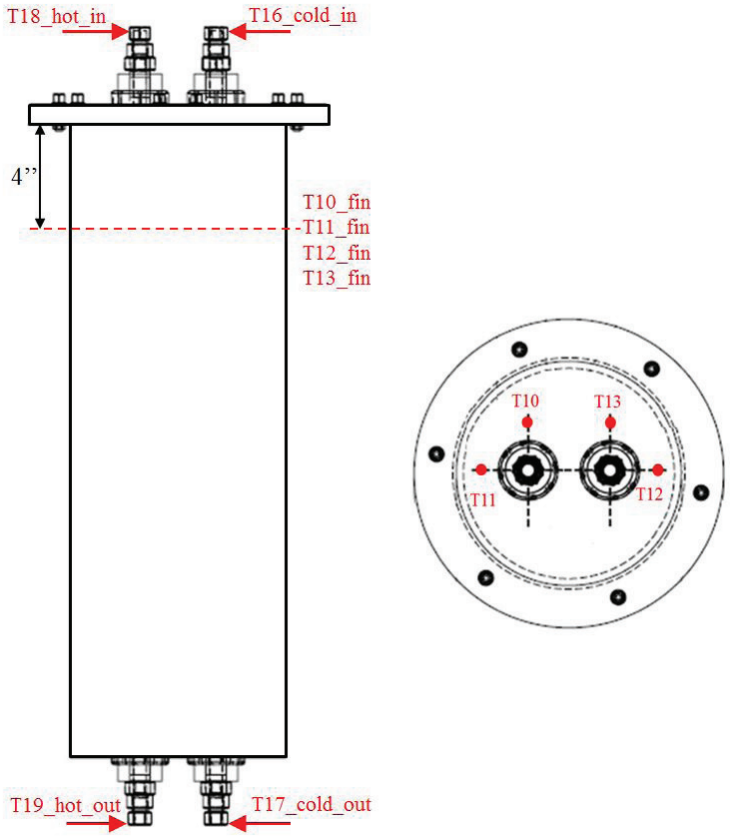


**Figure 3.5: Adhesive thermocouple fin position**

### 3.2.1 Thermocouple Calibration

Thermocouples T16 to T19 (inlet and outlet HTF thermocouples) were calibrated using the Alpha FLUKE 7102 micro-bath and the calibration program in LABView in order to reduce the uncertainty in the temperature measurements taken with these thermocouples. This calibration reduced the uncertainty in temperature measurements made by T16 to T19 to 0.4 $^{o}$C. All other

thermocouples were used with the original uncertainty of 0.5 ˚C, as given by the manufacturer. To account for hysteresis, the thermocouples were calibrated both by heating and cooling the micro-bath. The thermocouples were checked after calibration to insure consistency, as seen in Appendix A.

### *3.3 Pump*

A magnetic drive centrifugal pump was used to circulate the hot HTF, and the pressure from the municipal water supply was sufficient to circulate the cold water. The calculations behind choosing the pump are highlighted in Appendix B, and the Cole Parmer model EW-72012-10 circulator was chosen. Ball valves are used on both the hot HTF loop and cold HTF loop to throttle and control the HTF flow rates.

### *3.4 Flow Meters*

Two OMEGA pulse counting flow meters (model FTB 4605) were used to track the flow rates of the hot and cold HTFs during the experiments. A circuit with a step up resistor was used to convert the pulse signal from the flow meter into an analog signal that could be read by National Instruments NI9435 and NI9422 modules. This circuit diagram can be seen in Appendix C. One module is used for each pulse counting flow meter. The frequency signal (pulse/sec) can then be converted to a flow rate knowing that these flow meters operate at 40 pulses/L. Both flow meters were calibrated for accuracy by measuring the time required to fill a 2 L container using a range of flow rates.

### *3.5 Phase Change Material*

Dodecanoic acid ($CH_3(CH_2)_{10}COOH$, 98 % pure, Alfa Aesar) was chosen as the PCM for this experiment because it is safe, relatively inexpensive, has a melting temperature of 42.5 ± 0.5 ˚C (within the desired range for use with SDHW), and was found to have stable thermal properties during testing. The ideal melting temperature range was chosen by evaluating temperature data

from an existing SDHW system (Murray et al., 2011). Table 3.1 outlines the thermophysical properties of dodecanoic acid.

**Table 3.1: Thermophysical properties of dodecanoic acid**

| | |
|---|---|
| Molecular Weight* | 200.31 kg/kmol |
| Density of Powder at 20°C / Liquid at 45°C* | 869 / 873 kg/m$^3$ |
| Melting Temperature* | 42.5 ± 0.5 ˚C |
| Latent Heat of Fusion* | 182 kJ/kg ± 5 % |
| Heat Capacities Solid/Liquid † | 2.4/2.0 kJ/kg·K ± 3 % |
| Thermal Conductivities Solid/Liquid † | 0.150*/0.148 W/m·K |
| Viscosity † | 0.008 Pa·s |

† Calculated using experimental methods (Desgrosseilliers et al., 2012)
*Chemical Properties Handbook (1999)

### *3.6 Construction of the Experimental Setup*

The following is an overview of the procedure used to prepare the LHESS for experimental testing:

1) Nine thermocouple probes were inserted in the locations given in Fig. 3.4 through compression fittings on the outside of the PCM container, and four thermocouple probes were inserted in the locations given in Fig. 3.5 through compression fittings at the inlets/outlets of the hot and cold HTF pipes;
2) The four adhesive thermocouples were attached to the copper fins in the locations shown in Fig. 3.5;
3) The container was filled with melted dodecanoic acid from the top, and the Plexiglas lid was bolted back in place;
4) The immersion heater was connected with a bulkhead fitting to the hot water bath;
5) The centrifugal pump was connected to the outlet of the hot water bath, ensuring that the water-line in the bath was above the pump inlet for priming;
6) The hot HTF pipe was connected from the top of the LHESS to the pump, and from the bottom of the LHESS to the flow meter. The flow meter was connected to the inlet of the hot water bath to complete the hot HTF loop;

7) The cold HTF pipe was connected from the top of the LHESS to the municipal water source and from the bottom of the LHESS to the flow meter. The flow meter was connected to a pipe that exits to a drain;
8) The flow meter and thermocouple wires were connected to the NI modules, and the DAQ was connected to the computer;
9) The hot water bath was filled with lab grade water (to decrease rusting of the copper pipes), and the pump was run at high speed to fill the hot HTF pipe loop.

The photograph in Fig. 3.6 shows the entire experimental setup with the components labeled.


**Figure 3.6: Experimental setup including PCM container, hot water bath, flow meter, and DAQ (Another LHESS experimental setup is seen in the background)**

The pump is located behind the constant temperature hot water bath and is not shown in Fig. 3.6. As well, the flow meter on the cold loop is located at the outlet of the cold HTF pipe and cannot be seen in Fig. 3.6. The expected energy storage for this system is presented in Section 4.1.

## *3.7 Experimental Procedure*

The operating parameters vary by experiment, and are given Chapter 5 and 6 with the experimental results. The following procedures were followed for the charging, discharging, and simultaneous charging/discharging experiments:

### 3.7.1 Charging

1) A LabVIEW DAQ-Assist program was created on the desktop computer to record temperatures and flow rates during experiments;
2) The hot water in the bath was heated to the required inlet temperature;
3) The pump was turned on to full power and a ball valve at the outlet of the pump was throttled to maintain the required hot HTF flow rate;
4) The hot HTF was circulated through the PCM container until all thermocouples read above the melting temperature of the PCM, and all the PCM was melted upon observation.

### 3.7.2 Discharging

1) Cold water from the municipal supply was turned on fully and a ball valve was throttled to maintain the required flow rate of cold HTF;
2) The cold HTF was circulated through the PCM container until all the thermocouples read room temperature or lower, and all PCM was solid upon observation.

### 3.7.3 Simultaneous Charging and Discharging

1) The LHESS was either charged or discharged to achieve the initial conditions used in the experiment (*i.e.* either the PCM was completely melted or completely solid);

2) The procedures given for the charging and discharging experiments were followed simultaneously for a fixed time interval, followed by charging only for a fixed time interval;
3) This cycle was repeated five times or until patterns in the PCM behavior emerged, upon observation.

### 3.7.4 Additional Procedures

In the case that the thermocouples at the inlet/outlet of the hot HTF pipe are removed, or any part of the hot water loop is opened to the atmosphere, the pump must be run at full speed for a brief period of time to force any air out of the loop. In the case that this procedure is not followed, the thermocouples at the inlet and outlet of the hot HTF pipe, and the flow meter on the hot water loop, may read incorrect values due to an air lock in the system.

## *3.8 Numerical Model*

COMSOL Multiphysics (version 4.2a) was used to build a 2D symmetric numerical model of the charging experiment using the *Heat Transfer in Solids* physics module. The thermophysical properties of water and copper used in the model were specified in the COMSOL material library. The properties used for the PCM are given in Table 3.1. The following assumptions were made to simplify the model:

1) Natural convection in the melted PCM was neglected;
2) A 2D horizontal slice of the system is sufficient to model the system;
3) Heat source is a constant temperature or a constant heat flux at the inner pipe wall.

The following boundary and initial conditions were used:

1) Initial temperatures of the model match the initial temperatures recorded experimentally by the thermocouples;
2) All outside walls were insulated;

3) No-slip condition on the inner pipe wall;

4) No viscous stress and convective flux at the pipe outlet.

Natural convection in a PCM is present after the PCM melts; however, the numerical model used in this thesis has conduction heat transfer only, and therefore is a non-physical case and can only be validated before melting occurs. This model was used as a reference to clearly identify the heat transfer mechanisms taking place before the PCM melted in the experiment. A 2D horizontal slice of the LHESS was used because without the gravity effects of natural convection heat transfer, the temperature profiles would be the same at every height in the LHESS.

Predicting the behavior of systems undergoing phase changes using numerical analysis is difficult due to the inherent non-linear nature at moving interfaces and the transient characteristics of the process. Several methods are used to solve the phase change problem, the most common being the enthalpy method as presented by Ogoh and Groulx, which was used for the numerical model in this thesis (Ogoh & Groulx, 2010). The heat source was modeled as both a constant surface temperature and a constant heat flux, and both methods are compared to experimental results in Chapter 5. The temperature difference between the inlet and outlet of the hot HTF was shown experimentally to be small, which justifies using a constant temperature on the inside surface of the copper pipe wall as the heat source. However, the convection coefficient of the water inside the copper pipe is known as well (shown in Section 4.3), and using a constant heat flux as the heat source may be appropriate. To model the constant heat flux, the forced convection coefficient, $h$, corresponding to the hot HTF flow rate is used in Eq. (3.1). The forced convection coefficient is calculated in Chapter 4 for the corresponding hot HTF flow rate.

$$Q''_{convection} = h\Delta T. \tag{3.1}$$

where $\Delta T$ is the temperature difference between the hot HTF fluid and the surrounding PCM.

### 3.8.1 Mesh Convergence Study

2D quadrilateral elements were used to discretize the model because they have a higher level of accuracy than triangular elements. A mesh convergence study was performed to determine the optimum element size to produce consistent results and use minimal computational time. The melted fraction of the PCM in the model was calculated half way through (15 hours) and at the end (30 hours) of the charging period as shown in Fig. 3.7 for a variety of element sizes.

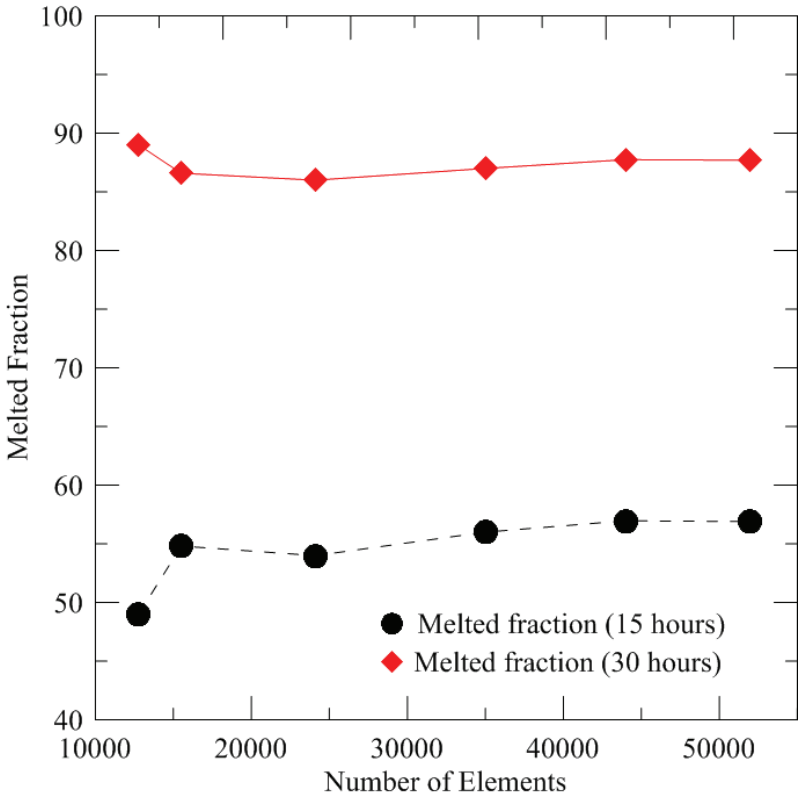


**Figure 3.7: Mesh convergence study- Element size *vs.* melted fraction of PCM**

The total size of the geometry in COMSOL is 0.0324 $m^2$. From Fig. 3.7, 43987 and 75564 elements produce the same results, therefore, stable results are obtained for 43987 elements or more. Figure 3.8 shows the computational time as a function of the number of elements used. The simulations were all run on a Dell T1500 Intel Core i7 CPU with 8 GB of memory and 2.93 GHz processor speed.

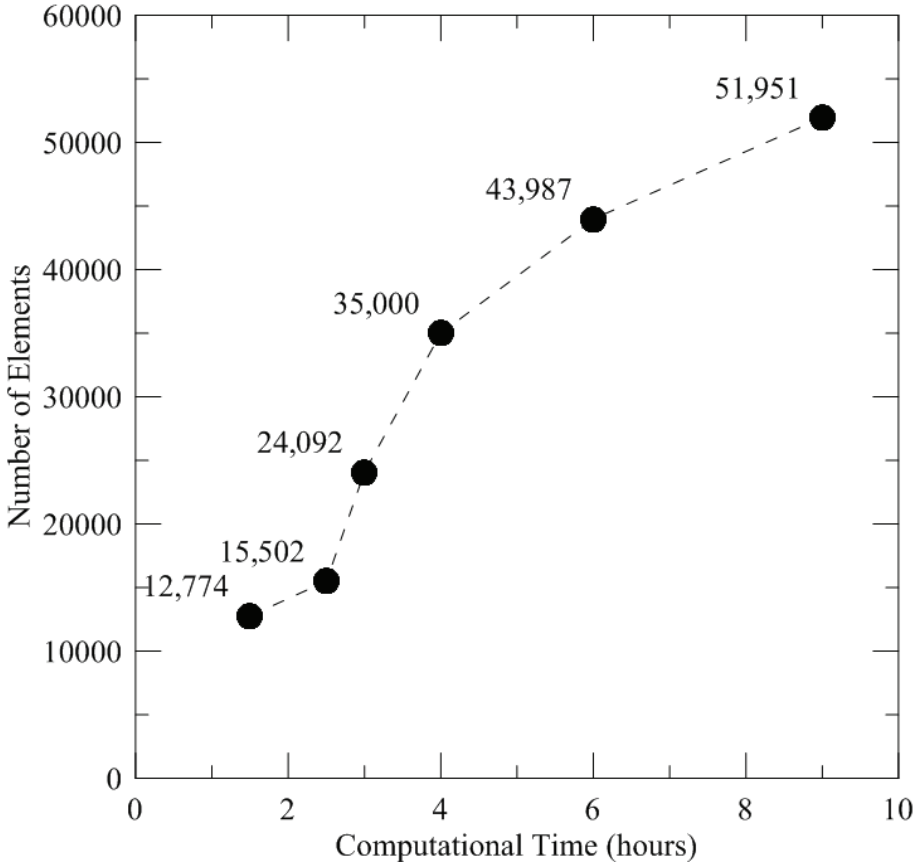


**Figure 3.8: Mesh convergence study: Computational time *vs.* number of elements**

43987 elements provided accurate results but significantly less computing time, therefore the final mesh chosen has 43987 elements with an average element size of 0.737 $mm^2$. Figure 3.9 shows the geometry and mesh of the numerical model.

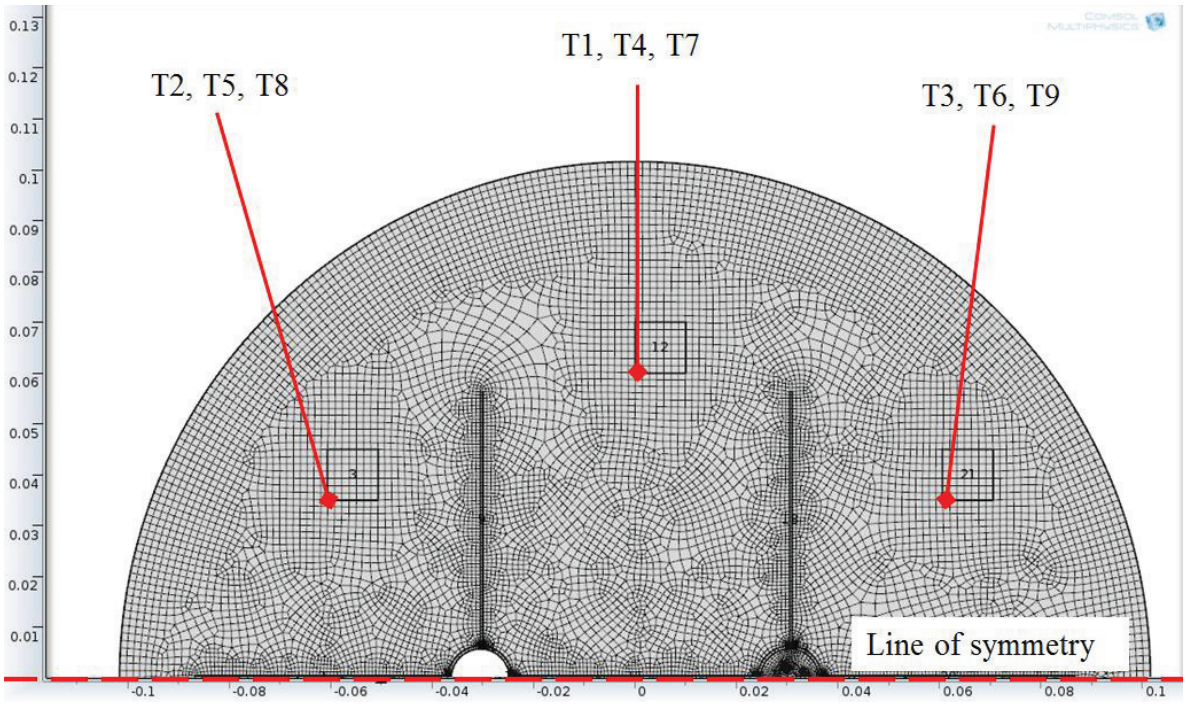


**Figure 3.9: 2D quad mesh used for LHESS model in COMSOL Multiphysics**

To reduce computational time, the mesh has smaller quad elements close to points of interest, and larger elements where the heat transfer patterns are more linear. In the experimental setup, nine probe thermocouples were placed throughout the system. The bottom left corners of the squares in Fig. 3.9 facilitate point measurements to be taken at the probe locations. Crossing line segments could have been used as temperature points as well, as long as a distinct point is created in the model geometry that does not interfere with the materials in the model.

# Chapter 4 Theory

## *4.1 Theoretical Energy Storage*

The theoretical energy storage capacity of the LHESS, based on the mass of PCM in the system, can be estimated using Eq. (1.3) and the parameters given in Table 4.1.

**Table 4.1: Energy equation parameters**

| | |
|---|---|
| $m_{\mathrm{PCM}}$ | 17.18 ± 0.01 kg |
| $T_{\mathrm{i}}$ | 10 ± 0.5˚C |
| $T_{\mathrm{f}}$ | 55 ± 0.5˚C |
| $m_{\mathrm{Water}}$ | 19.49 ± 0.01 kg |
| $Cp_{\mathrm{Water}}$ | 4.18 kJ/(kgK) |

The estimated energy storage of 17.18 kg of Dodecanoic acid is 5000 kJ ± 3 %, assuming all of the PCM reaches 55 ± 0.5 ˚C. Table 4.2 shows the contributions of latent and sensible energy to the theoretical energy storage capacity of the PCM.

**Table 4.2: Theoretical energy storage break-down**

| Energy Type | Amount | Percent of Total |
|---|---|---|
| Sensible energy (solid PCM) | 1340 kJ ± 0.8 % | 26 % |
| Sensible energy (liquid PCM) | 530 kJ ± 0.3 % | 10 % |
| Latent energy | 3130 kJ ± 1.9 % | 64 % |
| Total energy | 5000 kJ ± 3 % | |

The estimated energy storage for water with the same volume (and a corresponding mass of 19.49 kg) is 2444 kJ ± 3 %, which is 48 % of the energy storage capacity of the PCM. The energy storage capacity is a function of temperature, so the water and PCM capacity can be compared over a range of final temperatures using the same initial temperature of 10 ± 0.5 ˚C, as seen in Fig. 4.1. Based on the theoretical energy storage capacity, it is evident that water is a better storage medium when the system is below the melting temperature of the PCM (42.5 ± 0.5 ˚C).

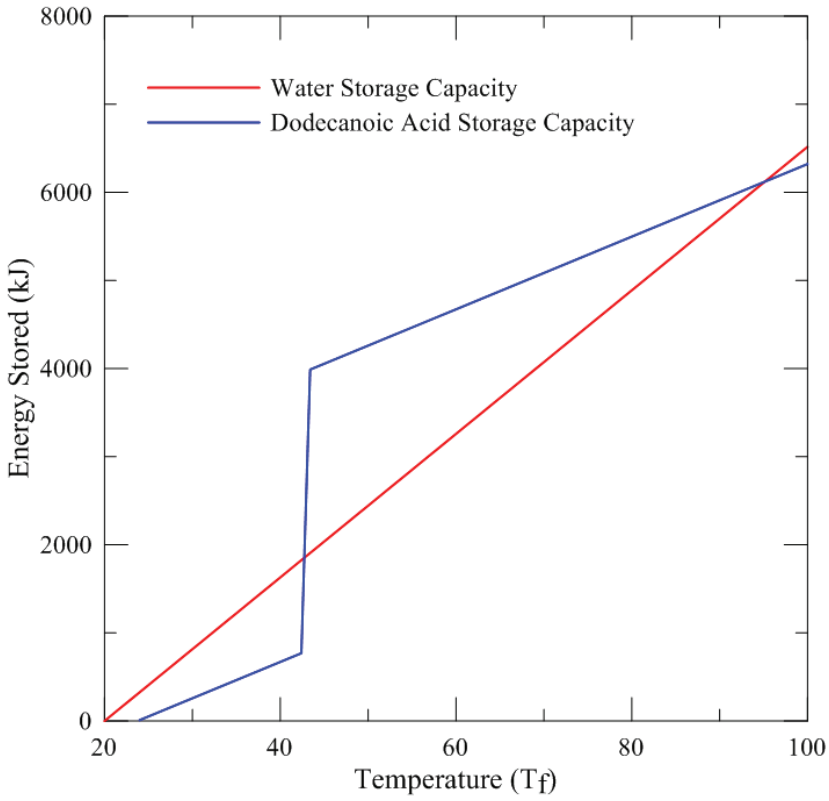


**Figure 4.1: Energy storage capacity of water compared to PCM**

The dodecanoic acid melting curve seen above will not be observed during the experiment because the PCM will melt at different times depending on its location in the container, while the theoretical curve assumes all the PCM goes through the phase transition at the same time. The water and the PCM have the same initial and final temperatures; therefore, the total change in energy from the initial state to the final state is comparable. However, between these two temperatures the energy as a function of temperature is not comparable because the water and PCM will not always be at the same state.

### *4.2 Experimental Energy Storage*

The total energy stored in the PCM is the energy input ($Q_{input}$) minus the heat lost through the PCM container wall ($Q_{loss}$). The power input ($\dot{Q}_{input}$) is the product of the HTF inlet/outlet temperature difference ($\Delta T$), the mass flow rate of the HTF ($\dot{m}$), and the specific heat capacity of

the HTF. The specific heat capacity of the HTF, in this case water, is $Cp_{water} = 4.18$ kJ/kgK. Inlet and outlet HTF temperatures and flow rates were recorded by the DAQ every 10 s, with the power calculated using Eq. (4.1).

$$\dot{Q}_{input} = \dot{m} Cp_{\text{water}} \Delta T. \tag{4.1}$$

The energy input ($Q_{input}$) was calculated by multiplying the power input by the $t$ = 10 s time interval. The total energy input during the experiment was calculated by summing the energy contributions over all the time intervals during the charging period, as given by Eq. (4.2).

$$Q_{input} = \sum t \dot{m} Cp_{\text{water}} \Delta T. \tag{4.2}$$

The same method was used for calculating the energy recovered ($Q_{recovered}$) during the discharging period.

### *4.3 Convection Coefficients*

The rate of forced convection heat transfer from the HTF to the copper pipe depends on the convection coefficient, $h$, as given by Eq. (4.3).

$$h = \frac{k}{D} \text{Nu}_{\text{D}}. \tag{4.3}$$

Where $k$ is the thermal conductivity of the water and $D$ is the diameter of the pipe. The Reynolds number ($\text{Re}_{\text{D}}$) is an indication of the flow regime inside the HTF pipe, and is calculated knowing the HTF velocity ($V$), fluid viscosity ($\mu$), density ($\rho$), and pipe diameter, as given in Eq. (4.4).

$$\text{Re}_{\text{D}} = \frac{\rho D V}{\mu}. \tag{4.4}$$

For internal flow in a circular pipe, a Reynolds number of less than 2 300 indicates laminar flow, and a Reynolds number of 2 300 or higher indicates turbulent flow. For laminar internal pipe

flow, the Nusselt number is $Nu_D$=3.66 assuming constant surface temperature, and $Nu_D$=4.36 assuming constant heat flux (F. Incropera et al., 2007). The Nusselt number, $Nu_D$, can be calculated using the Dittus-Boelter correlation for turbulent internal flow in a circular tube (F. Incropera et al., 2007), which is given in Eq. (4.5).

$$Nu_D = 0.023\, Re_D^{\frac{4}{5}}\, Pr^n. \tag{4.5}$$

The Prandtl number, Pr, comes from HTF properties (in this case water properties) taken at the average temperature. For charging, $n = 0.4$ and for discharging $n = 0.33$ (F. Incropera et al., 2007). The forced convection coefficients are used in Chapter 5 to understand the effect of increasing the HTF velocity on the melting and solidification patterns of the PCM. The convection coefficients are given in Fig. 4.2 as a function of the flow rate for both the hot and cold HTFs.

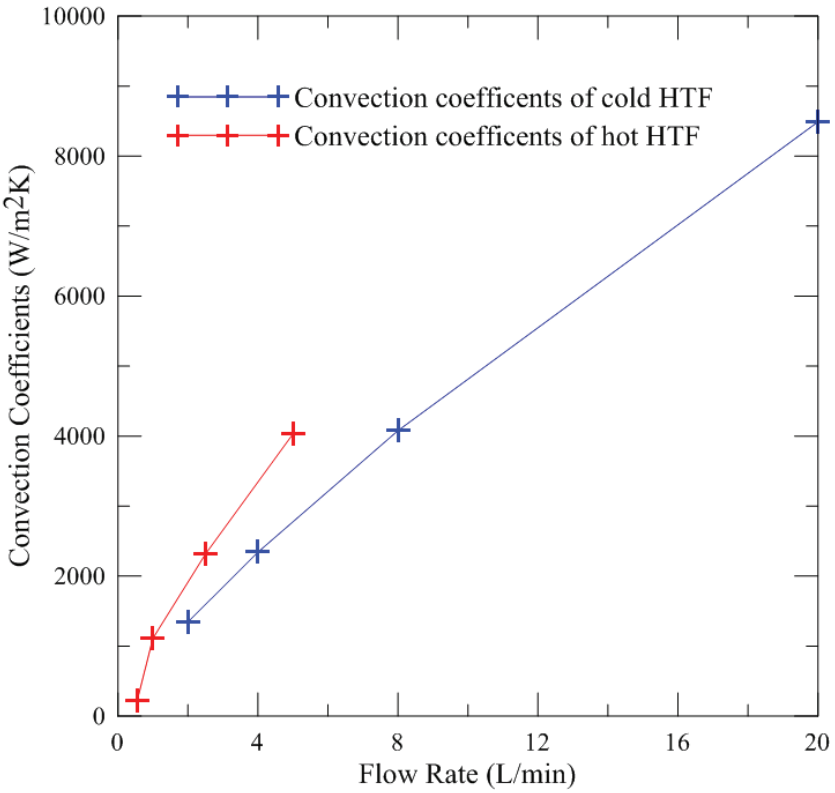


**Figure 4.2: Forced convection coefficients as a function of HTF flow rate for the hot and cold HTF**

The flow rates of the hot HTF are lower than those of the cold HTF throughout this thesis to reflect the flow rates observed in a SDHW system with LHESS, as discussed in Chapter 6. All of the flow rates result in turbulent flow, except the lowest flow rate used for the hot HTF (0.55 L/min), which results in laminar flow. The convection coefficient is noticeably lower for laminar flow, as seen in Fig. 4.2.

### *4.4 Heat Losses*

When the PCM is fully melted and the hot HTF is constantly circulated to keep the system hot, the additional energy input to the LHESS must replace the heat lost through the container wall. Heat losses ($\dot{Q}_{loss}$) were estimated by calculating the energy input when the PCM was fully melted and the hot HTF (at 58 ± 0.5˚C) was continuously circulated. This experiment was performed twice, and the results obtained are given in Table 4.2.

**Table 4.3: Heat losses**

| Experiment | Time kept at steady state | Energy input at steady state | Equivalent heat losses |
|---|---|---|---|
| 1 | 22.1 hours | 1700 kJ ± 46 % | 21 W ± 46 % at 57 $^{o}$C |
| 2 | 21.6 hours | 1697 kJ± 42 % | 22 W ± 42 % at 57 $^{o}$C |

At 20 $^{o}$C (assumed ambient room temperature, $T_{amb}$) there are no heat losses because there is no temperature difference between the PCM and the surroundings to drive heat transfer from one to the other. Therefore, assuming heat transfer varies linearly, a linear equation can be used to estimate the heat lost through the PCM container wall (in watts) during charging/discharging. This linear equation is given in Eq. (4.6), with an ambient room temperature of $T_{amb}$.

$$\dot{Q}_{loss} = \frac{21}{(60-T_{amb})}(T_{PCM} - T_{amb}). \quad (4.6)$$

The temperature of the PCM ($T_{PCM}$) is not the same everywhere in the LHESS, and therefore the average temperature recorded by all nine thermocouple probes was used to estimate the heat losses, making them a rough estimation.

## *4.5 Uncertainty Analysis*

Both bias and precision uncertainty are present in the work presented throughout this thesis.

### 4.5.1 Sources of Bias Uncertainty

Bias uncertainty can either be scale or offset uncertainty. In the experiments presented, the scale uncertainty is much smaller than the offset uncertainty, over the temperature range expected, and can therefore be neglected. The offset uncertainty in this work comes from the thermocouple and flow meter readings. These uncertainty values are given by the manufacturer for the flow meters and thermocouples T1-T15, and are based on the calibration discussed in Section 3.2.1 for the inlet and outlet thermocouples (T16-T19).

**Table 4.4: Offset uncertainty in measurements**

| Device | Offset Uncertainty |
|---|---|
| Thermocouple uncertainty T1-T15 ($\delta_{T1}$-$\delta_{T15}$) | ± 0.5 $^{o}$C |
| Thermocouple uncertainty T16 - T19 ($\delta_{T16}$-$\delta_{T19}$) | ± 0.45 $^{o}$C |
| Flow meter uncertainty ($\delta_{\dot{m}}$) | ± 2% of reading |

In the case of thermocouples T1-T15, the measured temperatures during the experiment range from 10 to 60 $^{o}$C, and therefore the uncertainty based on the above offset uncertainty values given by the manufacturer vary from 0.8 % to 5 % of the thermocouple readings. These values are reasonable for an experimental study, and are not further discussed in the results section.

However, the uncertainties in the energy calculations are significant and need to be considered. An example of the propagation of these uncertainties through the equation used to calculate the energy input/recovered experimentally (as seen in Section 4.2) is given in Appendix E. The energy values presented in Chapters 5 and 6 are given by Eq. (4.7).

$$Q = t\dot{m}Cp_{water}\Delta T \pm \delta_{\dot{Q}}. \quad (4.7)$$

Where $Q$ is the energy input/recovered and $\delta_Q$ is the uncertainty in the energy input/recovered. Since the uncertainty in $\Delta T$ is different for the hot and cold HTF, the energy equation can be broken into separate equations for charging ( $Q_{input}$ ) and discharging ($Q_{recovered}$ ). The uncertainty for each of these is given by Eq. (4.8) and Eq. (4.9).

$$\delta_{Qinput} = tCp_{water}\sqrt{(\Delta T\delta_{\dot{m}})^2 + (-\dot{m}\delta_{T18})^2 + (\dot{m}\delta_{T19})^2}. \quad (4.8)$$

and

$$\delta_{Qrecovered} = tCp_{water}\sqrt{(\Delta T\delta_{\dot{m}})^2 + (-\dot{m}\delta_{T16})^2 + (\dot{m}\delta_{T17})^2}. \quad (4.9)$$

These equations are used in results section (Chapter 5 and 6), and shown in Appendix E, to calculate the uncertainty in the energy calculated for each charging/discharging experiment, and during the simultaneous charging/discharging experiments.

### 4.5.2 Sources of Precision Uncertainty

Sources of precision error include fluctuations in municipal water supply and ambient air temperature. These uncertainties are difficult to quantify. Based on the plots shown in Appendix A, the precision error is significantly smaller than the bias error since the thermocouple measurements were off by close to the same amount each reading, even though they had an uncertainty of ± 0.45 $^{o}$C. For this reason precision uncertainty is not further discussed.

# Chapter 5 Results and Discussion: Separate Charging and Discharging

This chapter presents results when the experimental LHESS was charged and discharged separately to study the heat transfer patterns and phase change behavior during melting and solidification.

## *5.1 Experiments Performed*

The experiments performed, as well as the experimental parameters used, are outlined in Table 5.1:

**Table 5.1: List of experiments performed and the experimental parameters used**

| Experiment Number | Consecutive Charging and Discharging Experiments | Location in Thesis | Flow Rate | Inlet HTF Temperature |
|---|---|---|---|---|
| 1 | Repeatability experiment | Section 5.2 | 0.55 ± 0.01 L/min | 58 ± 0.5˚C |
| 2 | Charging experiment | Section 5.4 | 0.55 ± 0.01 L/min | 58 ± 0.5˚C |
| 3 | Charging experiment | Section 5.4.2 | various flow rates | 58 ± 0.5˚C |
| 4 | Charging experiment (hot HTF inlet at bottom) | Section 5.4.3 | 0.55 ± 0.01 L/min | 58 ± 0.5˚C |
| 5 | Discharging experiment | Section 5.5 | 3.5 ± 0.07 L/min | 10 ± 0.5˚C |
| 6 | Discharging experiment | Section 5.5.1 | various flow rates | 10 ± 0.5˚C |
| 7 | Discharging experiment (varying insulation thickness) | Section 5.5.2 | 3.5 ± 0.07 L/min | 10 ± 0.5˚C |

The hot and cold inlet HTF temperatures remained the same for all experiments in this thesis; however, the flow rates varied, as given in Table 5.1. The inlet/outlet temperatures can also be characterized by a dimensionless number called the Stefan number, which is given in Eq. (5.1) (F. Incropera et al., 2007).

$$\text{Ste} = C_p \Delta T / \Delta h_m. \quad (5.1)$$

For melting, $\Delta T$ is the difference between the inlet hot HTF temperature and the PCM melting temperature, and for solidification $\Delta T$ is the difference between the melting temperature and the

inlet cold HTF temperature. In systems with phase transitions, the Stefan number is the ratio of sensible heat to latent heat. In the system presented in this thesis, the Stefan number is small due to the small specific heat capacity ($C_p$) and small temperature difference ($\Delta T$), compared to the large latent heat of fusion of the PCM ($\Delta h_m$). For the experiments presented in Chapter 5, the Stefan number for melting is 0.17 ± 3 %, and the Stefan number for solidification is 0.43 ± 1 %.

### *5.2 Repeatability*

Complete charging of the LHESS was performed three times using the experimental parameters given in Table 5.1 in order to show that the experimental results are reproducible. The 0.55 L/min hot HTF flow rate, given in Table 5.1, was determined experimentally to result in lower uncertainty in the energy calculations than higher flow rates. The experiments produced repeatable results, as seen in Fig. 5.1, for three charging experiments (1, 2, and 3).

a)

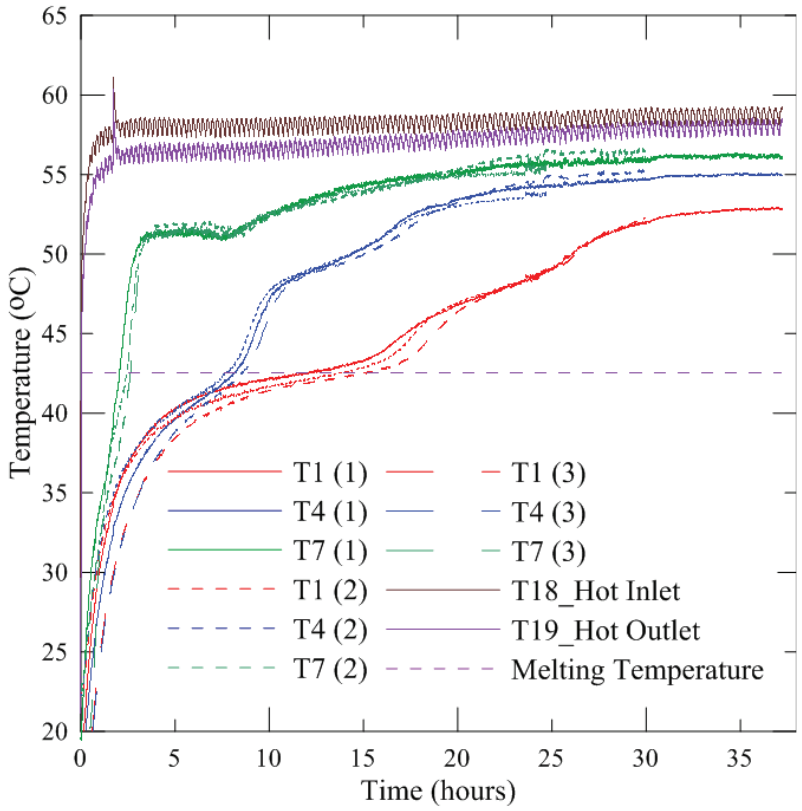


**Figure 5.1: Temperature profiles as a function of time measured during charging for three identical experiments: a) Middle probes T1, T4 and T7 (0.55 L/min flow rate)**

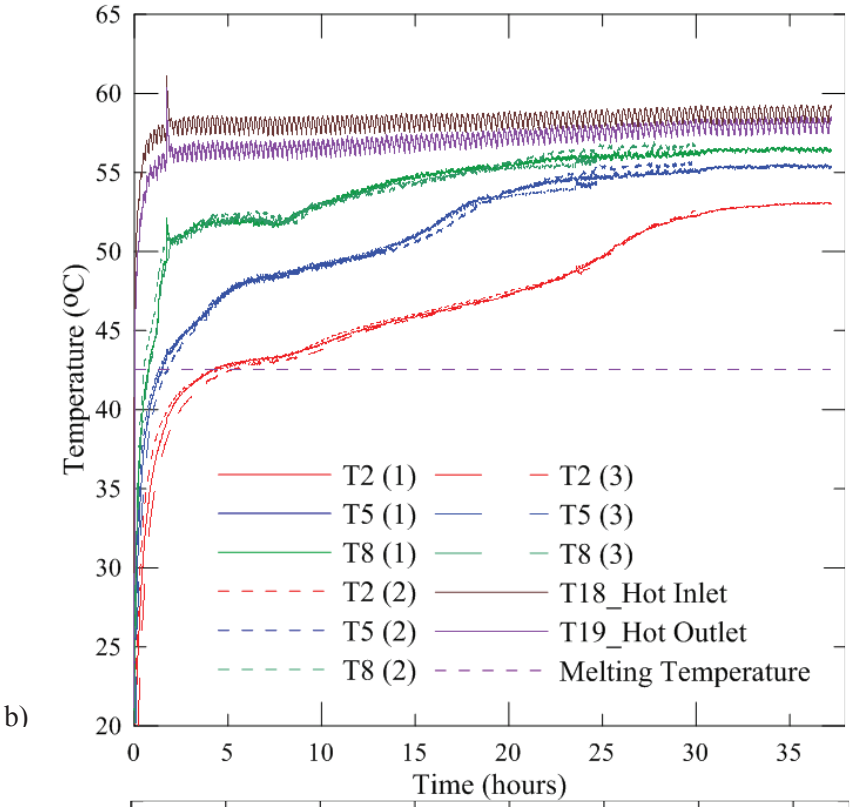


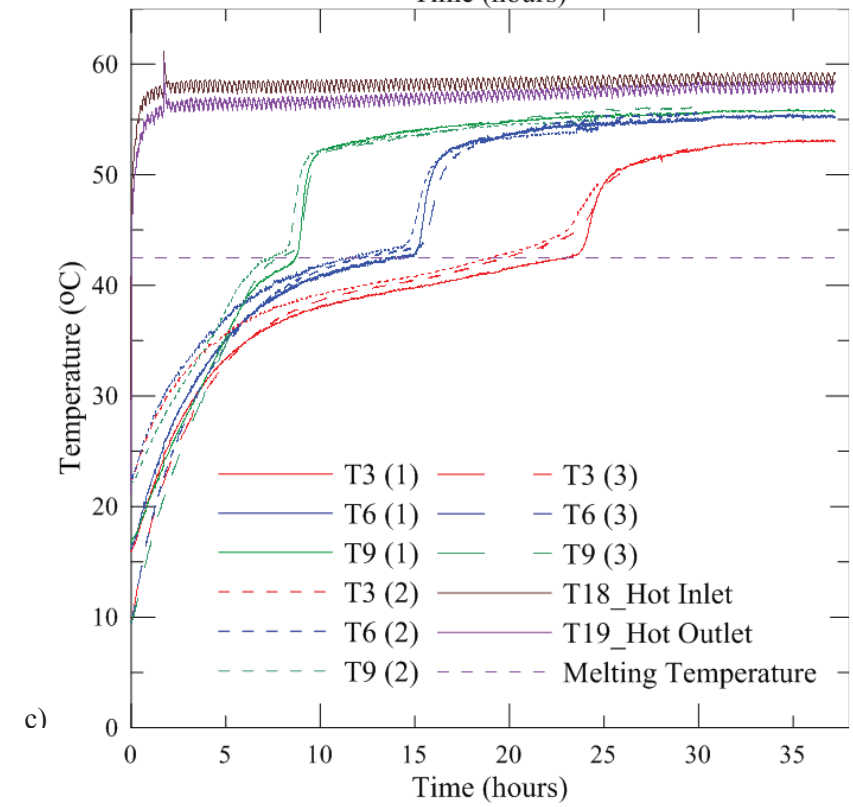


**Figure 5.1: Temperature profiles as a function of time measured during charging for three identical experiments: b) Hot-side probes T2, T5 and T8 c) Cold-side probes T3, T6 and T9, continued**

The PCM temperatures measured by the thermocouple probes (T1 to T9) reached steady values after approximately 30 hours of charging, with complete melting of the PCM after 38 hours, upon observation. From Fig. 5.1 the same temperature profiles were observed in each of the three charging experiments, demonstrating the repeatability of the experiment. The 58 ± 0.5˚C inlet temperature is the average over the experiment, as it is clear from Fig. 5.1 that the inlet temperature is subject to fluctuations due to the immersion heater switching on and off.

### *5.3 Symmetry*

The LHESS was designed to be symmetrical about the line of symmetry shown in Fig. 5.2-a). Symmetry in the system is useful because it means that the PCM temperatures on one side of the LHESS (on one side of the line of symmetry) can be predicted by the thermocouple probes on the opposite side of the container. Therefore, PCM temperatures at two points in the LHESS can be obtained using a single thermocouple probe. Also, a numerical model representing the experimental LHESS can be symmetrical, which may reduce computing time. Figure 5.2-b) shows a photograph taken after 15 hours of charging.

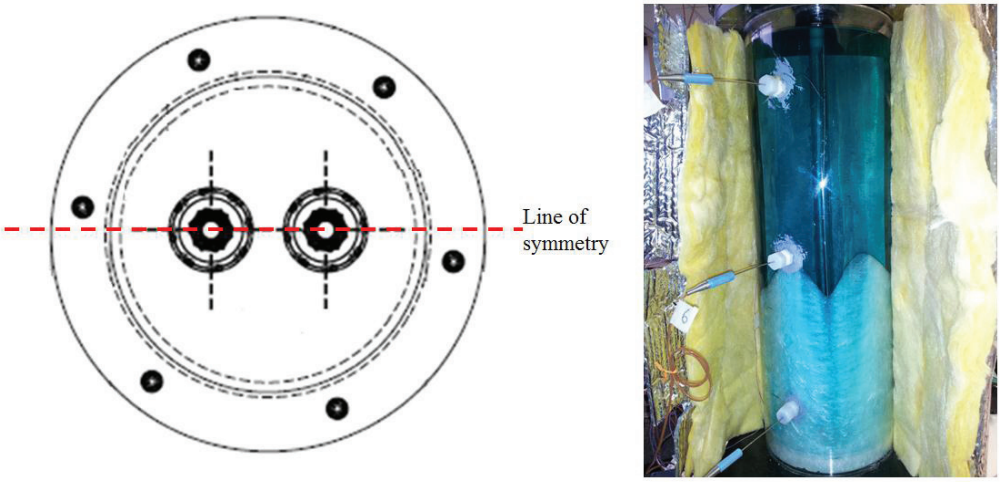


a) b)

**Figure 5.2: a) Line of symmetry in LHESS b) Photograph of the symmetry in the system taken after 15 hours of charging the LHESS**

Upon observation of the photograph in Fig. 5.2-b), there is symmetry in the system.

Section 5.2 shows that experimental results are repeatable, therefore both the complete charging (Section 5.4) and complete discharging (Section 5.5) experiments were run twice using the same operating parameters (flow rates and temperatures) but with the thermocouple probes (T1-T9) at two different depths in the PCM. Varying the depth of the thermocouples allows temperature measurements to be taken using the thermocouple probes at 18 locations for each set of experiments. Figure 5.3 shows the locations of the thermocouple probes and their distance, *R*, from the center-point of the LHESS.

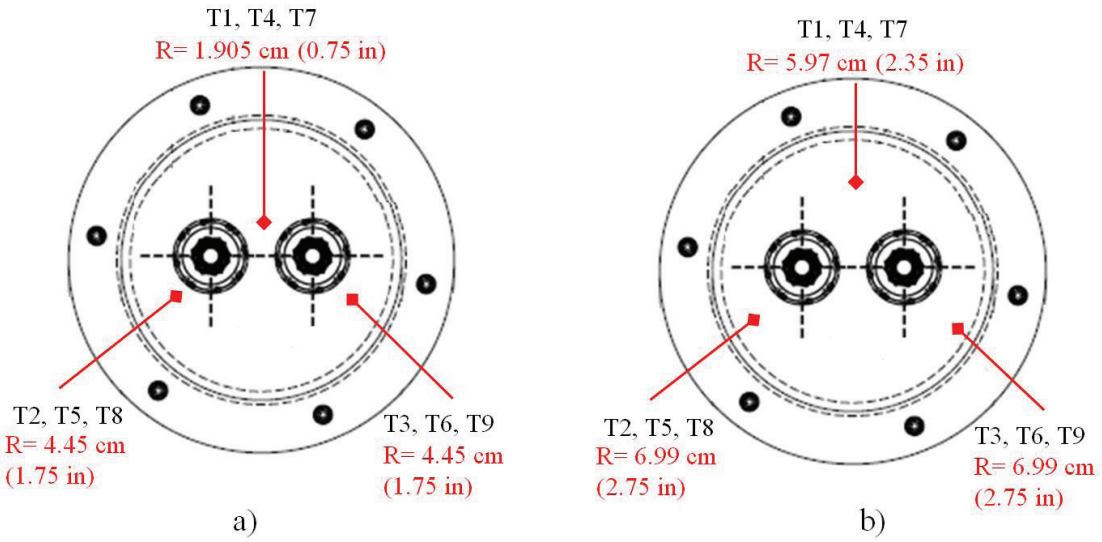


**Figure 5.3: a) First thermocouple probe depth b) Second thermocouple probe depth, given by the distance of the probe from the center-point of the LHESS**

As a result of symmetry in the system, and by running each experiment twice using the two probe depths, a total of 36 temperature points can be identified throughout the PCM.

### *5.4 Complete Charging*

Complete charging of the LHESS was performed to study the phase change behavior of the PCM and the heat transfer patterns throughout the system. As well, the energy storage capacity calculated during the charging experiment was compared to the theoretical energy storage capacity of the PCM. The experimental parameters used are given in Table 5.1.

Figure 5.4 shows the temperature measurements taken by the thermocouple probes (T1 to T9) during the melting process for two experiments with the probes at different depths into the PCM, as given in Fig. 5.3. The time required for all of the thermocouple probes to record melting was approximately 26 hours, with complete melting of the PCM after 38 hours.

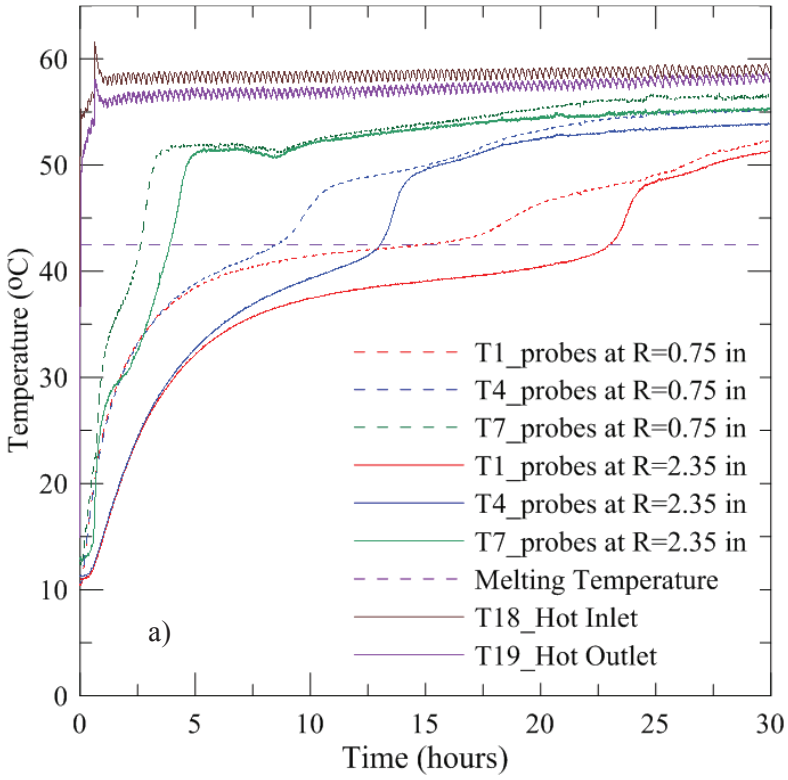


**Figure 5.4: Temperature profiles as a function of time measured during charging: a) Middle probes T1, T4 and T7 (0.55 L/min flow rate)**

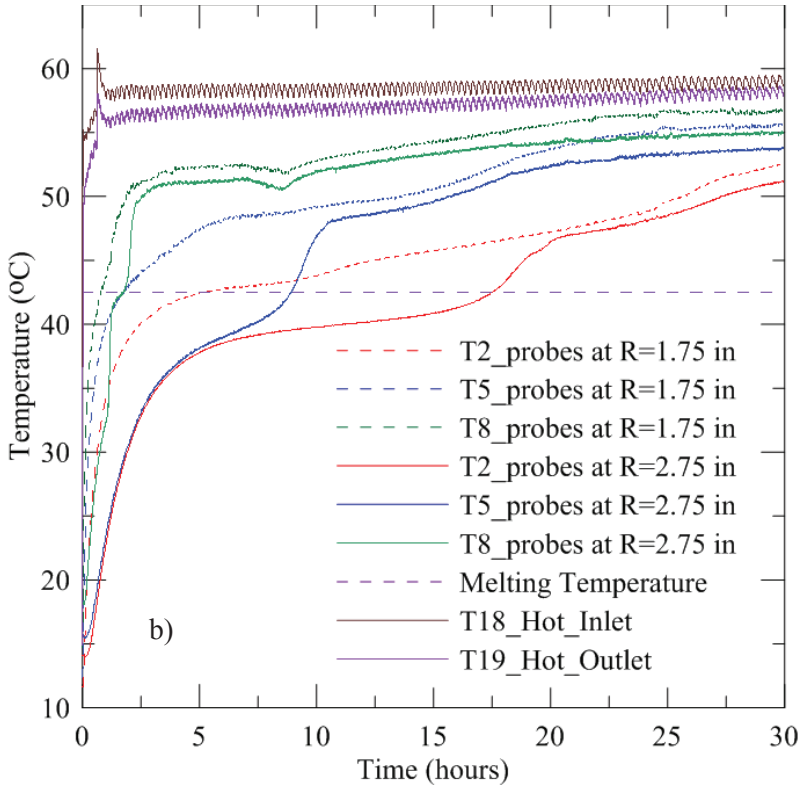


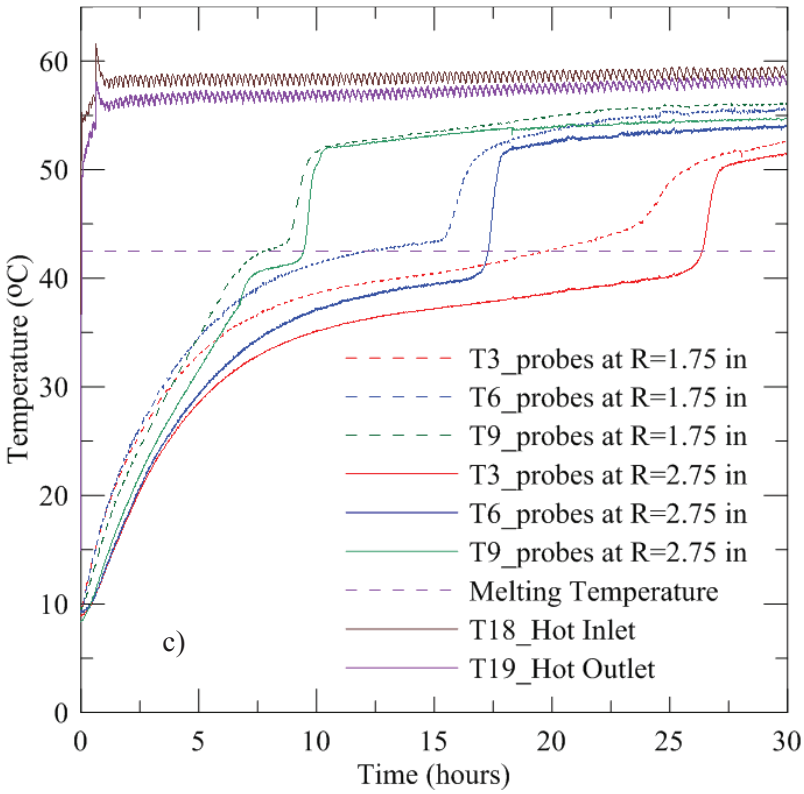


**Figure 5.4: Temperature profiles as a function of time measured during charging: b) Hot-side probes T2, T5 and T8 c) Cold-side probes T3, T6 and T9 (0.55 L/min flow rate), continued**

In Fig. 5.4-a), which shows the temperature profiles recorded by the middle thermocouple probes, the PCM closer to the heat source (at R=0.75 in) initially heats faster than the PCM farther away from the heat source (at R=2.35 in) due to the proximity of the PCM to the hot HTF. This is clear when comparing the dashed lines to the solid lines in Fig. 5.4-a). For both probe depths, the PCM initially heats up at a rate independent of the thermocouple probe height. This indicates that conduction is the main mechanism of heat transfer in the solid PCM which is not subject to the gravity effects observed with convective heat transfer. Once melting begins, the PCM at the top of the LHESS (T7) melts faster than the PCM at the middle (T4) and bottom (T1). This occurs because, as melting begins, more energy is displaced upward by natural convection, causing more melted PCM to move upwards to the top of the container. The picture in Fig. 5.5 shows the melted PCM in the top half of the LHESS after 20 hours of charging during one of the preliminary experiments with no insulation. The same pattern was observed in the experiment with the system fully insulated.

**Figure 5.5: Photograph of system charging after 20 hours (no insulation for observation)**

In Fig. 5.5 the PCM is blue due to a reaction with the copper pipe and fins. Further investigation into this reaction is required; however, it is thought to be a mild reaction with the PCM becoming saturated after the first couple melting/solidification cycles (Murray et al., 2011). The melted PCM at the top of the container stimulated more of the solid PCM at this height to melt, and this cycle continued until all of the PCM at the top of the LHESS was melted, as seen in Fig. 5.5. This pattern is in agreement with the temperature profiles shown in Figures 5.4-a), b) and c) in which the PCM at the top heights (green lines) melt before the PCM at the middle (blue lines) and the bottom (red lines). On the side with the hot HTF pipe, the PCM heated up and melted faster than it did in middle and on the side of the cold HTF pipe (all probes reading over the melting temperature in 16 hours compared to 24 and 26 hours for the middle and cold-side, respectively). This is due to the close proximity of the PCM on the side of the hot HTF pipe to the heat source.

Although melting does not occur until the PCM reaches 42.5 $^{o}$C, the temperature profiles measured by the thermocouple probes begin to flatten after 35 $^{o}$C. This is clearly shown by T3 (red lines in Fig. 5.4-c)) and is a result of the influence of the PCM in other areas of the system on the PCM directly in contact with the thermocouple probe. The amount of energy required to melt the PCM is several orders of magnitude larger than the energy required to simply raise the temperature of the material (as discussed in Section 1.1). As the melting front proceeds toward the thermocouple probe, two things happen: 1) a large portion of the energy from the hot HTF is required to melt the PCM directly at the melting front, and 2) the temperature difference between the heat source and the PCM at the probe location decreases as charging proceeds. As a result, less energy goes to the PCM at the probe location, causing the temperature increase of the material to slow down prior to melting, as recorded by the thermocouple probes in Fig. 5.4. Once melting is complete, the PCM at the probe location increases in temperature quickly due to significantly less energy required to simply heat the PCM compared to the energy required for melting, and the more rapid exchange of energy by convection once the PCM is melted. As well,

the small Stefan number for melting (0.17 ± 3 %) indicates that the effect of sensible heat transfer on the motion of the PCM melting front is weak, which explains the slower increase in PCM temperatures before melting.

In Fig. 5.4-c), the constant temperature phase transition plateaus were clearer due to the longer melting time required. However, the phase transition plateaus which are normally observed during melting were not clear for all probe locations. Thermocouple measurements in the experiment became affected by poor contact with the solid PCM due to the slight volume change from solidification. This slowed thermocouple response and did not result in the necessary resolution to observe clear phase change plateaus. However, this poor contact was improved once the PCM melted. The effects of natural convection in the case of the hot-side thermocouple probes, as seen in Fig. 5.4-b), caused the PCM to melt too rapidly for phase transition plateaus to be observed.

In Figures 5.4-a) ,b) and c) the inlet hot HTF (T18-brown lines) and outlet hot HTF (T19-purple lines) temperature difference is less than 2 $^{o}$C, which means the hot HTF does not decrease in temperature significantly from the entrance to the exit of the LHESS. This demonstrates again the effects of natural convection, since the variation in the temperature of the PCM over the height of the LHESS must be caused by natural convection, not as a result of more energy in the hot HTF at the top of the LHESS. This is clearly established in Section 5.4.3 in which the system was charged with the inlet of the hot HTF at the bottom of the LHESS.

The temperature measurements taken at the two thermocouple probe depths demonstrated that melting took place from the hot HTF pipe surface outward. The four adhesive thermocouples (T10-T13) located on the HTF pipe fins at the top height of the LHESS recorded temperatures during charging. These temperature profiles are given in Fig. 5.6.

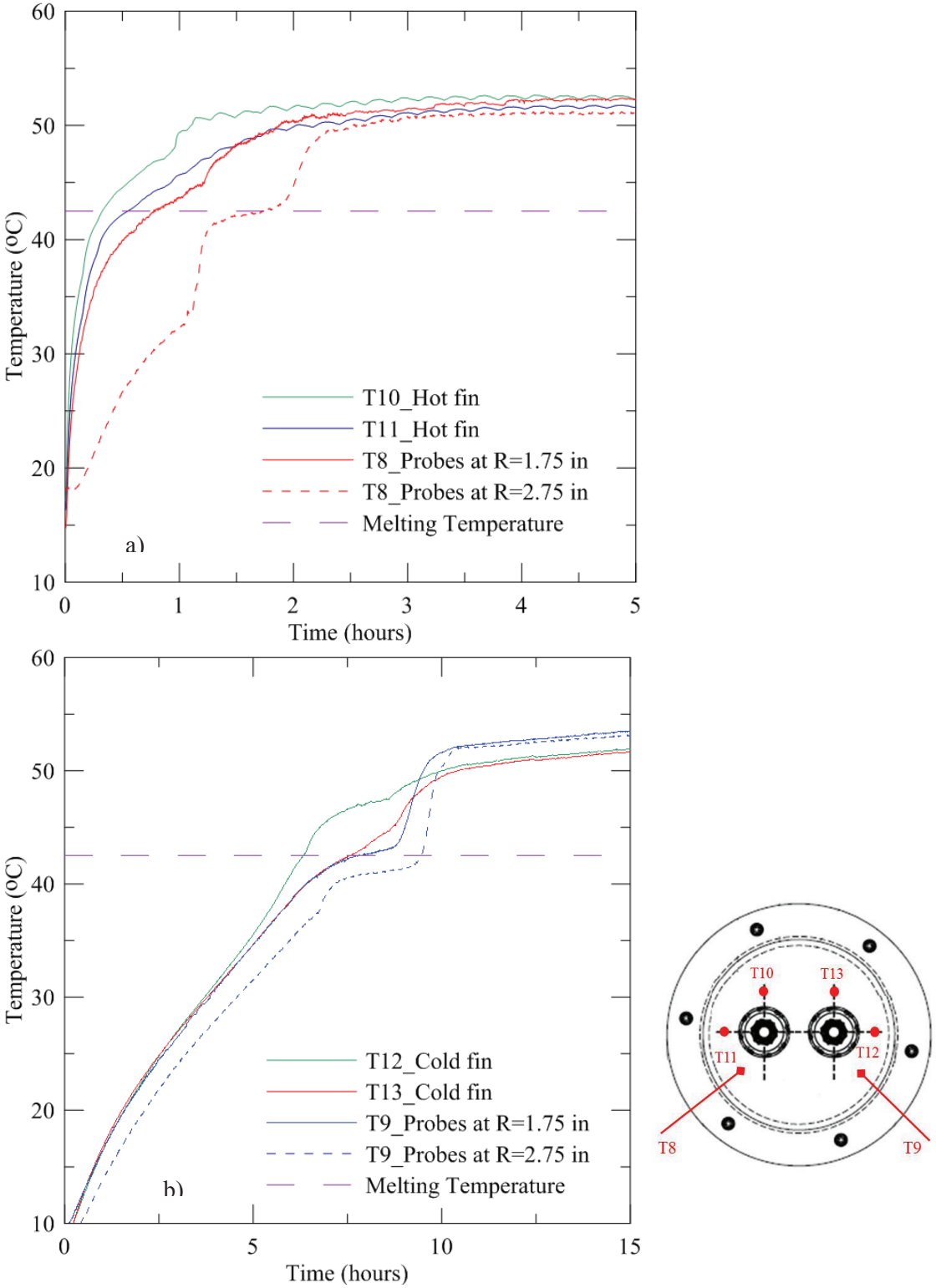


**Figure 5.6: Temperature profiles as a function of time measured during charging a) Hot-side fin and probe thermocouples b) Cold-side fin and probe thermocouples**

In Fig. 5.6-a) the PCM around the fins on the hot HTF pipe (T10 and T11) heated up and melted before the PCM at the probe location close to the hot HTF pipe at the same height (T8). In Fig. 5.6-b) the PCM around the fins on the cold HTF pipe (T12 and T13) heated up and melted at the same time as the PCM at the probe locations at that height (T9). This indicates that the fins improved heat transfer from the pipe to the PCM during melting, since the PCM melted around the fins first on the side of the hot HTF pipe. The addition of the fins on the cold HTF pipe did not enhance heat transfer on the side of the cold pipe because these fins were not in contact with the heat source, and were separated from the heat source by the high thermal resistance PCM. However, the fins on the cold HTF pipe closest to the hot HTF may have carried some heat from the melted PCM on that side of the cold HTF to the other side. In order to clearly determine the effects of the fins, the same experiments would need to be repeated with no fins.

### *Energy and Power Input*

The total energy transferred from the hot water to the PCM was 5690 kJ ± 46 % and 5080 kJ ± 52 % for experiment one and two, respectively, as shown in Fig. 5.7. This is the energy input to the LHESS by the hot HTF, calculated by Eq. (4.2) and does not take into account the heat losses through the container wall, which are discussed in detail later in Section 5.4.

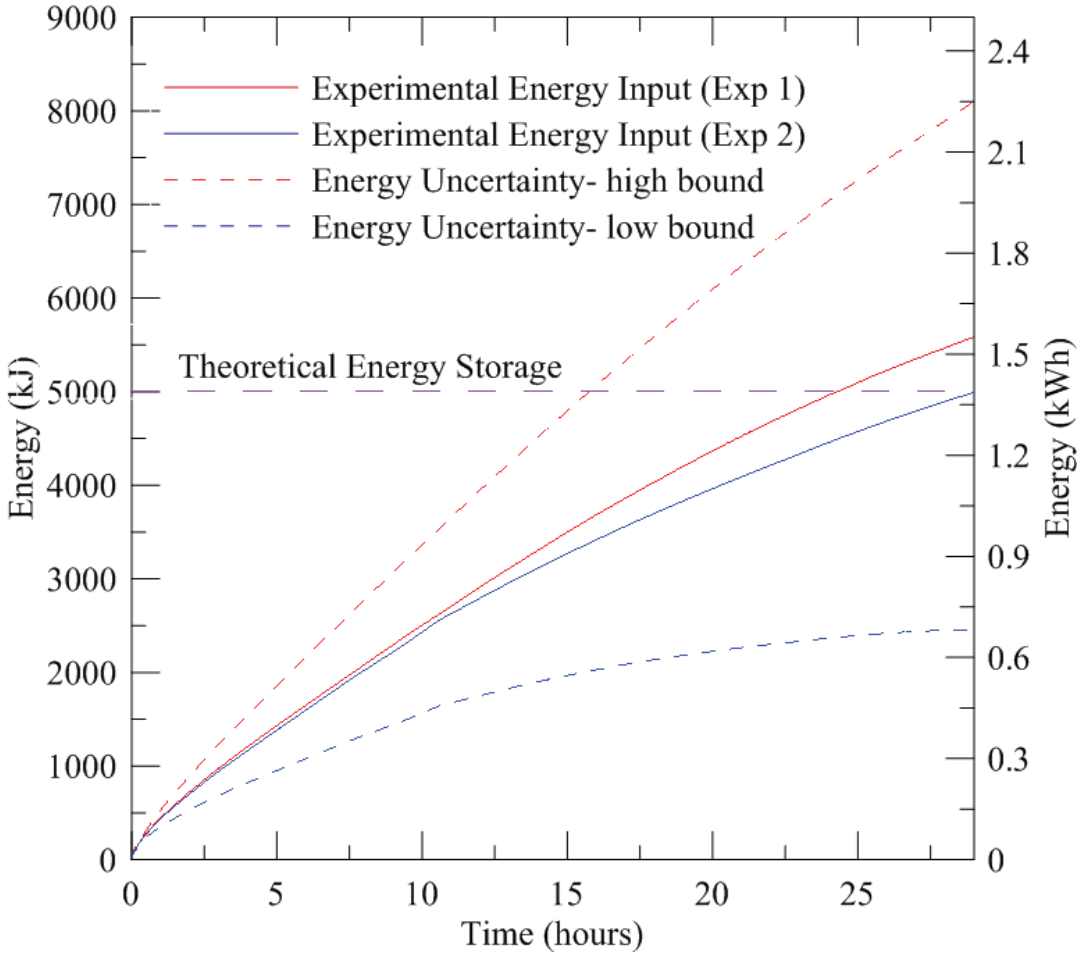


**Figure 5.7: Energy input as a function of time during charging experiment (0.55 L/min flow rate)**

The theoretical energy storage capacity of the system was shown in Section 4.1 to be 5000 kJ ± 6%. It is expected that this theoretical energy capacity be reached at the end of the charging period, when all the PCM has melted. Although the uncertainty is large, the energy calculated from experimental data is similar to the theoretical energy storage capacity, verifying the experimental energy values and providing greater confidence in the calculated energy input than the uncertainty based on equipment manufacturers values would lead one to believe.

The power capacity of the system during charging is a good indication of the suitability of the LHESS for use with SDHW. Figure 5.8 shows the power input over the two experiments.

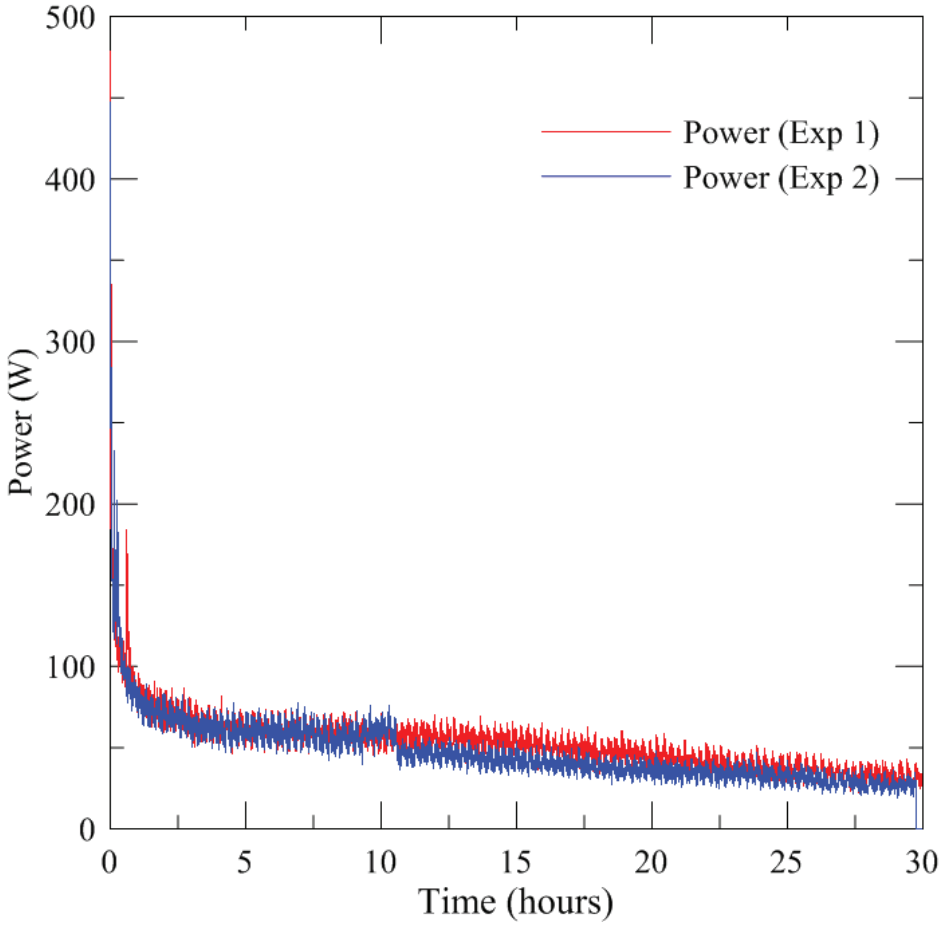


**Figure 5.8: Power as a function of time during charging experiment (0.55 L/min)**

The power input experimentally during charging is low due to the long charging times. The average power output of a single flat plate solar collector is 480 W in Halifax. This is assuming the collector is 3 $m^2$ (Thermo-Dynamics, 2011), 40 % efficient, with an average daily insolation in Halifax of 3.3 $kWh/m^2$ (NRCan, 2012). This means that the average power input by the hot HTF to the PCM, which is 53 W, is 13 % of the average power output of a single flat plate solar collector. For a LHESS to be used commercially, the power capacity of the system has to match the expected power output from the SDHW. The expected power output from a SDHW varies over the day, with an average power output of 480 W, but with daily peaks of up to 1400 W for the same solar collector, as seen in Fig. 5.9.

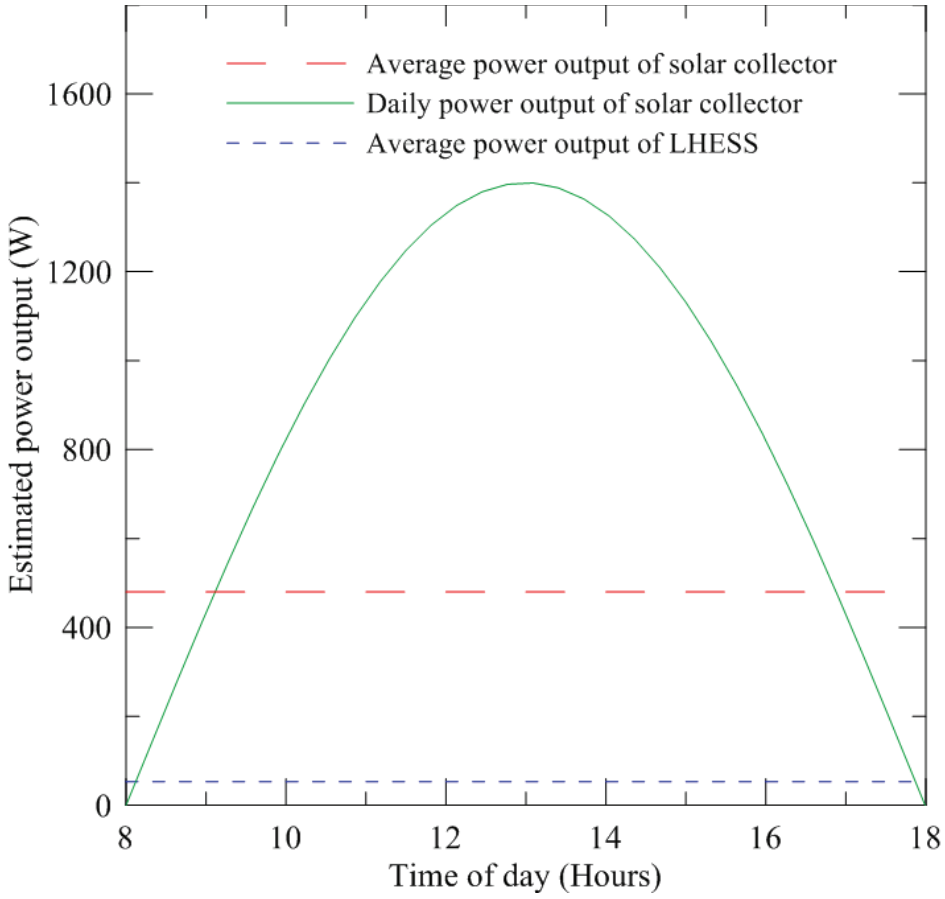


**Figure 5.9: Power output of flat plate solar collector compared to LHESS power**

This variation in power output over the day as the solar insolation varies is something that needs to be considered when designing a LHESS for the power capacity of a SDHW system. This issue is further discussed in Chapter 7.

The heat flux from the hot HTF during charging, as a function of the heat transfer surface area, is given in Fig. 5.10. The heat transfer surface area (surface area of the copper pipe in the PCM) is 0.00772 $m^2$.

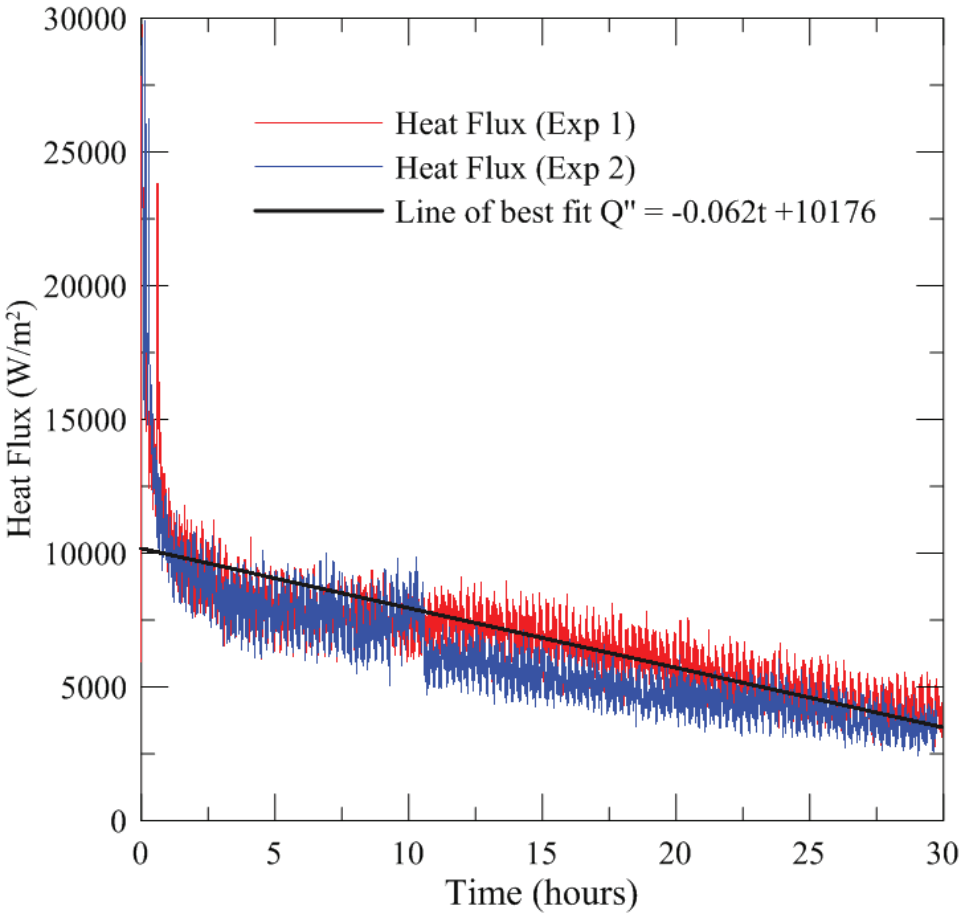


**Figure 5.10: Heat flux as a function of time during charging experiment (0.55 L/min)**

As seen in Fig. 5.10, the heat flux varies with time over the charging period. Using a linear regression the heat flux input from the hot HTF can be represented by Eq. (5.2).

$$Q''_{input} = -0.066t + 10176. \quad (5.2)$$

The largest heat flux occurs in the first 30 minutes of the charging period. The PCM is initially solid at 10 °C; therefore, the initial temperature difference between the hot HTF and the PCM is largest at the beginning of the charging period. This results in the largest heat flux from the hot HTF to the PCM during the charging period. Knowing how the heat flux varies with time will allow for more accurate modeling of the heat source in future numerical models of this system.

### *Heat Losses*

Heat losses as a function of time over the charging period for the two experiments are shown in Fig. 5.10.

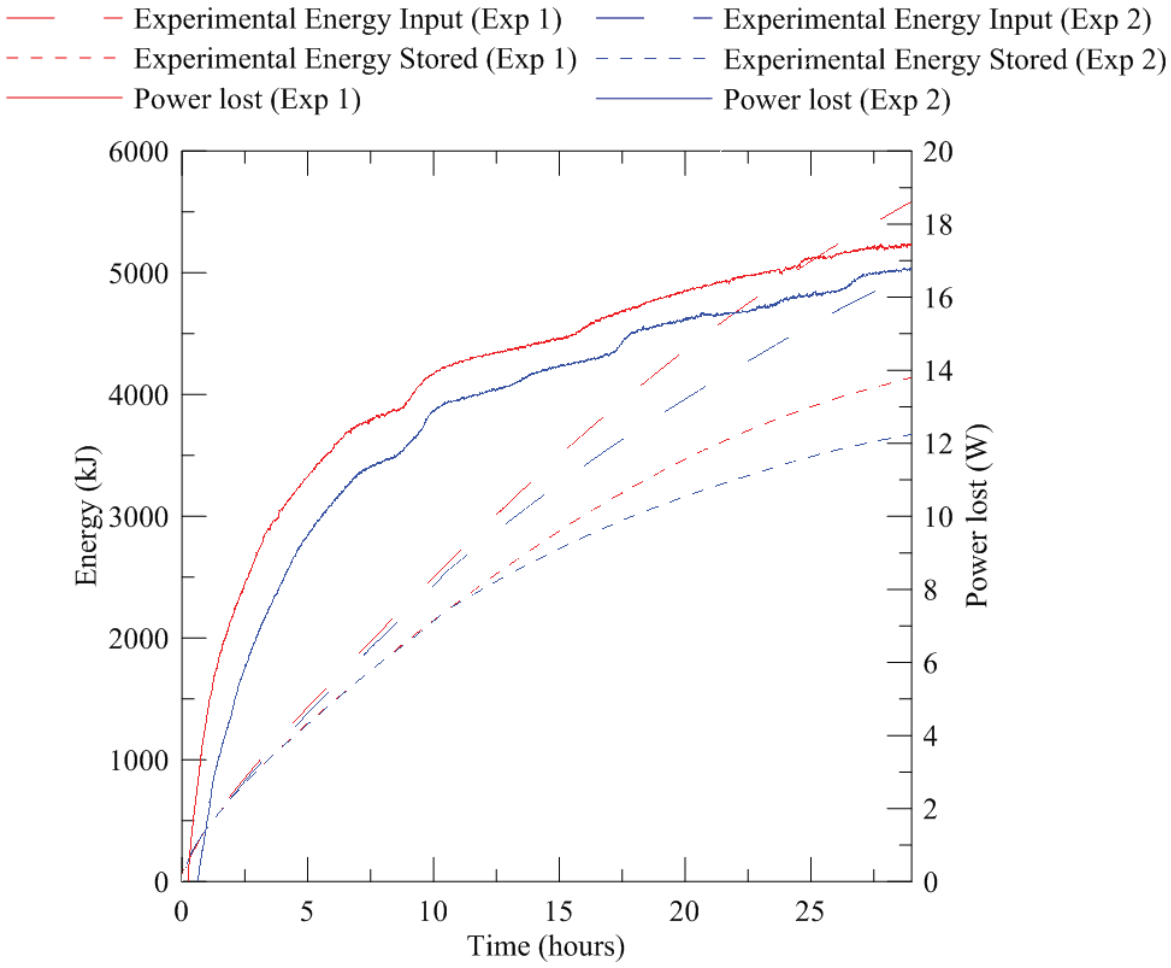


**Figure 5.11: Heat losses -Energy input and energy stored as a function of time**

In Fig. 5.11, the experimental energy input is presented and is the same energy input as presented in Fig. 5.7, calculated by Eq. (4.1). The energy stored shown in Fig. 5.11 accounts for the heat lost through the container wall, calculated using Eq. (4.7), subtracted from the energy input by the hot HTF. As the experiment proceeds, the heat losses increase due to an increasing temperature difference between the PCM and the surroundings. Figure 5.5 shows that the PCM close to the container wall is the last to melt, therefore the solid PCM insulates the remaining PCM inside the

system until close to the end of the charging period. The heat losses shown in Fig. 5.11 are calculated using a PCM temperature averaged over the ones recorded by the nine thermocouple probes over the charging experiment. Because of the insulation provided by the solid PCM on the inner container wall, the average PCM temperature as measured by the probes will be an over estimation of the average PCM temperature. Therefore, these heat losses will be an over estimation of the heat losses through the container wall. The total energy lost over the entire charging period was 1500 kJ and 1360 kJ for experiment one and two consecutively, which accounts for 26 % and 27 % of the total energy input by the hot HTF. The percent of heat lost is still lower than the uncertainty in the energy calculations, therefore, heat losses through the container wall won't be discusses further in the remaining analysis of experimental results.

### 5.4.1 Numerical Study

The experimental results, using the second thermocouple probe depth given in Fig. 5.3-b), were compared to the conduction-only COMSOL numerical model. Figure 5.12 shows the comparison between the numerical results and the experimental results.

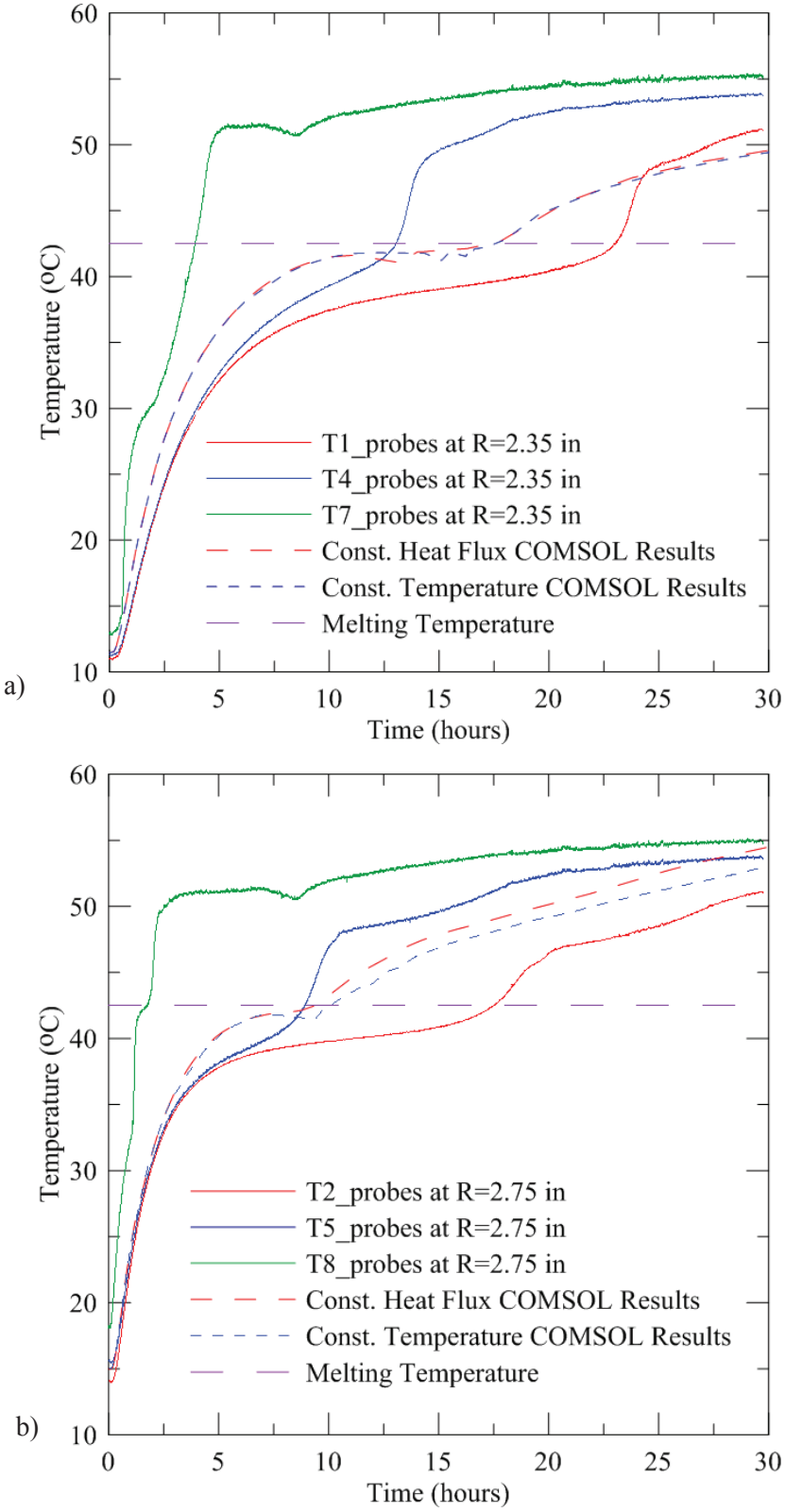


**Figure 5.12: Temperature profiles as a function of time measured during charging a) Middle probe thermocouples T1, T4 and T7 b) Hot-side probes T2, T5 and T8, comparing results to COMSOL**

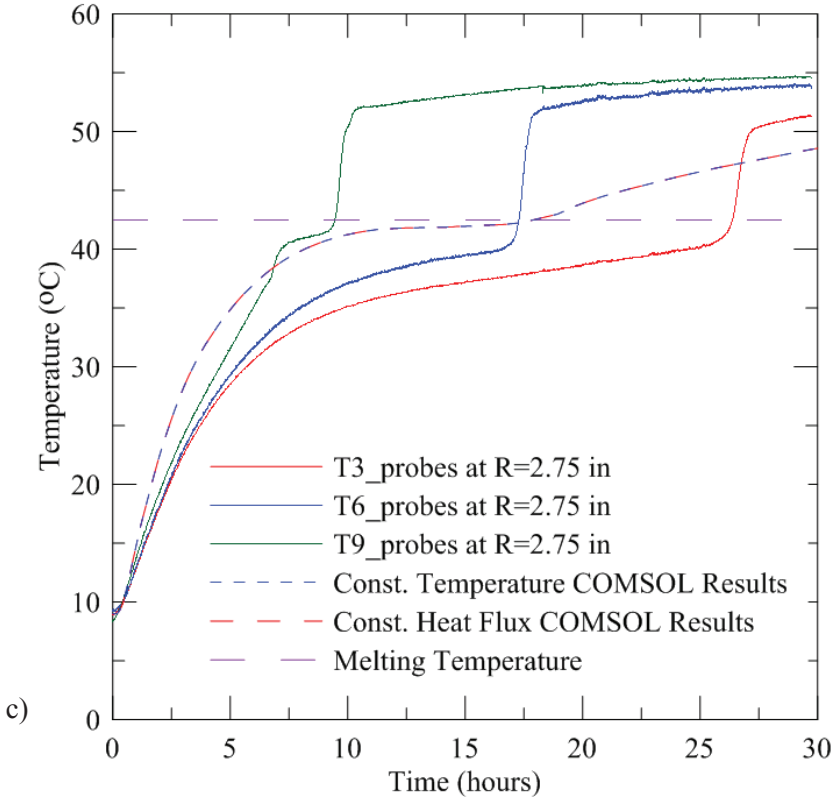


**Figure 5.12: Temperature profiles as a function of time measured during charging c) Cold-side probes T3, T6 and T9, comparing results to COMSOL, continued**

From Fig. 5.12, the PCM temperature profiles in the experiment are a close match to the temperature profiles given by the conduction only numerical model when the PCM is below 35 $^{o}$C. This confirms the results found in Section 5.4, which indicated that conduction is the only mechanism of heat transfer present early in the charging process. This also indicates that the numerical model is valid when the PCM is below about 35 $^{o}$C. The temperature profiles given by the numerical model for both the constant temperature and the constant heat flux methods of modeling the heat source are also a close match. This means both methods of modeling the heat source are acceptable, and confirms the forced convection coefficient calculated for the 0.55 L/min hot HTF flow rate (as presented in Section 4.3).

From Fig. 5.12, when the PCM is above 35 $^{o}$C, the temperature profiles begin to diverge from the numerical results, indicating the onset of natural convection in the experimental system. After

about 35 $^{o}$C, natural convection effects in melted PCM elsewhere in the system begin to influence the temperature profiles recorded by the thermocouple probes, which is discussed in Section 5.4. During and after melting, the thermocouple probes at the top of the LHESS in the experiment (T7, T8 and T9- green lines in Fig. 5.12) record higher temperatures and faster melting than the PCM in the same locations in the numerical model. This is due to the absence of natural convection in the numerical model. The lack of natural convection in the model means that heat transfer is limited by the low thermal conductivity of the PCM, resulting in poor conduction through the LHESS. Consequently, the PCM in the lower section of the experimental LHESS (T1, T2 and T3 –red lines in Fig. 5.12) takes longer to heat up and melt than the PCM in the COMSOL model because energy is displaced upward to the top of the LHESS by natural convection.

In the experiment, at the end of the charging period, 100 % of the PCM melted, upon observation. However, at the end of the simulation in the numerical model (after the same amount of charging time as in the experiment) only 87 % of the PCM was melted, as shown in Section 3.8. This is again due to the effects of natural convection speeding up the melting process in the experiment.

### 5.4.2 Effect of Flow Rate on Charging

The system was charged using various hot HTF flow rates to study the effect of the flow rate on the melting process. Plots of temperature as a function of time for various flow rates are shown in Fig. 5.13.

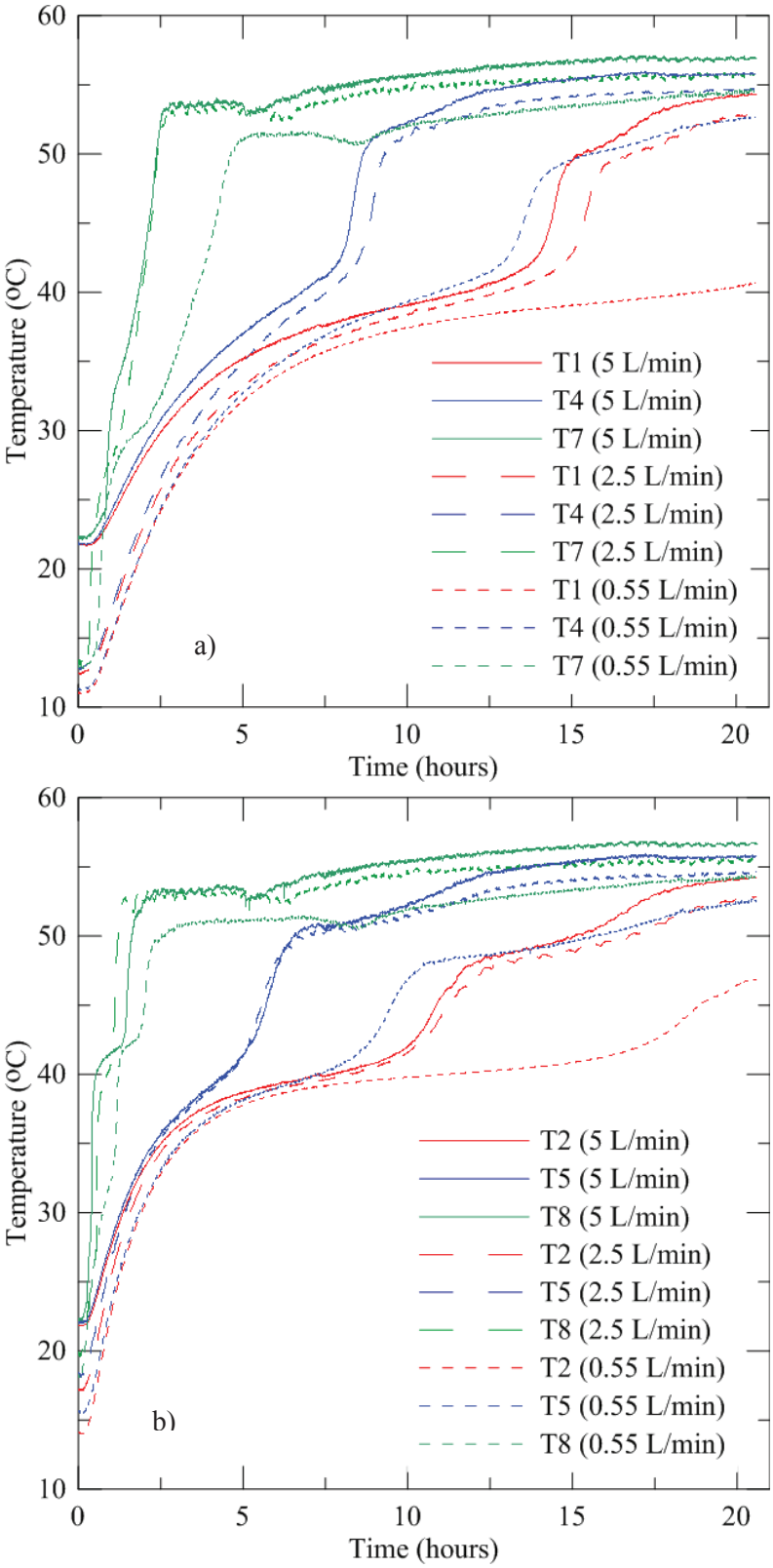


**Figure 5.13: Temperature profiles as a function of time measured during charging: a) Middle probes T1, T4 and T7 b) Hot-side probes T2, T5 and T8 (comparing flow rate)**

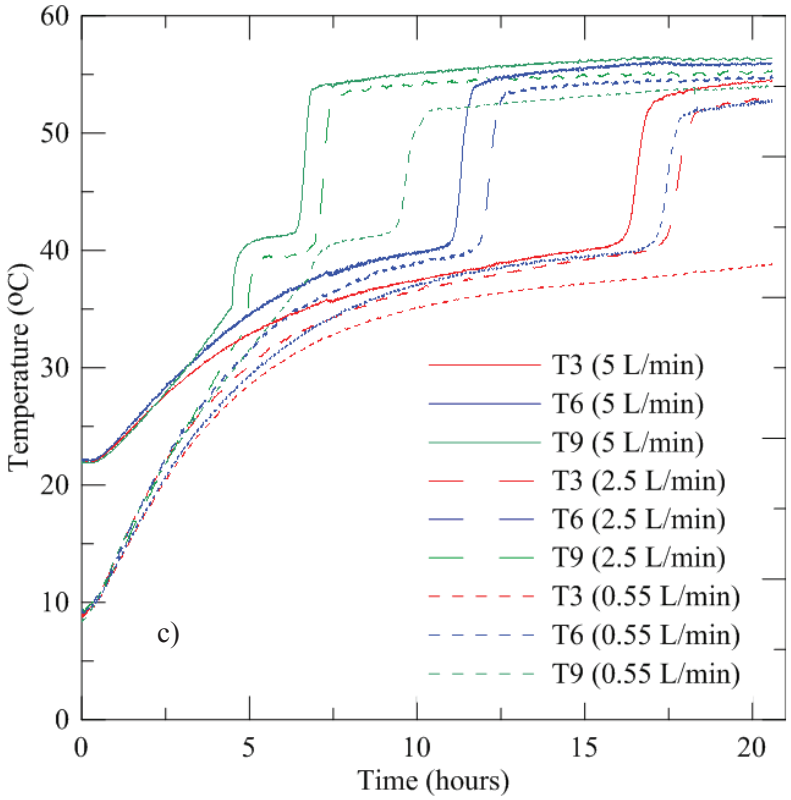


**Figure 5.13: Temperature profiles as a function of time measured during charging: c) Cold-side probes T3, T6 and T9 (comparing flow rate), continued**

Based on Fig. 5.13, the PCM melts more quickly as the flow rate increases. As shown previously, natural convection plays a major role during melting, and the above plot shows that forced convection inside the HTF pipe also plays a role in the heat transfer processes during charging. The forced convection coefficients were calculated and shown in Section 4.3 for the flow rates used. Based on Fig. 4.2, as the flow rate increases, the convection coefficient of the HTF inside the copper pipe increases as well; so increases the rate of convection heat transfer from the hot HTF increases to the system, as demonstrated by Newton's law of cooling, Eq. (5.3).

$$Q_{convection} = hA\Delta T. \tag{5.3}$$

The significantly lower heat transfer rates and longer melting times at 0.55 L/min is attributed to the significantly lower forced convection coefficient as a result of laminar flow, as shown in Fig.

4.2. When the PCM is initially solid, increasing the flow rate does not increase the rate of heat transfer until the PCM close to the hot HTF pipe has melted. This is clear in Fig. 5.13-b), where the PCM initially heats at the same rate independent of the flow rate, and the effect of the flow rate does not become evident until after melting. When the PCM is melted it can accommodate this increased energy transfer rate from the hot HTF by natural convection. However, quantifying the increase in natural convection in the PCM cannot be done using the experimental setup presented in this thesis. The best way to further study this phenomenon is to create a validated 3D numerical model of this system using the experimental data produced by this thesis research, which is discussed in the recommendations section in Chapter 7.

In Fig. 5.13-c), the initial PCM temperatures for the 5 L/min experiment are higher than the initial PCM temperatures in the 0.55 and 2.5 L/min experiments. Along with increased forced convection with the higher flow rate, the higher initial PCM temperature contributes to the faster melting of the PCM at the 5 L/min flow rate. The difference in PCM initial temperatures is a result of the experiments done prior to the charging experiment. For the 5 L/min experiment, the charging process was started when the system had been steady at room temperature for several days. However, for the 0.55 and 2.5 L/min experiments, charging was started directly after a discharging experiment was completed. During discharging, the temperatures of the PCM dropped below room temperature as a result of the low (10 $^{o}$C) inlet cold HTF temperature. However, the most significant difference in PCM melting time occurred for the 0.55 and 2.5 L/min experiments, which had the same initial PCM temperatures.

Faster melting of the PCM at higher flow rates may also be attributed to more energy being input to the system when the HTF is at a higher flow rate, resulting in a reduction in the time required for the PCM to melt and earlier onset of natural convection. Based on Eq. (4.1), as the flow rate increases the energy input to the LHESS from the hot HTF will increase as well.

### 5.4.3 Effect of Inlet Orientation on Charging

It was shown in the literature that for a vertical pipe-in-pipe LHESS that natural convection effects played a major role during melting when the HTF entered the container from the bottom of the LHESS, but these effects were not significant when the HTF entered from the top of the container (Ettouney et al., 2004). To verify this, the inlet orientation of the hot HTF was switched from the top of the LHESS to the bottom to determine the impact of inlet orientation on the heat transfer processes. The system was charged using the 0.55 L/min flow rate, as given in Table 5.1, to allow for direct comparison between the two inlet orientations. Figure 5.14 shows the results obtained during charging using both inlet orientations:

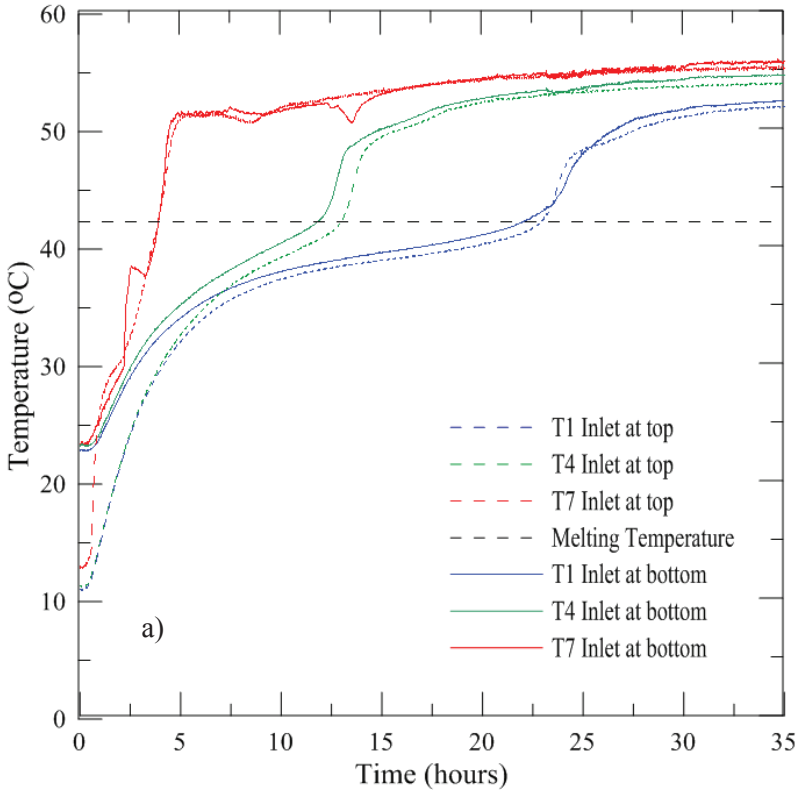


**Figure 5.14: Temperature profiles as a function of time measured during charging: a) Middle probes T1, T4 and T7 (comparing inlet orientation)**

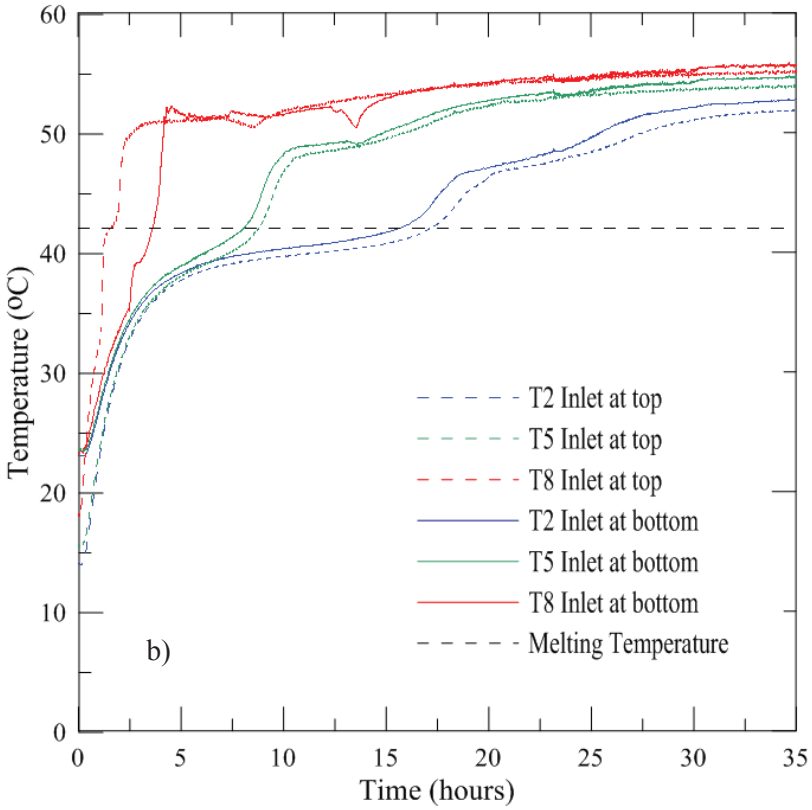


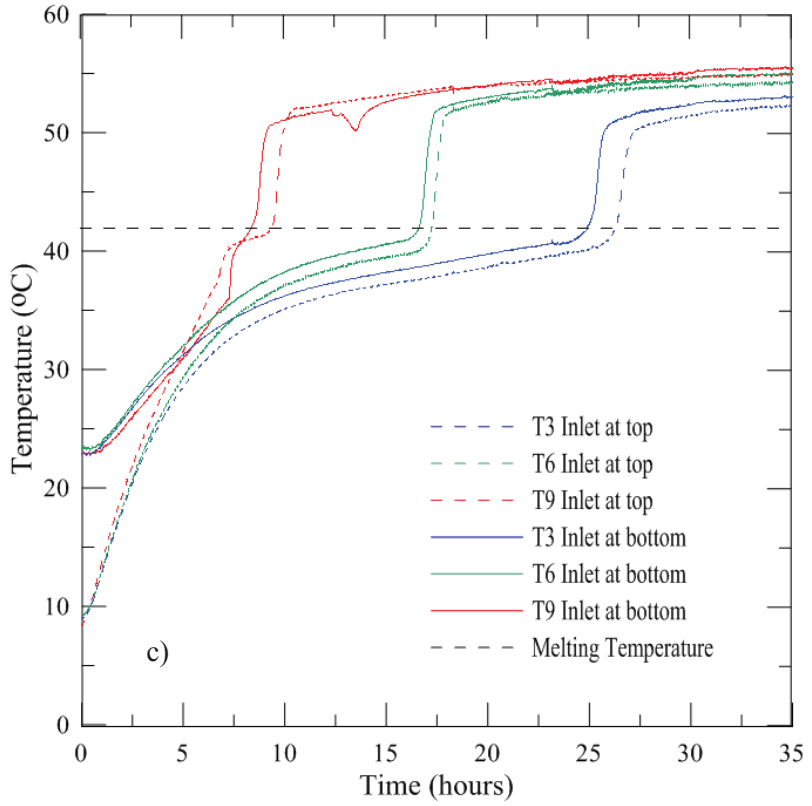


**Figure 5.14: Temperature profiles as a function of time measured during charging: b) Hot-side probes T2, T5 and T8 c) Cold-side probes T3, T6 and T9 (comparing inlet orientation), continued**

The results presented in Fig. 5.14 indicate that having the inlet of the hot water at the bottom of the LHESS only slightly decreases the melting time of the PCM, as recorded by the thermocouple probes. Although the system with the inlet at the bottom melted slightly faster, the lag time at the probe locations only ranges up to one hour, which is small compared to the total time required to charge the system. However, with the inlet at the bottom, after 72 hours of charging the melting interface on the cold side of the LHESS remained 5 cm (2 in) from the bottom of the cylinder, and not all of the PCM had melted, as shown in Figure 5.15.

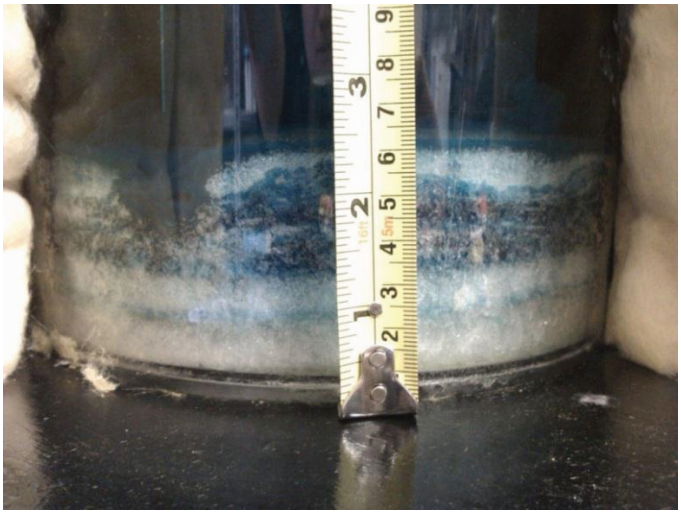

**Figure 5.15: Photograph taken after 72 hours of charging**

Ettouney et al. concluded that the large temperature difference between the inlet and outlet of the HTF, for the case of the HTF entering from the top, was the reason that the PCM at the top of the container remained hotter than the bottom of the container (Ettouney et al., 2004). However, based on the comparison between the two inlet orientations reported in this thesis, the increased melting at the top of the LHESS for this experimental setup was not driven by the temperature difference between the inlet and outlet of the HTF. This verifies the results found in Section 5.4, and proves that the temperature variations over the height of the LHESS are a result of natural convection, and not a result of the hot HTF inlet location.

### *5.5 Complete Discharging*

Complete discharging of the LHESS was performed to study the heat transfer patterns throughout the system and to compare the energy recovered by the cold HTF to the energy input during charging. The experimental parameters used are given in Table 5.1.

Figure 5.16 below shows the temperatures at the two thermocouple probe depths during discharging.

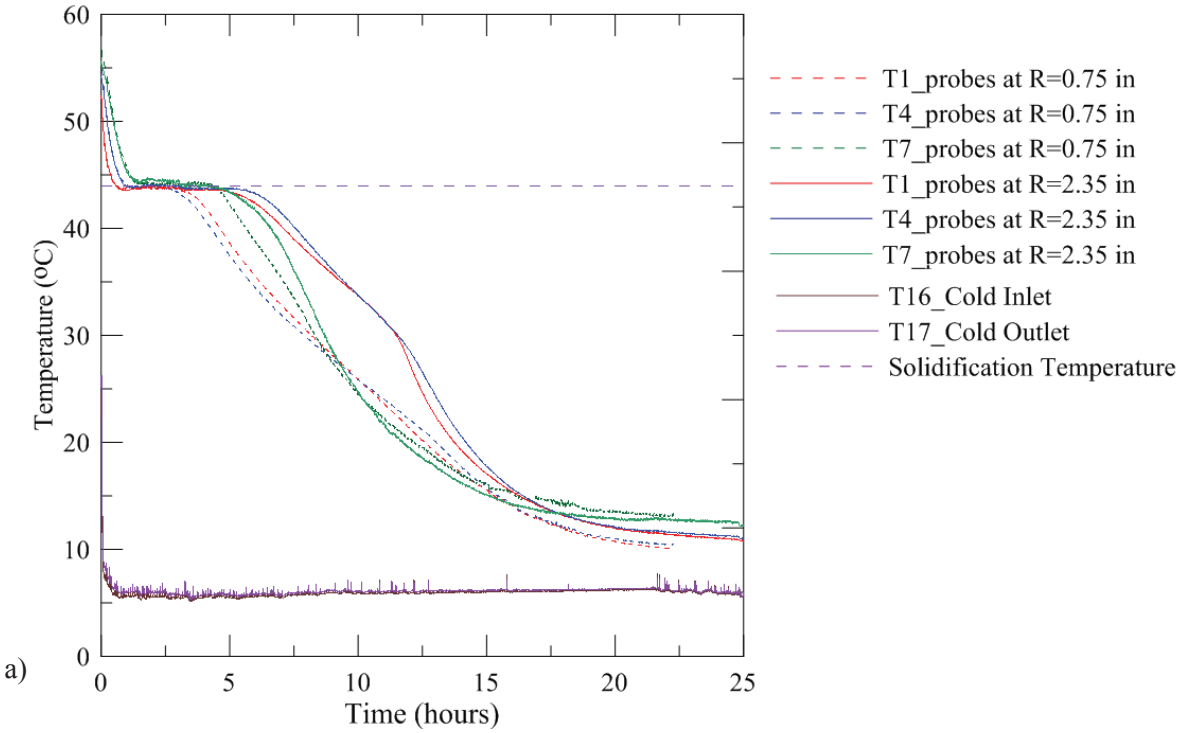


**Figure 5.16: Temperature profiles as a function of time measured during discharging: a) Middle probes T1, T4 and T7 (3.5 L/min flow rate)**

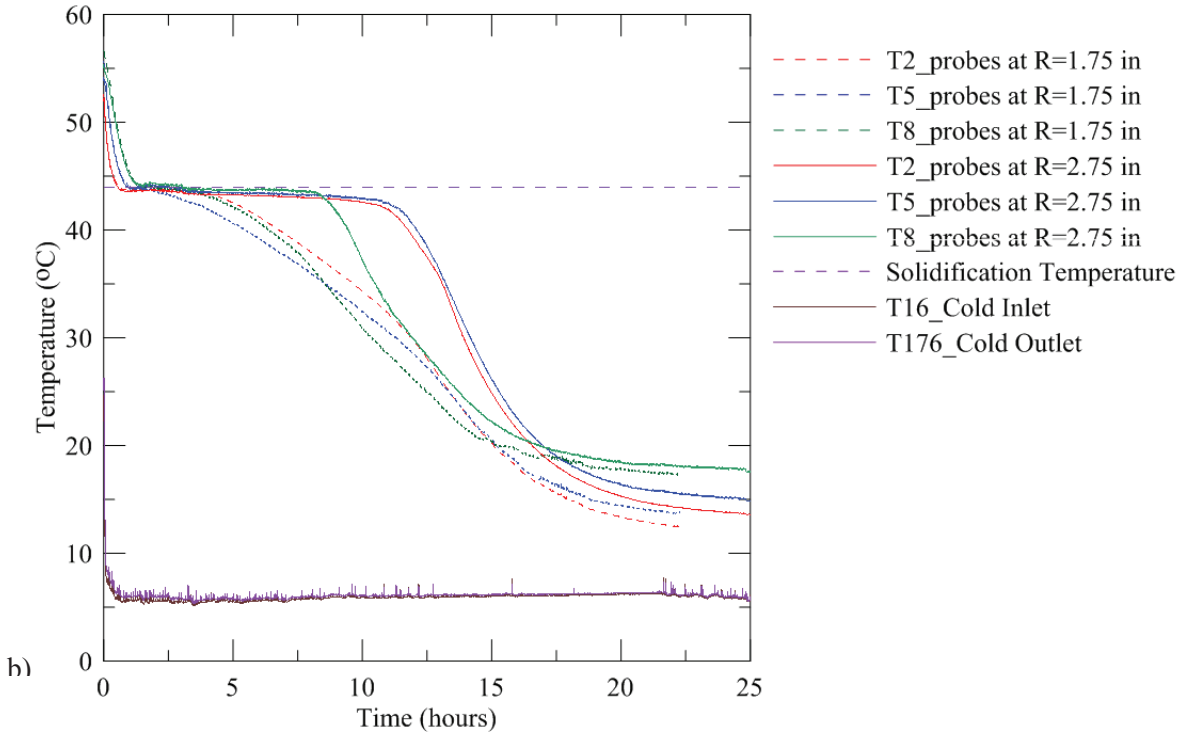


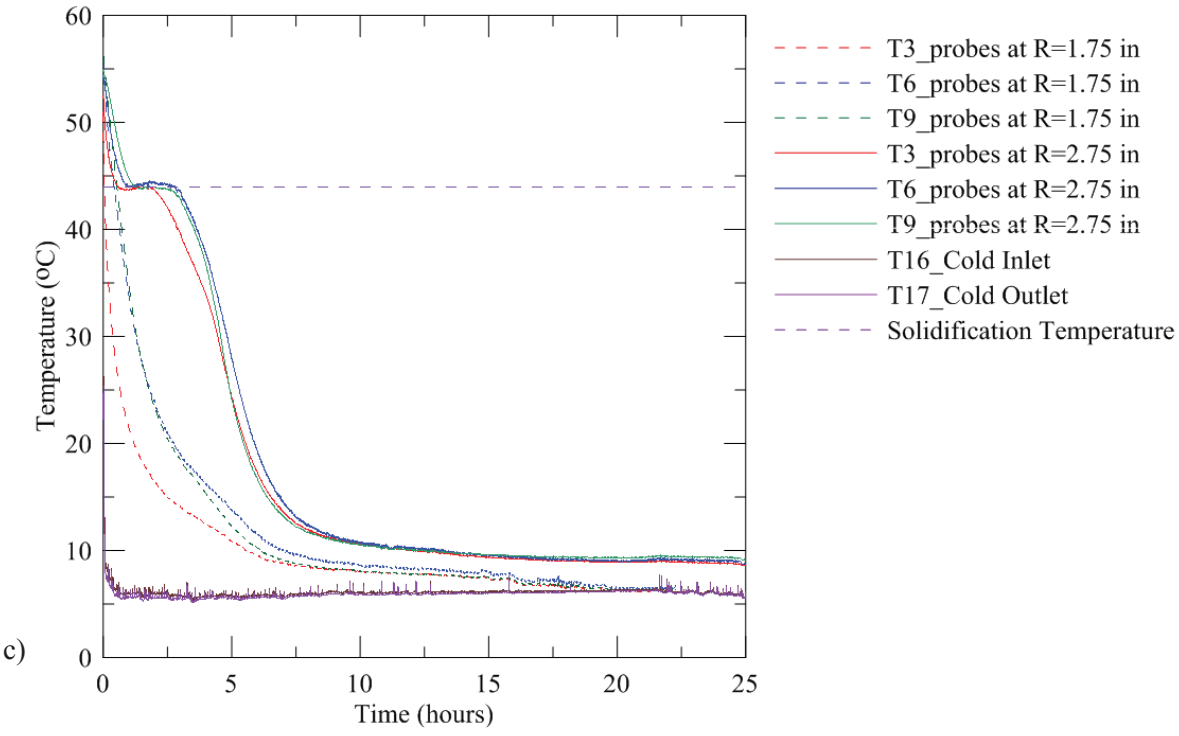


**Figure 5.16: Temperature profiles as a function of time measured during discharging: b) Hot-side probes T2, T5 and T8 c) Cold-side probes T3, T6 and T9 (3.5 L/min flow rate), continued**

From Fig. 5.16 it is apparent that natural convection does not play a significant role during solidification, since the temperature profiles of the PCM are independent of the height of the thermocouple probe. It took about 40 hours for all of the PCM to solidify. The PCM solidified around the inside wall of the container as well as close to the cold HTF pipe, making it impossible to accurately observe when the inside layers of the PCM were completely solid.

The temperatures recorded at the two probe depths in Fig. 5.16 (dashed lines representing the PCM closer to the cold HTF, and solid lines representing the PCM farther away from the cold HTF) indicated that solidification proceeded from the cold pipe surface to the container wall. The PCM first solidifies around the cold HTF pipe, thereby insulating the pipe and slowing down the solidification process in the rest of the LHESS. This is observed in Fig. 5.16-a) by the faster initial decrease in temperature (before the PCM solidified) compared to the slower decrease in temperature after the PCM solidified. This is also due to the decreased heat transfer rate as a result of a smaller temperature difference between the cold HTF and the PCM as discharging proceeds.

Based on the temperature profiles given in Fig. 5.16, the solidification plateau appears to be at 44 $^{o}$C, which is a slightly higher temperature than the expected solidification temperature. The actual solidification temperature of a PCM is always lower than its melting temperature because of a minimum level of sub-cooling required for nucleation (activation energy). The measured solidification temperature plateau given by this experimental setup is higher due to the interference of the thermocouple probes, which gives the PCM a nucleation site. The same phenomenon was recorded by Agyenim and Hewitt in a horizontally mounted concentric shell and tube LHESS (Agyenim & Hewitt, 2010).

### *Energy Recovered*

Initially an average of 10,500 kJ ± 35 % was recovered. This is the average energy recovered for three discharging experiments at varying flow rates, and is unreasonably large since only an

average of 5390 kJ ± 49 % was stored in the PCM. Because the constant temperature hot water bath was still connected to the LHESS by the copper pipe, the cold water was recovering energy from the PCM as well as from the hot water bath. 28.3 kg of water in the hot water bath, initially at 60 $^{o}$C, was being cooled to room temperature by both losing heat through the water bath and pipe walls, and by transferring energy to the cold HTF. This led to 4300 kJ ± 4 % of sensible energy lost from the hot water bath. The bath and pipe were insulated; therefore it is assumed that the majority of this energy was recovered by the cold HTF. Once this problem was identified, the hot water bath was detached during discharging, and 4760 kJ ± 45 % of energy was recovered by the cold HTF. This means there is a 12 % difference in the energy recovered by the cold HTF and energy supplied by the hot HTF, which, given the uncertainty in the energy calculations, is acceptable. Figure 5.17 shows the energy input and recovered over one cycle of charging and discharging.

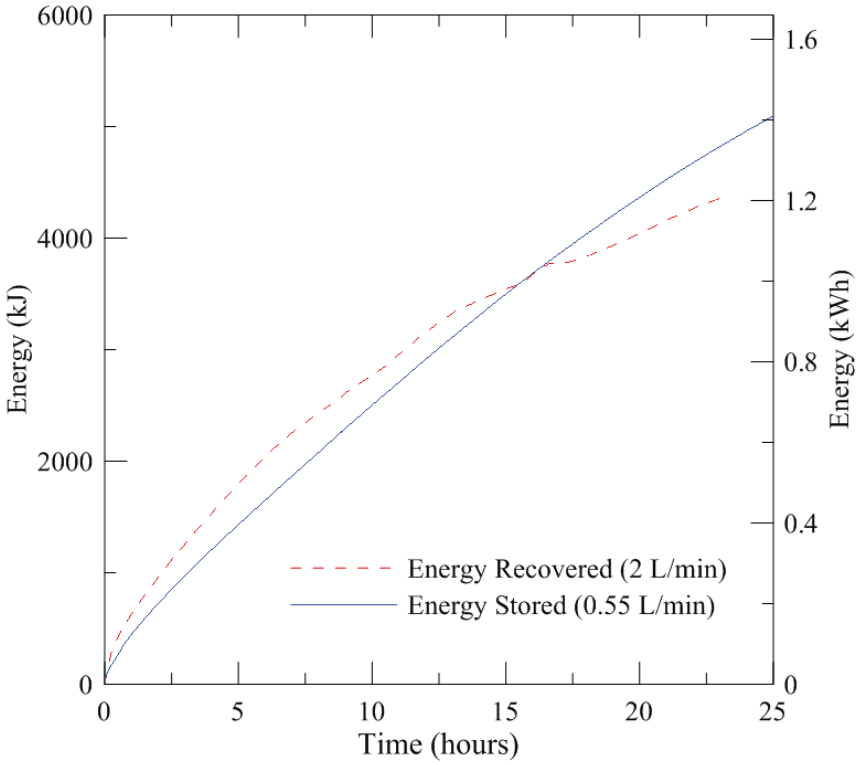


**Figure 5.17: Energy stored and recovered as a function of time during charging and discharging experiments**

The energy recovered matched closely to the energy input, even though the flow rate of charging and discharging are not the same, which in this case is a coincidence.

### 5.5.1 Effect of Flow Rate on Discharging

The LHESS was discharged using various flow rates to determine if the cold HTF flow rate affects the solidification patterns inside the system. Figure 5.18 shows the temperature profiles at the probe locations for three different flow rates.

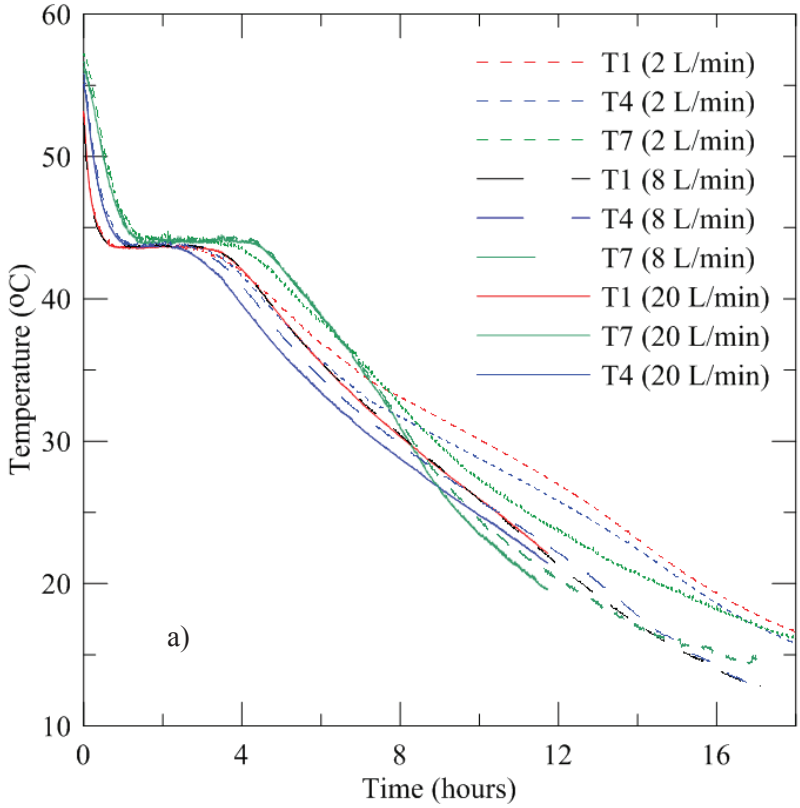


**Figure 5.18: Temperature profiles as a function of time measured during discharging: a) Middle probes T1, T4 and T7 (comparing flow rate)**

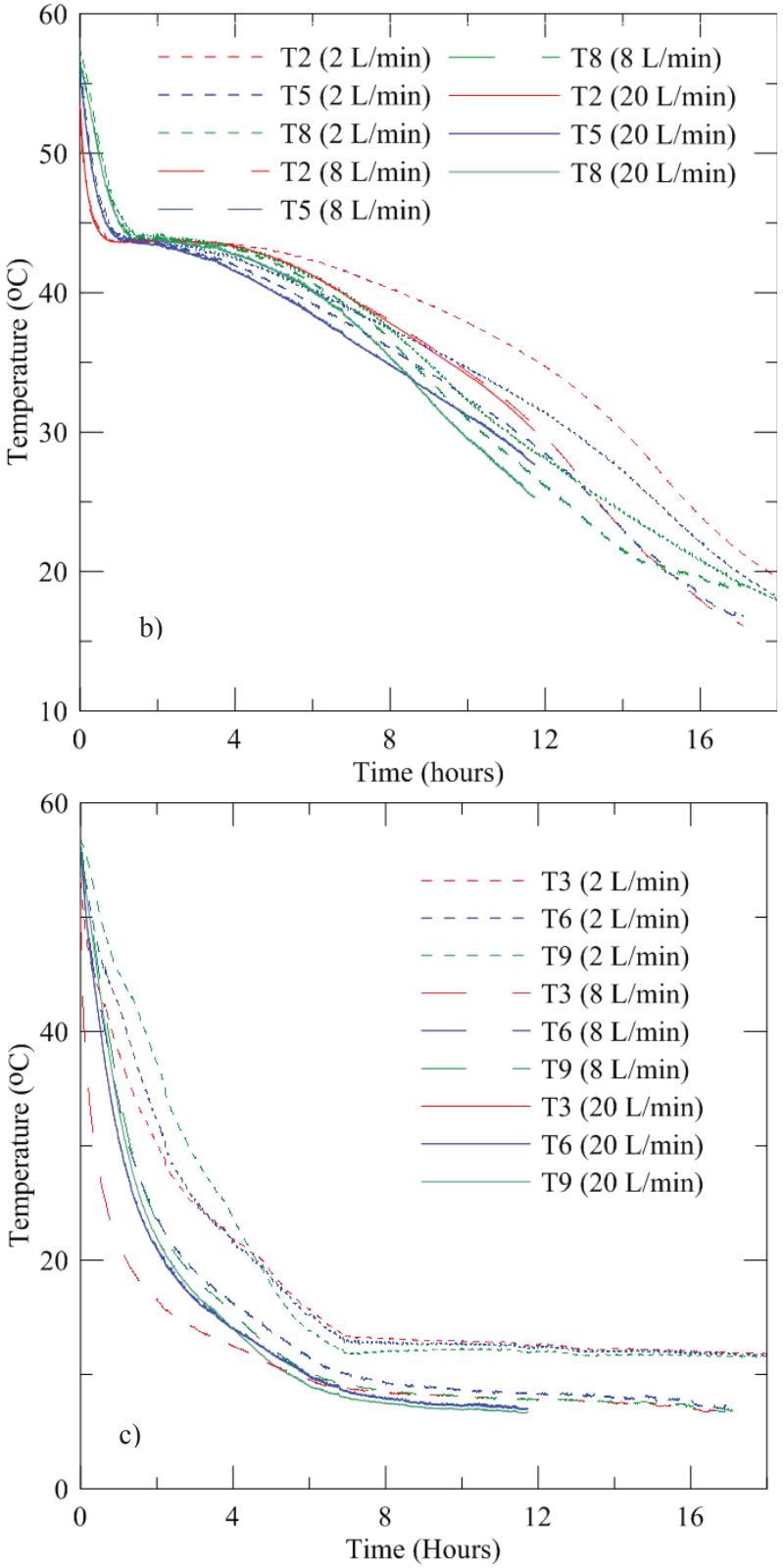


**Figure 5.18: Temperature profiles as a function of time measured during discharging: b) Hot-side probes T2, T5 and T8 c) Cold-side probes T3, T6 and T9 (comparing flow rate), continued**

The flow rate does not significantly change the solidification patterns of the PCM. The discharging experiments had similar phase change patterns and cooling rates independent of the cold HTF flow rates used. Figure 5.18-a) shows that the phase transition plateaus are the same for all the flow rates used, with the PCM at the top of the container (T7) taking slightly longer to solidify on the side of the cold HTF. The PCM in Fig. 5.18-c) solidified so fast, due to the proximity of the PCM to the cooling source, that the phase transition plateaus are not observed. For the lower flow rate, the PCM initially cools down more slowly, as shown by the small dashed lines in Fig. 5.18-c). This is because the PCM is initially melted when discharging begins; therefore, the amount of natural convection in the PCM can vary to accommodate the variation in the heat transfer rate as the flow rate changes, as discussed in Section 5.4.2. Although the convection coefficient increases inside the pipe with increased flow rate, as shown in Section 4.3, once the PCM solidifies there is no increase in the rate of cooling because there is no natural convection in the solid PCM. Therefore, the increased forced convection does not impact the rate of solidification like it does the rate of melting. This agrees with the results presented for charging, in Section 5.4.2, where it was found that varying the flow rate only affected the rate of heat transfer once the PCM was melted.

The temperature difference between the inlet and outlet of the cold HTF with respect to the flow rate over the discharging period is shown in Fig. 5.19.

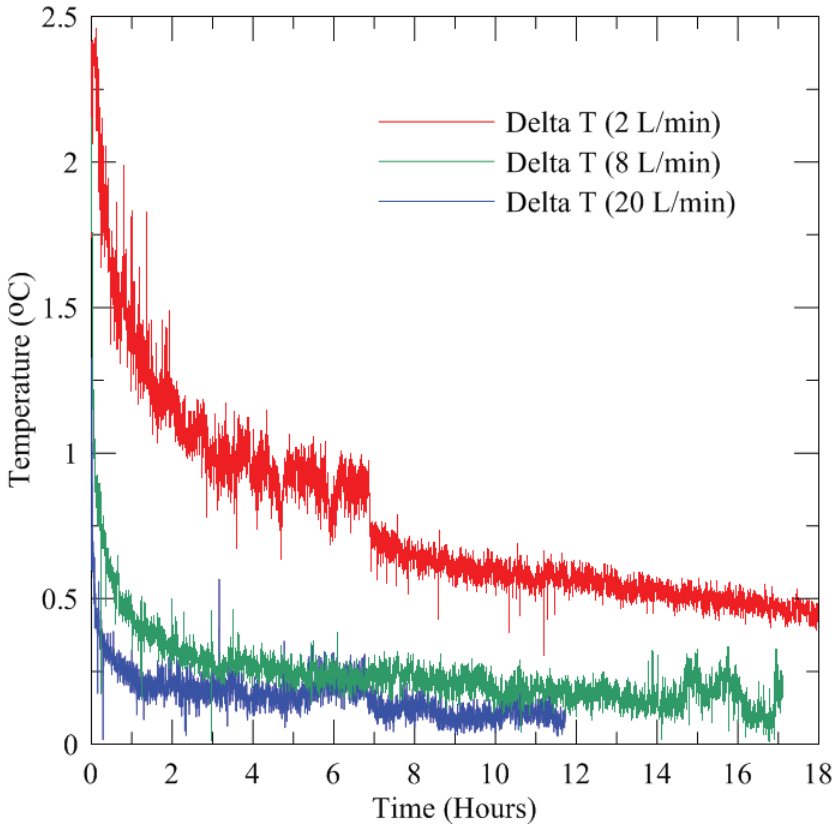


**Figure 5.19: Temperature difference between inlet and outlet of cold HTF (comparing flow rates)**

As the flow rate increases, the temperature difference between the inlet and outlet of the cold HTF decreases. This is because the amount of energy recovered from the PCM does not vary with the flow rate in these discharging experiments. In order for the amount of energy recovered from the system, based on Eq. (4.1), to remain constant for the different flow rates, the temperature difference between the inlet/outlet of the cold HTF decreases to compensate for the increased flow rate, as shown in Fig. 5.19. At the 2 L/min cold HTF flow rate, after seven hours of charging, there is an abrupt decrease in the temperature difference which is because of a sudden increase in the municipal water temperature.

### 5.5.2 Effect of Insulation Thickness on Discharging

A charging and discharging experiment was run with a 0.635 cm (¼ in) thick layer of insulation around the LHESS. For the experiments discussed in this thesis a 1.9 cm (¾ in) thick layer of

insulation was used. The heat losses through the container wall, as discussed in Section 5.4, were calculated for this thicker insulation. For charging, thicker insulation is beneficial because it results in reduced heat losses through the container wall and faster charging of the LHESS. However, adding insulation to the container actually increased the time required for the PCM to solidify, as seen in Fig. 5.20.

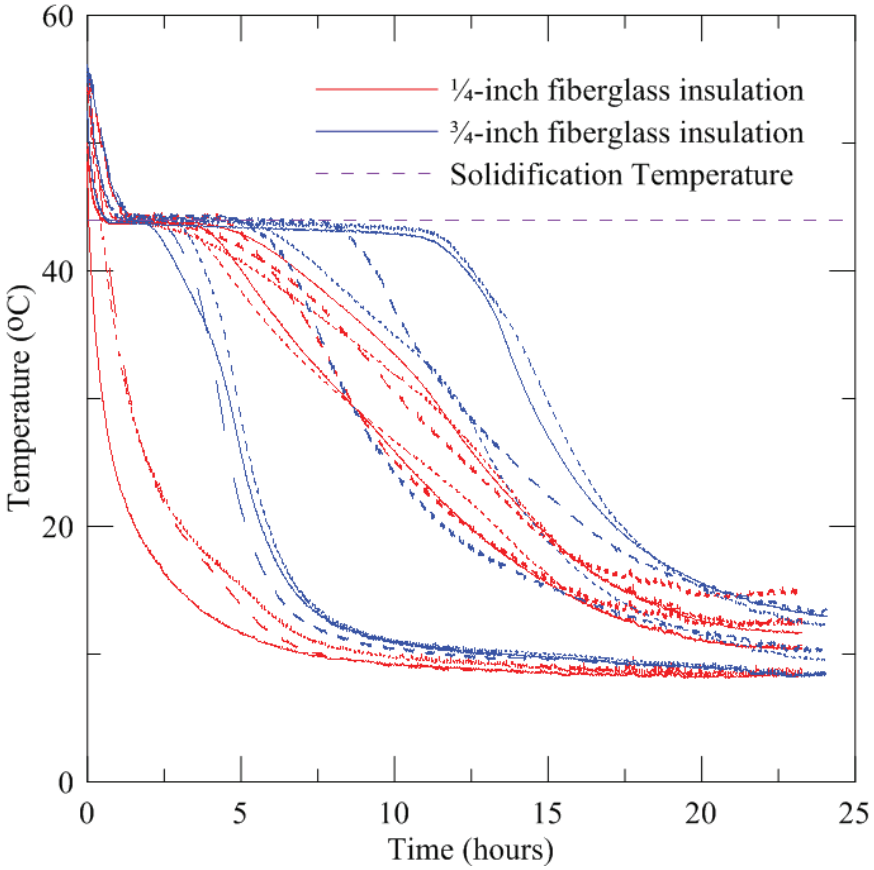


**Figure 5.20: Temperature profiles as a function of time measured during discharging for various insulation thicknesses (3.5 L/min cold HTF flow rate)**

The thicker layer of insulation resulted in a reduction in the heat losses through the container wall and therefore increased the time required for the PCM to solidify. This increased solidification time is indicated by the longer solidification plateaus seen for the 1.9 cm (¾ in) insulation thickness (blue lines). With less insulation the PCM solidifies faster, however this does not mean

the cold HTF recovers more energy from the system, but that additional energy is lost to the surroundings.

### *5.6 Summary*

In Chapter 5 it was found that during charging convection is the main mechanism of heat transfer once the PCM is melted. However, when the PCM is solid before melting, and during discharging, conduction is the only mechanism of heat transfer present in the system. During discharging, the PCM solidifies close to the cold HTF pipe and insulates the remaining PCM. During charging, the PCM melts from close to the heat source outward, resulting in faster melting compared to solidification. The different mechanisms of heat transfer present during charging and discharging cause the PCM to react differently to an increase in HTF flow rate. During charging, increasing the hot HTF flow rate speeds up melting by the increasing natural convection in the melted PCM. However, during solidification, increasing the cold HTF flow rate does not affect the rate of solidification because the solid PCM is limited to conductive cooling.

# Chapter 6 Results and Discussion: Simultaneous Charging and Discharging

The LHESS was charged and discharged simultaneously, helping to fill the gap in LHESS research which was identified in Chapter 2. In this chapter, all thermocouple probe measurements were taken at the second probe depth, as given by Fig. 5.3-b).

## *6.1 List of Experiments Performed*

The experiments performed and their location in the thesis, are outlined in the Table 6.1.

**Table 6.1: List of experiments performed**

| Experiment Number | Simultaneous Charging and Discharging Experiments | Location in Thesis |
|---|---|---|
| 1 | Initially melted, simultaneous charging/discharging at same flow rate (2.75 L/min for both charging/discharging) for 24 hours | Section 6.2 |
| 2 | Initially solid, simultaneous charging/discharging at same flow rate (2.75 L/min for both charging/discharging) for 24 hours | Section 6.2 |
| 3 | Initially melted, simultaneous charging/discharging at same flow rate (10 L/min for both charging/discharging) for 24 hours | Section 6.2 |
| 4 | Initially solid, simultaneous charging/discharging at same flow rate (10 L/min for both charging/discharging) for 24 hours | Section 6.2 |
| 5 | Initially melted, 10 minutes simultaneous charging/discharging then 10 minutes charging (5.7 L/min discharging flow rate and 2.75 L/min charging flow rate) | Section 6.3 |
| 6 | Initially melted, 10 minutes simultaneous charging/discharging then 20 minutes charging (5.7 L/min discharging flow rate and 2.75 L/min charging flow rate) | Appendix D |
| 7 | Initially melted, 10 minutes simultaneous charging/discharging then 30 minutes charging (5.7 L/min discharging flow rate and 2.75 L/min charging flow rate) | Appendix D |
| 8 | Initially melted, 20 minutes simultaneous charging/discharging then 20 minutes charging (5.7 L/min discharging flow rate and 2.75 L/min charging flow rate) | Appendix D |
| 9 | Initially melted, 20 minutes simultaneous charging/discharging then 40 minutes charging (5.7 L/min discharging flow rate and 2.75 L/min charging flow rate) | Appendix D |
| 10 | Initially melted, 10 minutes simultaneous charging/discharging then 10 minutes charging (20 L/min discharging flow rate and 2.75 L/min charging flow rate) | Section 6.3 |
| 11 | Initially melted, 10 minutes simultaneous charging/discharging then 20 minutes charging (20 L/min discharging flow rate and 2.75 L/min charging flow rate) | Appendix D |
| 12 | Initially melted, 10 minutes simultaneous charging/discharging then 30 minutes charging (20 L/min discharging flow rate and 2.75 L/min charging flow rate) | Appendix D |
| 13 | Initially melted, 20 minutes simultaneous charging/discharging then 20 minutes charging (20 L/min discharging flow rate and 2.75 L/min charging flow rate) | Appendix D |

| | | |
|---|---|---|
| 14 | Initially melted, 20 minutes simultaneous charging/discharging then 40 minutes charging (20 L/min discharging flow rate and 2.75 L/min charging flow rate) | Appendix D |
| 15 | Initially solid, 10 minutes simultaneous charging/discharging then 10 minutes charging (5.7 L/min discharging flow rate and 2.75 L/min charging flow rate) | Section 6.3 |
| 16 | Initially solid, 10 minutes simultaneous charging/discharging then 20 minutes charging (5.7 L/min discharging flow rate and 2.75 L/min charging flow rate) | Appendix D |
| 17 | Initially solid, 10 minutes simultaneous charging/discharging then 30 minutes charging (5.7 L/min discharging flow rate and 2.75 L/min charging flow rate) | Appendix D |
| 18 | Initially solid, 20 minutes simultaneous charging/discharging then 20 minutes charging (5.7 L/min discharging flow rate and 2.75 L/min charging flow rate) | Appendix D |
| 19 | Initially solid, 20 minutes simultaneous charging/discharging then 40 minutes charging (5.7 L/min discharging flow rate and 2.75 L/min charging flow rate) | Appendix D |
| 20 | Initially solid, 10 minutes simultaneous charging/discharging then 10 minutes charging (20 L/min discharging flow rate and 2.75 L/min charging flow rate) | Section 6.3 |
| 21 | Initially solid, 10 minutes simultaneous charging/discharging then 20 minutes charging (20 L/min discharging flow rate and 2.75 L/min charging flow rate) | Appendix D |
| 22 | Initially solid, 10 minutes simultaneous charging/discharging then 30 minutes charging (20 L/min discharging flow rate and 2.75 L/min charging flow rate) | Appendix D |
| 23 | Initially solid, 20 minutes simultaneous charging/discharging then 20 minutes charging (20 L/min discharging flow rate and 2.75 L/min charging flow rate) | Appendix D |
| 24 | Initially solid, 20 minutes simultaneous charging/discharging then 40 minutes charging (20 L/min discharging flow rate and 2.75 L/min charging flow rate) | Appendix D |

The experimental parameters used in each case are given in the subsequent sections. However, the hot and cold HTF inlet temperatures are 58 ± 0.5˚C and 10 ± 0.5˚C, respectively, for all the experiments done in this thesis. The corresponding Stefan numbers for the experiments in Chapter 6 are 0.17 ± 3 % for melting and 0.43 ± 1 % for solidification.

Two initial conditions were used throughout Chapter 6 to study the impact that the PCM phase has on the heat transfer processes during simultaneous charging/discharging. These initial conditions are:

1) PCM completely melted
2) PCM completely solid

Initial condition 1) represents a LHESS which has been fully charged prior to simultaneous charging/discharging. Initial condition 2) represents a LHESS that has not had energy supplied to melt the PCM, or was previously fully discharged, so the PCM is solid at room temperature.

### *6.2 Simultaneous Charging and Discharging with the same Flow Rates*

As discussed in Chapter 1, a LHESS used with a SDHW system operates under simultaneous charging/discharging modes due to the time intervals of the hot water demand and solar energy availability. The same flow rates are used for the hot and cold HTF to allow a direct comparison between energy recovered and energy supplied. The uncertainty in the energy calculations for some of the experiments in Chapter 6 are large, therefore the energy calculations are for trend identification only. The experimental parameters used for Section 6.2 are given in Table 6.2.

**Table 6.2: Experimental Parameters for Section 6.2**

| | |
|---|---|
| Hot HTF Temperature | 58 ± 0.5˚C |
| Cold HTF Temperature | 10 ± 0.5˚C |
| Hot HTF Flow Rates | 2.75 and 10 L/min |
| Cold HTF Flow Rates | 2.75 and 10 L/min |

These simultaneous charging/discharging experiments were performed for a 24 hour period to study the behavior of the PCM during this operating mode. The 24 hour period was determined experimentally, and was chosen to insure that all significant changes in the system in this operating mode were captured by the thermocouples.

### 6.2.1 Initially Melted Phase Change Material

The LHESS was charged and discharged simultaneously twice, each time using the same flow rates for the hot and the cold HTF (2.75 L/min for the first experiment and 10 L/min for the second experiment). In these experiments the PCM was initially melted. Figure 6.1 shows the temperatures recorded by the probe thermocouples as a function of time for the two experiments.

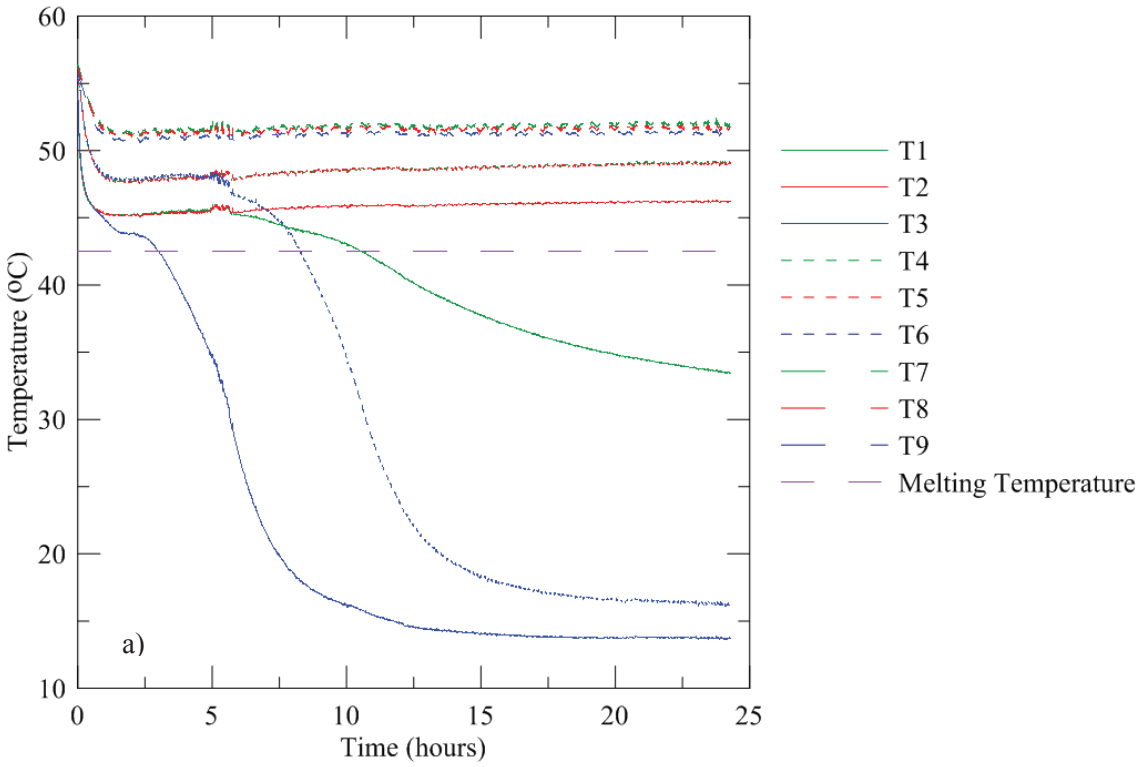


**Figure 6.1: Temperature profiles as a function of time measured during simultaneous charging/discharging of initially melted PCM for a flow rate of a) 2.75 L/min**

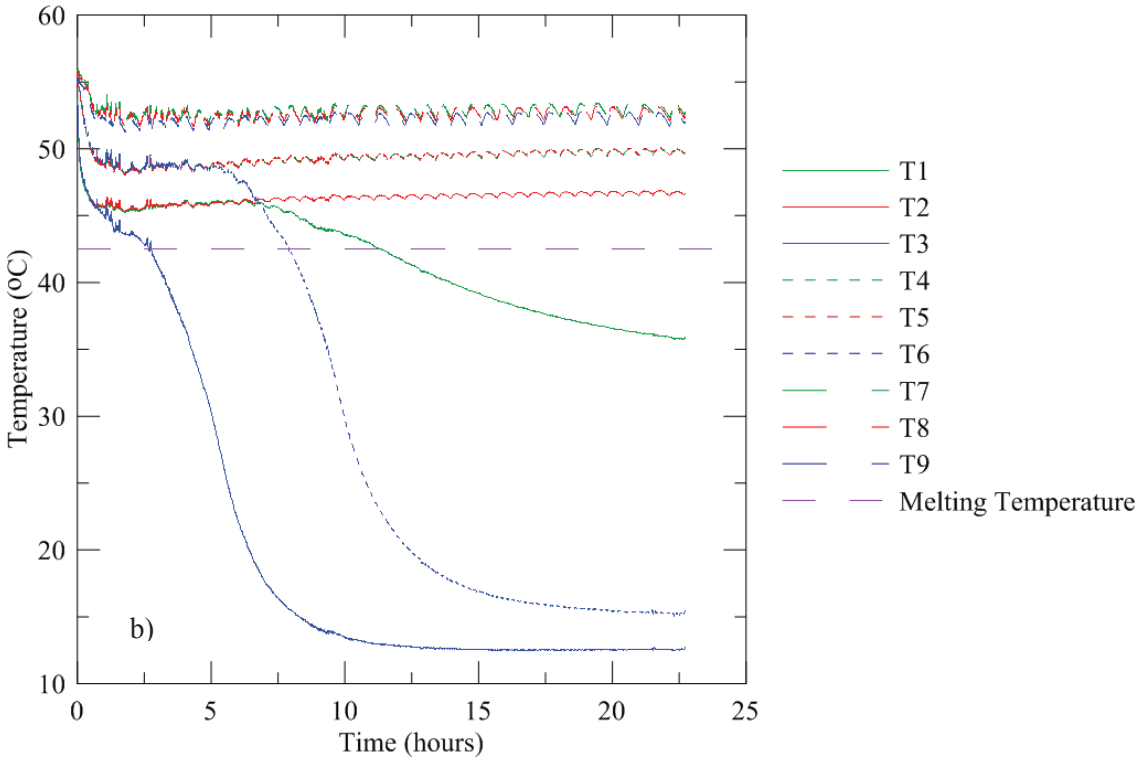


**Figure 6.1: Temperature profiles as a function of time measured during simultaneous charging/discharging of initially melted PCM for a flow rate of b) 10 L/min, continued**

From Fig. 6.1, the flow rate does not affect the PCM behavior in this operating mode, as there is no significant difference between the temperature profiles shown in Figures 6.1-a) and b). In both experiments shown in Fig. 6.1, the bottom two-thirds of the PCM on the side of the cold HTF (T3 and T6- blue lines), and the bottom one-third of the PCM in the middle of the LHESS (T1- solid green lines) solidified. The PCM on the side of the hot HTF remained completely melted, although the temperature of the PCM at the bottom (T2- solid red lines) initially decreased and remained 8 $^{o}$C cooler than the PCM at the top of the container (T8 –red large dashed lines). This is a result of natural convection in the melted PCM displacing energy upward to keep the PCM hotter at the top of the LHESS.

All of the thermocouple probes recorded temperature drops within the first 2 hours. This is a result of an initial thermal shock in the system when warm stagnant water in the cold pipe (which was heated when the system was initially charged to bring the PCM to the melted initial

condition) was quickly replaced by the cold HTF when the experiment began. The PCM reacted to this thermal shock by decreasing in temperature by 2 to 4 ºC everywhere, with the largest temperature drops at the bottom of the LHESS (T1, T2 and T3).

The PCM temperatures near the top of the container (T7, T8 and T9), even on the side of the cold HTF, remained above the melting temperature. Again, this is attributed to natural convection bringing higher temperature PCM from elsewhere in the system to the top of the container. With natural convection keeping hotter melted PCM at the top of the container, stratification is observed in the LHESS. The temperatures measured by the adhesive thermocouples on the fins of the hot and cold HTF pipes are given in Fig. 6.2.

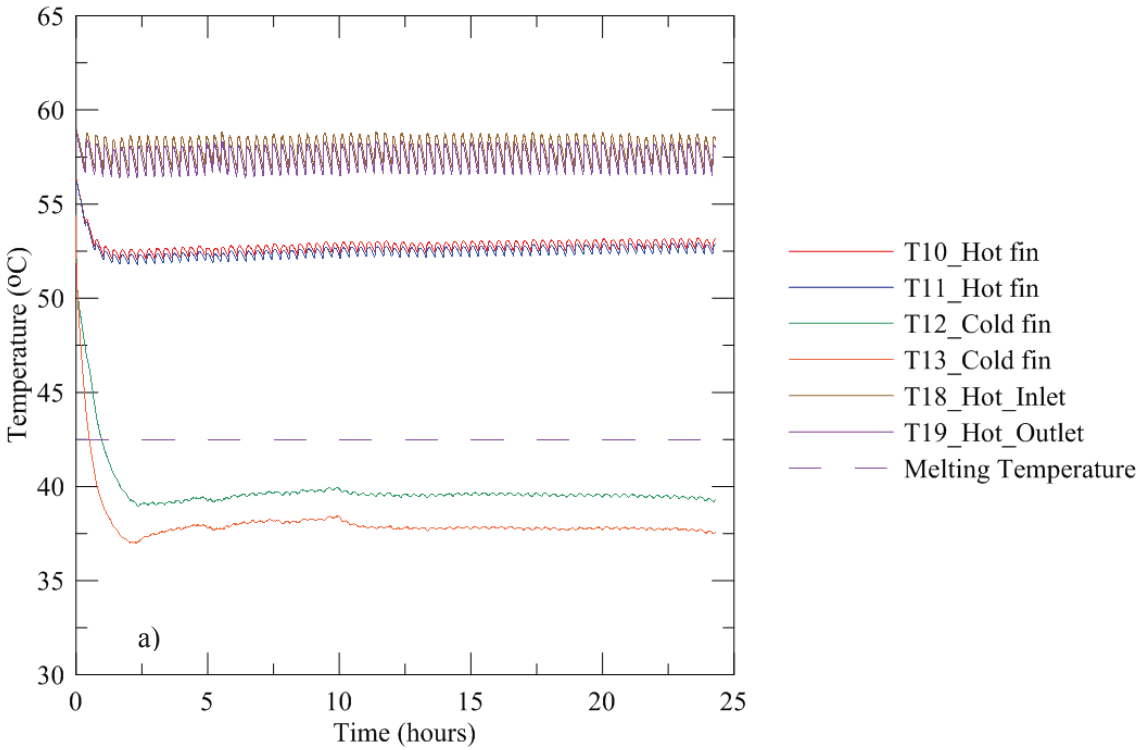


**Figure 6.2: Temperature profiles as a function of time measured by thermocouples on fins during simultaneous charging/discharging for a flow rate of a) 2.75 L/min**

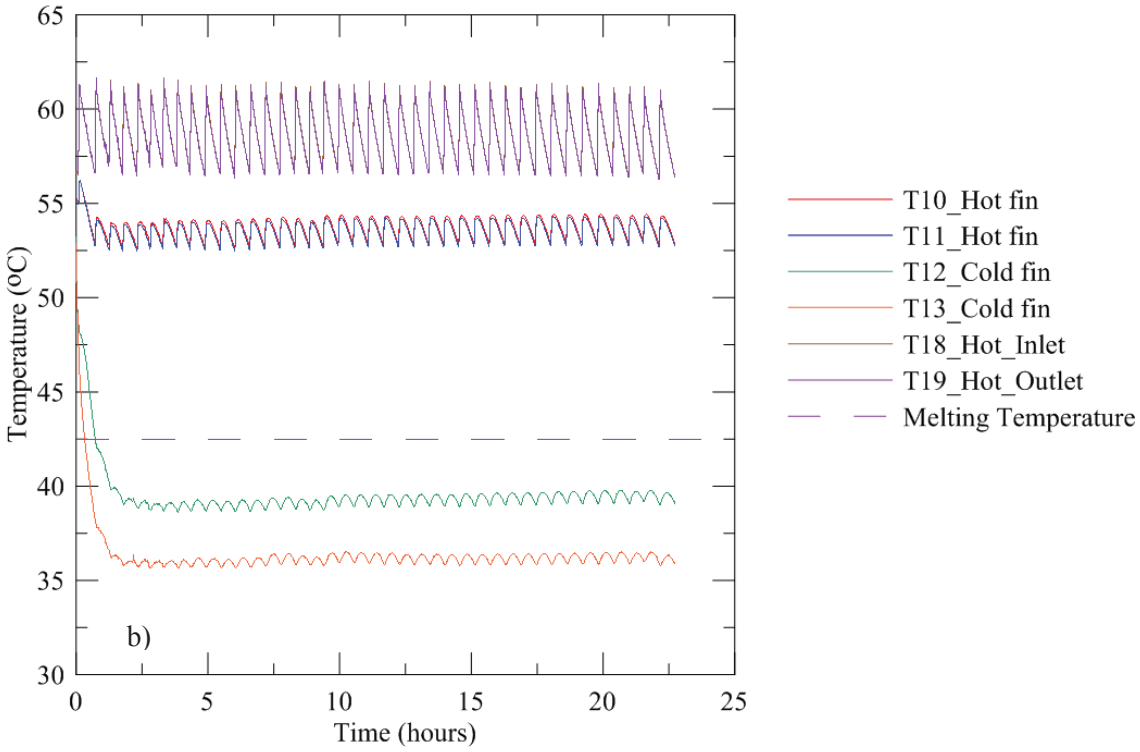


**Figure 6.2: Temperature profiles as a function of time measured by thermocouples on fins during simultaneous charging/discharging for a flow rate of b) 10 L/min, continued**

For both flow rates, the PCM close to the fins on the hot HTF pipe (T10 and T11) remained melted, and the PCM close to the fins on the cold HTF pipe (T12 and T13) solidified. Temperature fluctuations are present in the PCM near the fins on the hot HTF pipe, and are larger for the 10 L/min case [Fig. 6.2-b)] than the 2.75 L/min case [Fig. 6.2-a)]. These fluctuations are similar to the fluctuations in the hot HTF temperatures (T18 and T19), which are also more apparent for the higher HTF flow rate. The hot HTF and hot fin temperatures fluctuate more for the 10 L/min experiment than the 2.75 L/min experiment because the immersion heater has to provide more energy to maintain the hot HTF at a relatively constant temperature. The immersion heater therefore stays on for longer periods of time, resulting in a larger increase in the inlet temperature of the hot HTF.

The photograph in Fig. 6.3 shows the solid PCM on the side of the cold HTF pipe (right side of the photograph) and the still melted PCM on the side of the hot HTF pipe (left side) at the end of the 24 hour simultaneous charging/discharging experiment.

**Figure 6.3: Photograph of LHESS after 24 hours of simultaneous charging/discharging at 2.75 L/min**

The PCM solidified on the fins of the cold HTF pipe within the first hour of the experiment, as seen in Fig. 6.2 (T12 and T13), and then solidification proceeded toward the container wall. This can be seen in Fig. 6.3. As well, the PCM between the hot and cold HTF pipes remained melted.

### 6.2.2 Initially Solid Phase Change Material

Similarly to Section 6.2.1, the LHESS was charged and discharged simultaneously twice, each time using the same flow rates for the hot and the cold HTF (2.75 L/min for the first experiment and 10 L/min for the second experiment). In this case the PCM was initially solid. Figure 6.4 shows the temperatures recorded throughout the container.

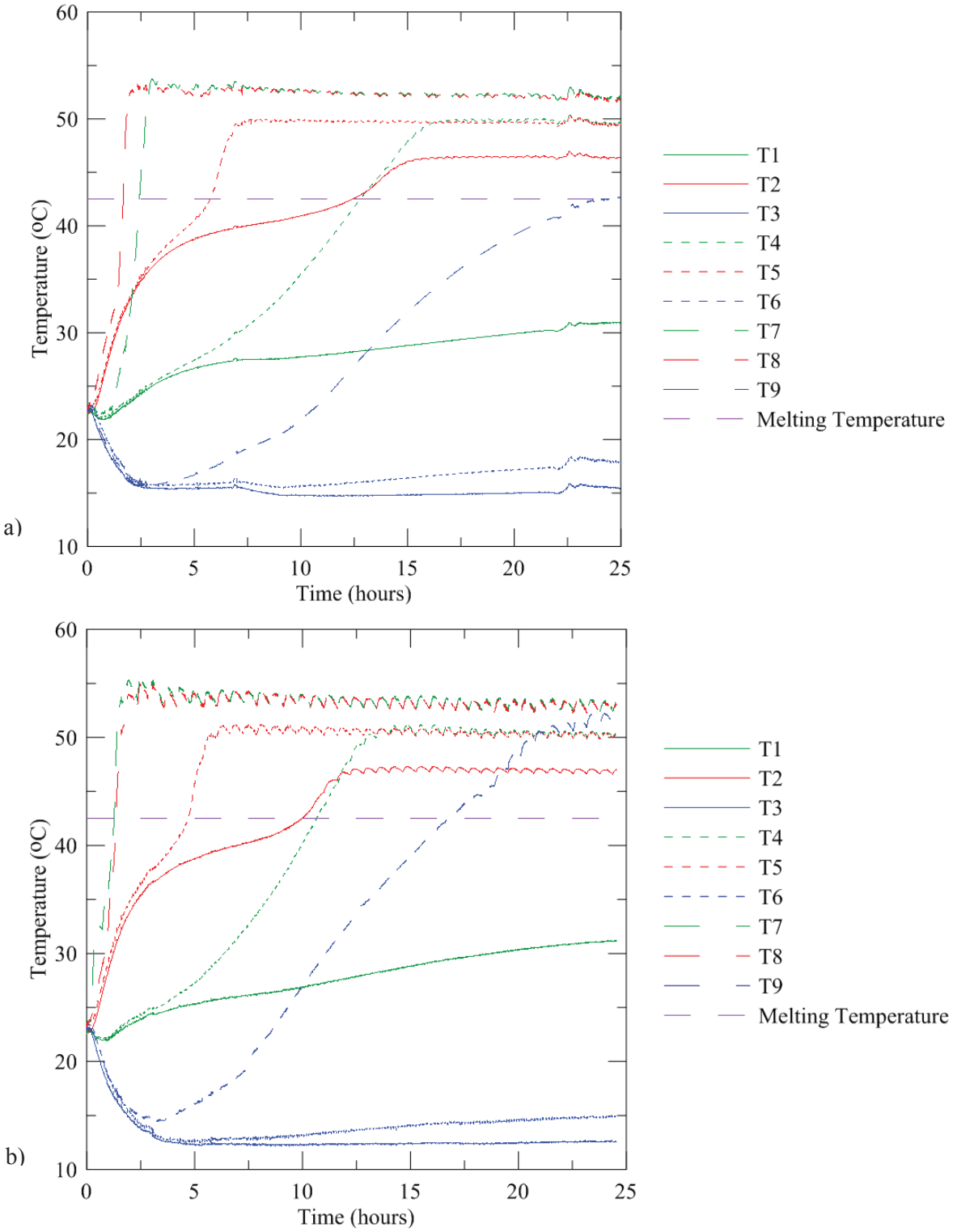


**Figure 6.4: Temperature profiles as a function of time measured during simultaneous charging/discharging of initially solid PCM for a flow rate of a) 2.75 L/min b) 10 L/min**

Similarly to Section 6.2.1, the flow rate does not have a significant effect on the heat transfer processes inside the container, as there is no significant difference between the temperature profiles in Figures 6.4-a) and b). For both flow rates all of the PCM on the side of the hot HTF pipe melted (T2, T5 and T8- red lines). All of the PCM at the top height of the container melted as well, with the PCM on the side of the cold HTF pipe at the top height being last to melt (T9- blue large dashed line). The bottom two-thirds of the PCM on the side of the cold HTF pipe remained solid, which indicates that the top third which melted was heated by warmer PCM that was carried up by natural convection. Otherwise, the top third of the PCM on the side of the cold HTF pipe would have remained solid because of the PCMs proximity to the cold HTF. The top two-thirds of the PCM in the middle probe location between the hot and cold HTF pipes (T4 and T7- green lines) melted as well. Figure 6.5 shows the initially melted case [6.5-a)] compared to the initially solid case [6.5-b)] for the low flow rate.

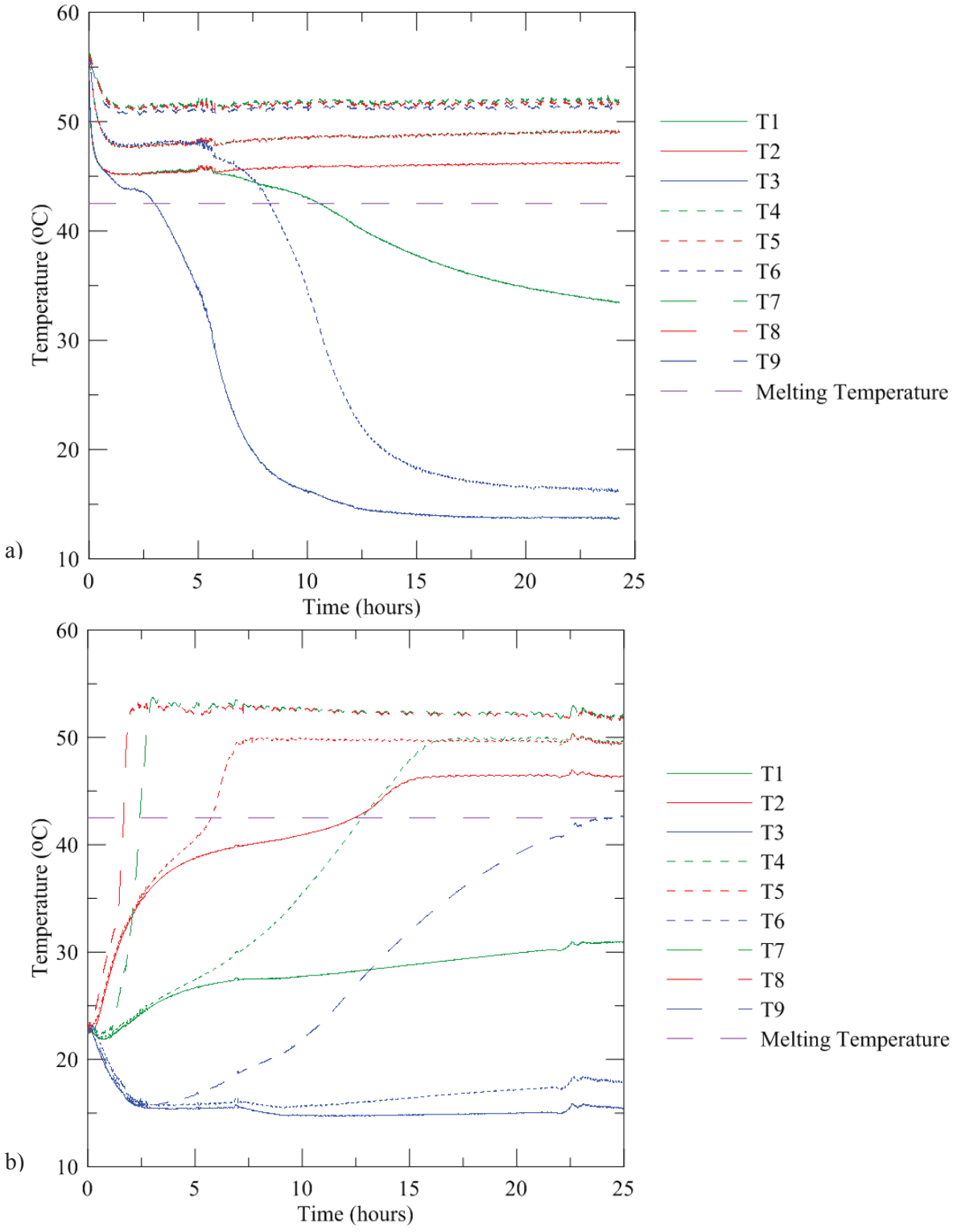


**Figure 6.5: Temperature profiles as a function of time measured during simultaneous charging/discharging at 2.75 L/min: a) initially melted b) initially solid**

Figure 6.5 indicates that the PCM completely melts, or remains melted, on the side of the hot HTF pipe (red lines in Fig. 6.5) for both initial conditions. As well, the middle thermocouple probes recorded melting in the top two-thirds of the container (green lines in Fig. 6.5) for both initial conditions. This indicates that after 24 hours of simultaneous charging/discharging, the PCM phase inside the LHESS are similar independent of the initial PCM phase. Figure 6.6 shows the total energy input and recovered at the end of the 24 hour simultaneous charging/discharging experiments for the low cold HTF flow rate. The uncertainty in the energy calculations is large, therefore Fig. 6.6 is only used for identification of trends.

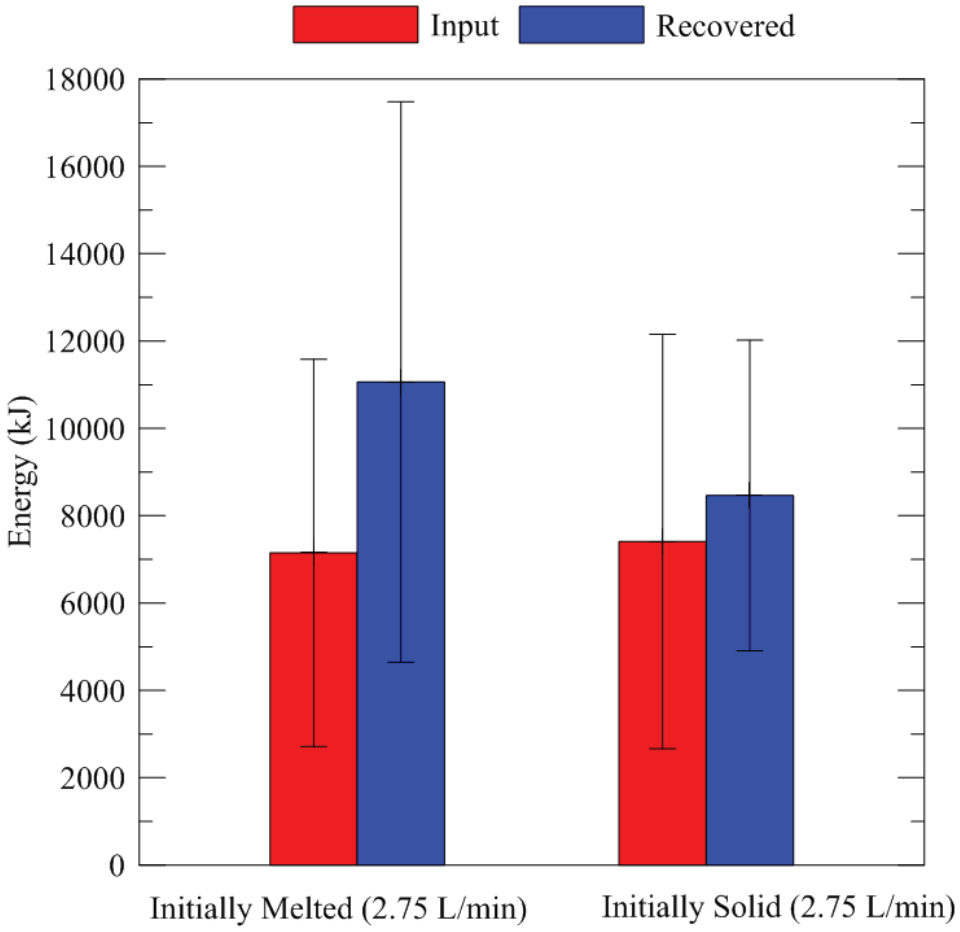


**Figure 6.6: Total energy supplied and recovered for the 24 hour simultaneous charging/discharging period using 2.75 L/min for the hot and cold HTF flow rates**

Based on Fig. 6.6, more energy is recovered than supplied during the 24 hour simultaneous charging/discharging experiment for both the initially melted and the initially solid case. However, the uncertainty in the energy calculations (and overlap in the error bars) is too large to draw any meaningful conclusions for the initially solid case.

### *6.3 Replicating a Solar Domestic Hot Water System*

The following experiments were done to replicate the operation of a LHESS used with a SDHW system during the day when solar energy is available. Throughout the day, energy is supplied to the LHESS (*i.e.* constantly charging the system), with intervals of energy extraction (*i.e.* a ten or twenty minute shower). To replicate this, the LHESS was simultaneously charged and discharged (domestic hot water use and solar energy input to the LHESS at the same time) for a fixed time interval, and then only charged (continuing to put energy into the LHESS, but no domestic hot water demand) for a fixed time interval. This cycle was repeated several times for each experiment, and several experiments were done with varying time intervals and flow rates, as shown in Table 6.1. One cycle includes the simultaneous charging/discharging period and the charging only period that follows. The flow rate of the cold HTF came from hot water end use data for single family dwellings collected by Aquacraft Incorporated Water Engineering and Management (DeOreo & Mayer, 2000).

**Table 6.3: Hot water usage in single family dwelling (DeOreo & Mayer, 2000)**

| Utility | Average flow rate (L/min) |
|---|---|
| Bath | 8.43 |
| Dishwasher | 4.65 |
| Shower | 5.7 |
| Faucets | 3.48 |
| Clothes washer | 7.9 |

Using the above data, high domestic hot water-use and low domestic hot water-use scenarios can be chosen to reflect a single family dwellings' hot water consumption. Assuming the dishwasher, faucets, and bath are all running, the flow rate will be 20 L/min, which is a high water-use scenario. Assuming only the shower is in use, the flow rate will be 5.7 L/min, which represents a low water-use scenario. These two flow rates were used for the cold HTF throughout Section 6.3.

A hot HTF flow rate of 2.75 L/min was used to reflect the glycol flow rate of a typical SDHW system of a single family dwelling as reflected by data available from a local company (Thermo-Dynamics, 2011) To summarize, the following experimental parameters were used for all experiments in Section 6.3:

**Table 6.4: Experimental parameters for Section 6.3**

| | |
|---|---|
| Hot HTF Temperature | 58 ± 0.5˚C |
| Cold HTF Temperature | 10 ± 0.5˚C |
| Hot HTF Flow Rate | 2.75 L/min |
| Cold HTF Flow Rate – High water-use | 20.0 L/min |
| Cold HTF Flow Rate – Low water-use | 5.7 L/min |

### 6.3.1 Initially Melted Phase Change Material

The LHESS was charged/discharged simultaneously for 10 minutes followed by 10 minutes of charging only (repeated until patterns emerged in the temperature profiles) with the PCM initially melted. Figure 6.7 shows the temperature profiles recorded for the high and low water-use scenarios.

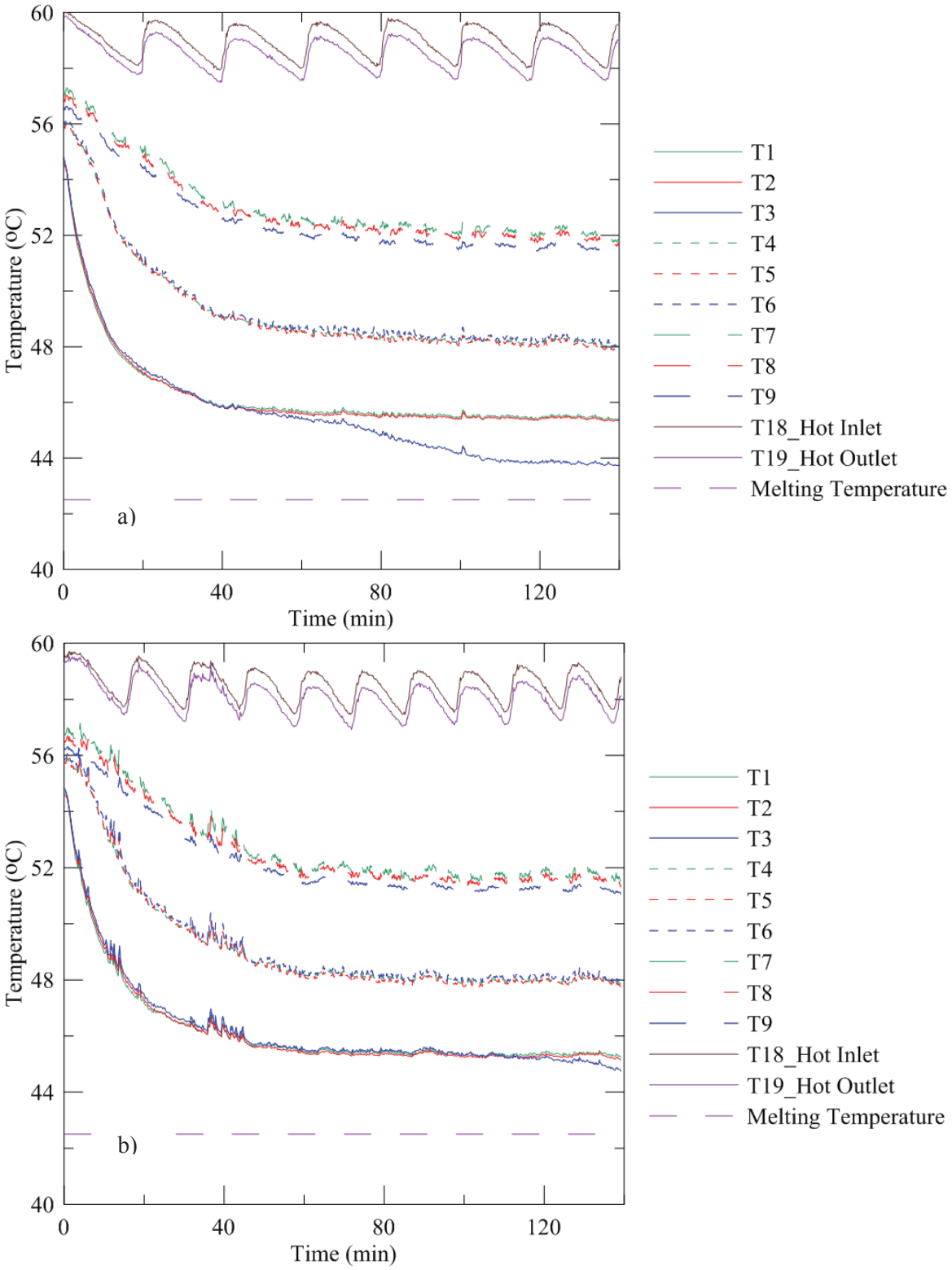


**Figure 6.7: Temperature profiles as a function of time measured during simultaneous charging/discharging with PCM initially melted a) 5.7 L/min b) 20 L/min cold HTF flow rate**

An initial drop in temperature is observed by all the probes, as seen in Figures 6.7-a) and b). This temperature drop is similar to the one discussed in Section 6.2, and is caused by an initial thermal shock to the system. The probes at the bottom of the container recorded the largest drop in temperature (T1, T2 and T3), followed by the second largest temperature drop recorded by the middle probes (T4, T5 and T6), and the smallest temperature drop recorded by the probes at the top of the container (T7, T8 and T9). This is a result of natural convection heat transfer displacing the energy supplied by the hot HTF to the top of the container. This stratification may be advantageous for a thermal energy storage system, as discussed in Chapter 2 (H. Mehling et al., 2003). After the initial drop in temperature, the PCM temperature profiles remain relatively constant. In Fig. 6.7-a) the PCM at the bottom of the LHESS on the side of the cold HTF pipe (T3 –blue line) began to decrease in temperature more than in Fig. 6.7-b) after the first 60 minutes of the experiment. This could be a result of a slight difference in the initial temperatures of the PCM in the 5.7 L/min experiment, as the same trend begins to happen after 120 minutes in Fig. 6.7-b). In Fig. 6.7 the cold HTF inlet and outlet temperatures are not shown, however, due to the scaling down of the size of the experimental LHESS, the temperature increase of the cold HTF was small (less than 1.5 $^{o}$C), particularly for the 20 L/min cold HTF flow rate.

Figure 6.8 shows the energy supplied and recovered after each cycle of simultaneous charging/discharging followed by only charging (every 20 minutes).

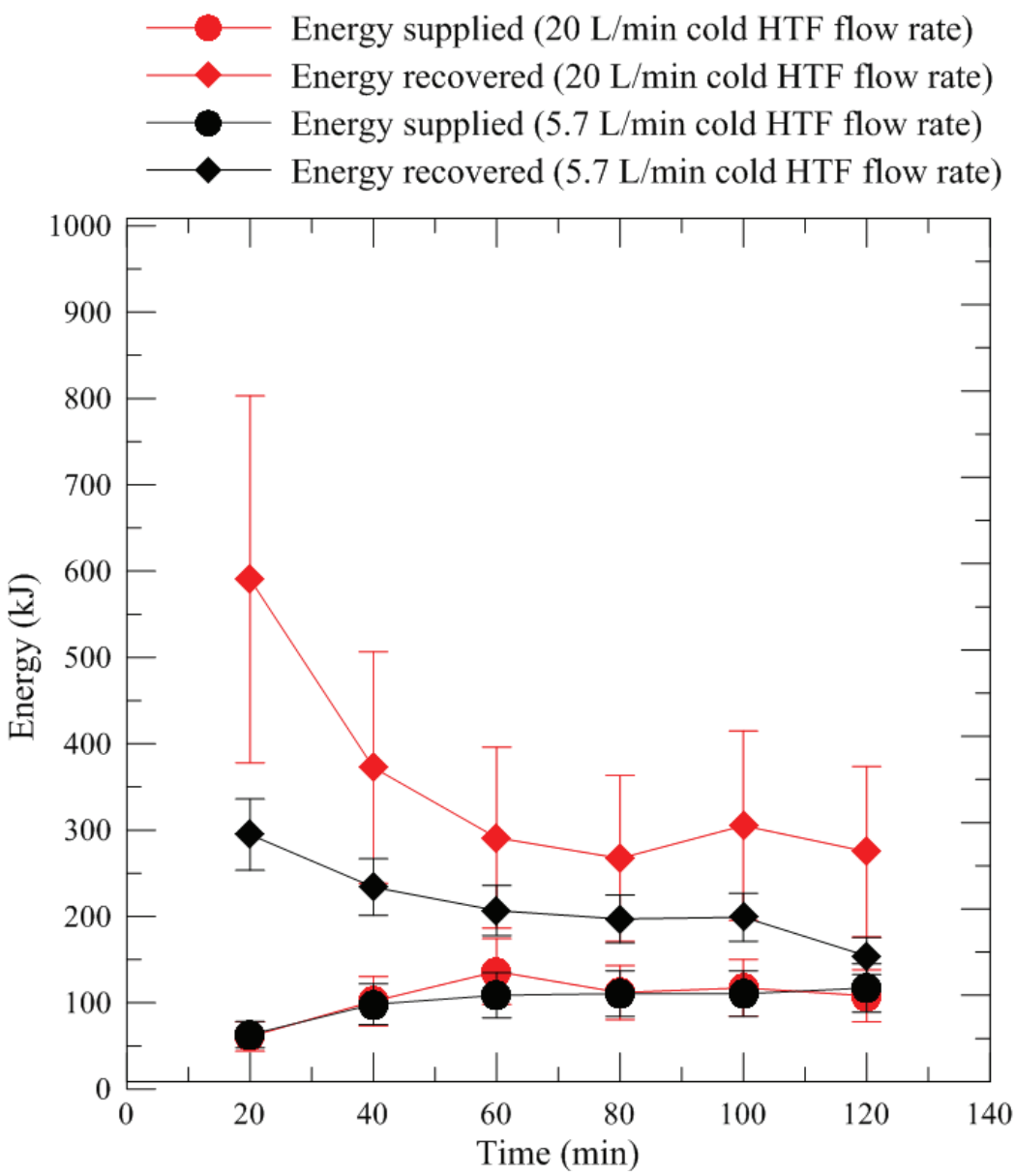


**Figure 6.8: Energy supplied and recovered each cycle during simultaneous charging/discharging with the PCM initially melted**

More energy is recovered (diamonds in Fig. 6.8) than input (circles in Fig. 6.8) when the PCM is initially melted, due to the additional energy available for collection by the cold HTF when the PCM solidifies. Because of this additional energy from the latent heat of the PCM, more energy is recovered by the cold HTF even though the LHESS is discharged for only half the time that it is charged (discharged for 10 minutes and charged for 20 minutes each cycle).

The energy input does not vary between the two experiments because the flow rate of the hot HTF is the same in both cases, whereas the energy recovered increases with the increasing flow rate of the cold HTF. This is contrary to what was found in the discharging only experiment in Section 5.5. In the discharging only experiment increasing the flow rate did not increase the rate of solidification because the PCM was mainly solid close to the cold HTF. In this experiment the LHESS is continuously being charged, which keeps some of the PCM above the melting temperature even close to the cold HTF pipe fins, as seen in Fig. 6.9.

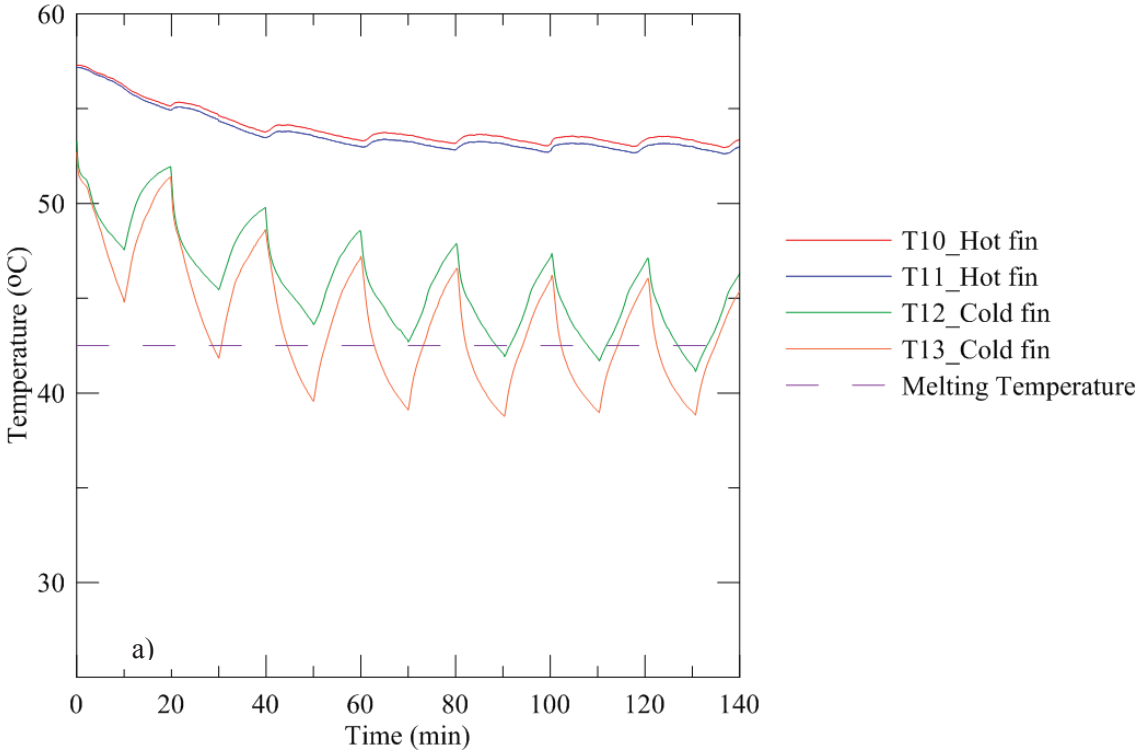


**Figure 6.9: Temperature profiles as a function of time measured by thermocouples on fins during simultaneous charging/discharging for a) 5.7 L/min cold HTF flow rate**

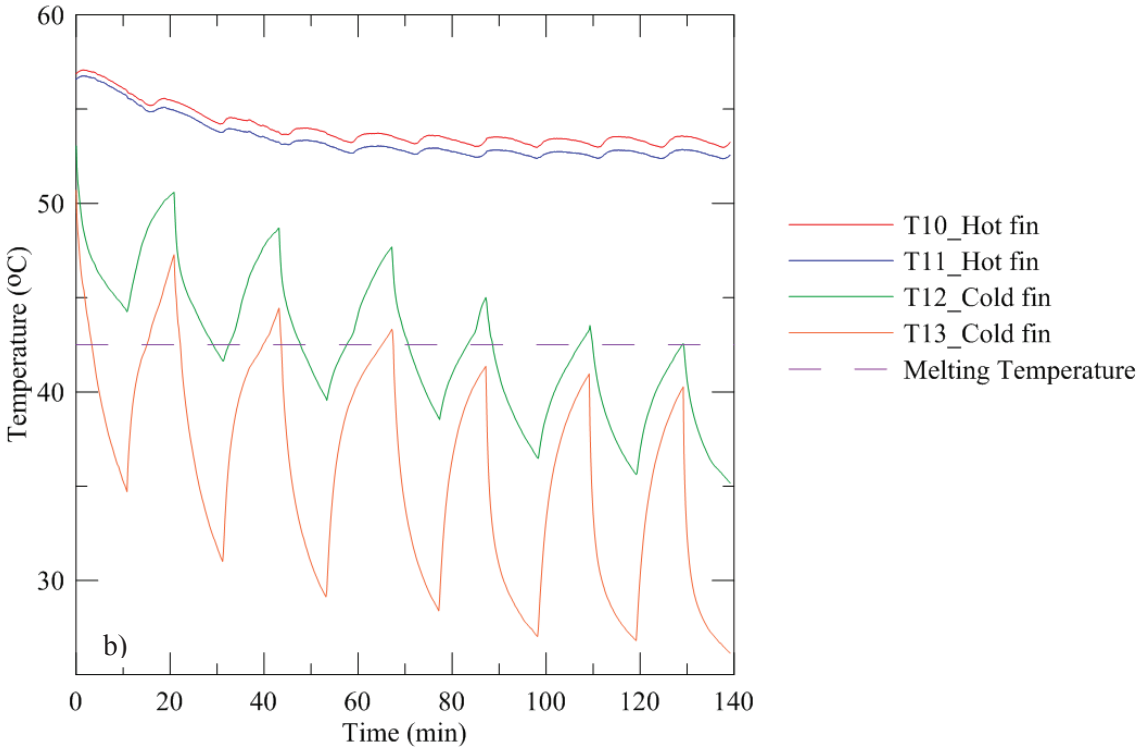


**Figure 6.9: Temperature profiles as a function of time measured by thermocouples on fins during simultaneous charging/discharging for b) 20 L/min cold HTF flow rate, continued**

In Fig. 6.9-a) the PCM close to the fins on the hot HTF pipe (T10 and T11) remained melted during the entire experiment, however the PCM close to the fins on the cold HTF pipe (T12 and T13) solidified and melted again each cycle. During each 10 minute period of discharging, thermocouples T12 and T13 (green and orange lines respectively) recorded temperatures dropping from above the melting temperature to below the melting temperature. Following this, during each 10 minute period of only charging, T12 and T13 recorded an increase in temperature back to above the melting/solidification temperature of the PCM. This means that each cycle the cold HTF solidified some of the PCM and absorbed energy from the PCM undergoing the phase change. In the discharging only experiment, after the PCM solidified close to the cold HTF pipe, it insulated the pipe and thus increasing the flow rate did not change how fast energy could be recovered. For these simultaneous experiments, the flow rate of the cold HTF affected how fast

energy was recovered from the PCM each cycle because the PCM was always melted when discharging began.

The energy charged and recovered for a variety of time intervals is shown in Fig 6.10. The energy values shown in Fig. 6.10 are the average energy input/recovered for each cycle, over a total of 5 cycles for each experiment presented. In this experiment, more energy can be recovered than input during the simultaneous charging/discharging period because of the energy already available in the system from the initially melted PCM. Initially, during charging to bring the PCM to the melted initial condition, 4860 kJ ± 51% was input to the system.

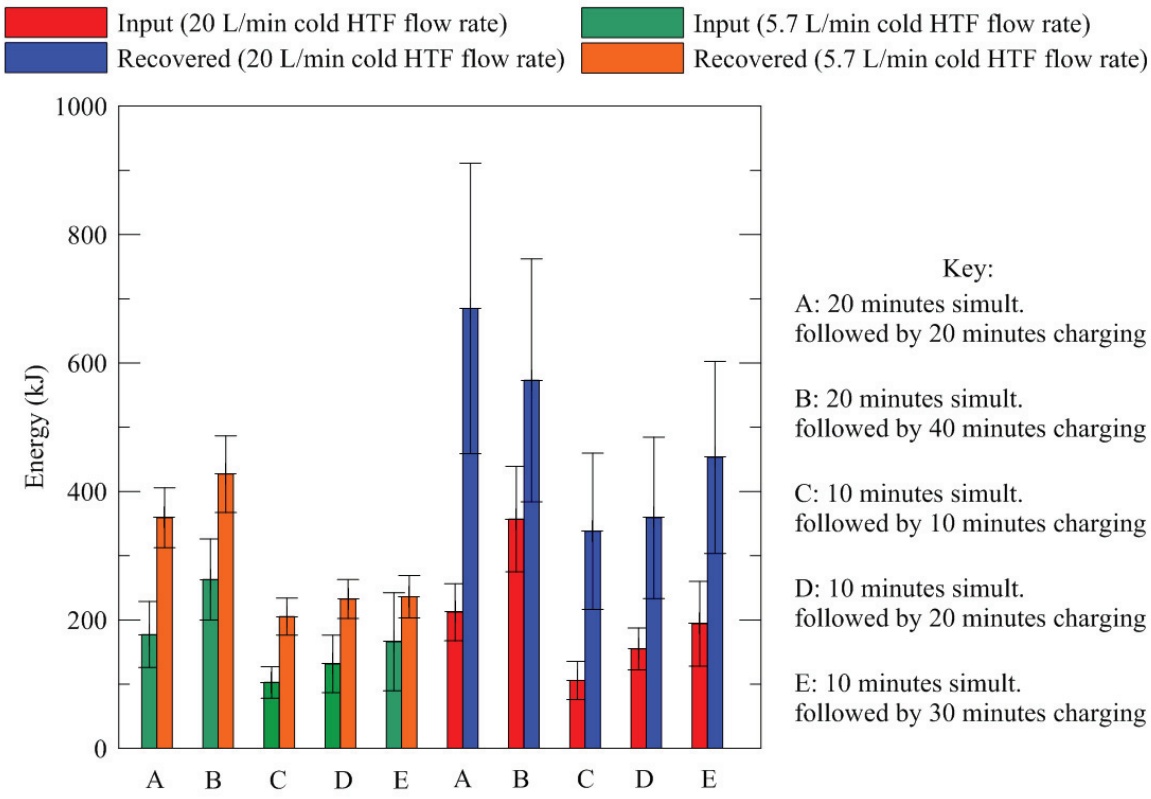


**Figure 6.10: Average energy supplied and recovered for the low water-use and the high water-use cases with the PCM initially melted**

Similar patterns were seen for the various time intervals, with more energy recovered than input for all the experiments. For the experiments done using the low cold HTF flow rate, more energy

is recovered (orange bars) as the discharging time increases, and more energy is input (green bars) as the charging time increases. For the high flow rates, similar patterns emerge, however, there are some anomalies, such as the energy patterns for time intervals A and B (red and blue bars). More energy should have been recovered in B since more energy was input by the hot HTF. These anomalies are attributed to the large uncertainty in the energy calculations for the higher flow rate. The repetitiveness of the patterns for the low flow rate case provides a higher level of confidence in the results. Because the energy input/recovered is dependent on the time intervals, it is of interest to look at the results independent of the time period. Figure 6.11 shows the power supplied and recovered. The power shown in Fig. 6.11 is the average energy input/recovered for each cycle, as presented in Fig. 6.10, divided by the time length of charging/discharging for each cycle.

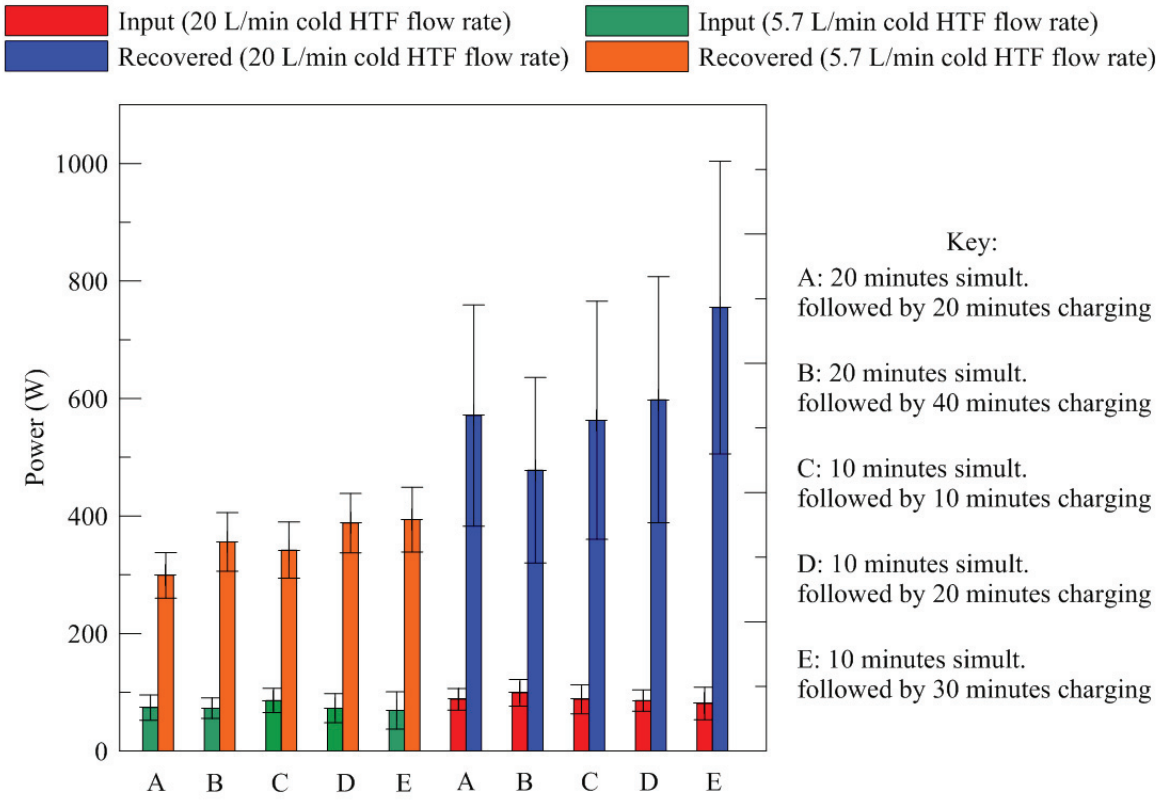


**Figure 6.11: Average power supplied and recovered for the low water-use and the high water-use cases with the PCM initially melted**

Due to the uncertainty in the power calculations, Fig. 6.11 is only used for trend identification. Based on Fig. 6.11, a clear pattern is observed, with relatively constant power being input for all the experiments. The power recovered from the PCM varies, with more power recovered as the charging time increases.

### 6.3.2 Initially Solid Phase Change Material

The LHESS was charged/discharged simultaneously for 10 minutes followed by 10 minutes of only charging (repeated until patterns emerged in the temperature profiles) with the PCM initially solid. Figure 6.12 shows the temperature profiles recorded for the high and low water-use scenarios.

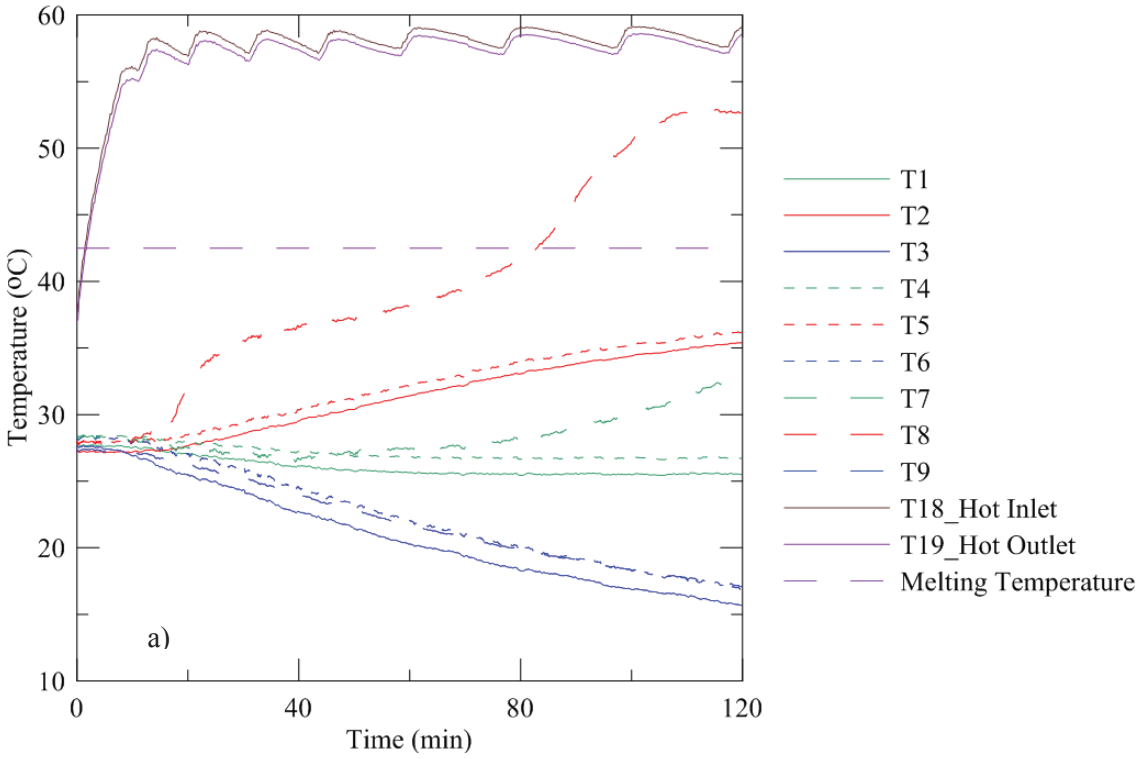


**Figure 6.12: Temperature profiles as a function of time measured during simultaneous charging/discharging with PCM initially solid a) 5.7 L/min cold HTF flow rate**

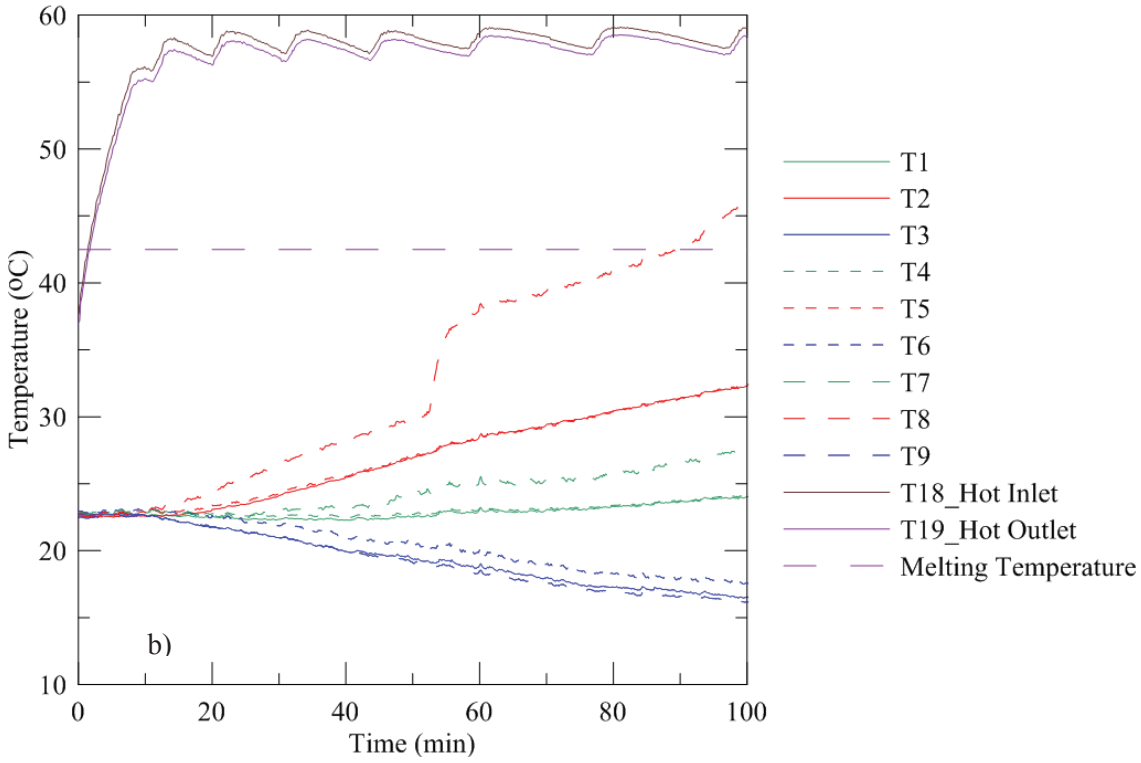


**Figure 6.12: Temperature profiles as a function of time measured during simultaneous charging/discharging with PCM initially solid b) 20 L/min cold HTF flow rate, continued**

In the initially solid case, the PCM did not stratify the same way it did in the initially melted case presented in Section 6.3.1. This is because the solid PCM cannot move, and the PCM that does melt has nowhere to move without first supplying energy to melt the surrounding PCM. In this case, the PCM temperatures at the middle of the LHESS (T1, T4 and T7- green lines) remained relatively constant, while the PCM close to the hot pipe (T2, T5 and T8- red lines) heated up and the PCM close to the cold pipe (T3, T6 and T9- blue lines) cooled down. Even though the PCM is initially solid, energy can still be recovered from the solid PCM because it is 10$^{o}$C warmer than the cold HTF. Melting was only recorded at the top probe location on the hot side (T8), while the middle probe at the top height (T7) measured an increase in temperature more than the middle thermocouple probes at the bottom and middle height. The PCM around the hot fins melted as well, as seen in Fig. 6.13, for both high and low flow rates.

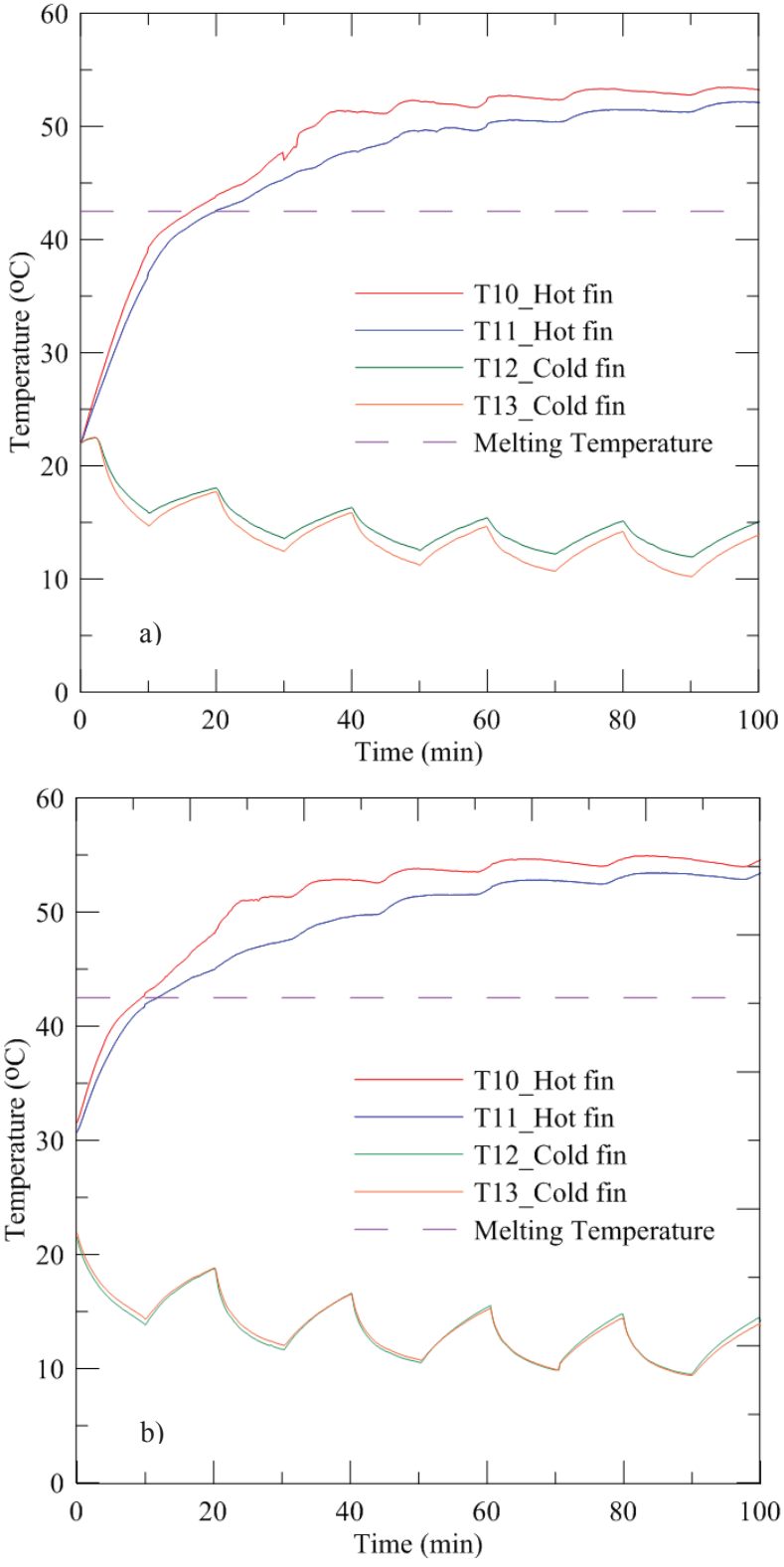


**Figure 6.13: Temperature profiles as a function of time measured by thermocouples on fins during simultaneous charging/discharging with PCM initially solid a) 5.7 L/min cold HTF flow rate b) 20 L/min cold HTF flow rate**

As seen in Fig. 6.13, the temperature of the PCM close to the fins, particularly around the cold pipe, fluctuated with each cycle of simultaneous charging/discharging and charging, similar to the initially melted experiments presented in Section 6.3.1. The PCM close to the hot fins heated up and melted within the first cycle, and then remained melted. This indicates that heat is being transferred from the hot HTF to the PCM through the fins, as expected.

The energy supplied and recovered during each cycle is given in Fig. 6.14.

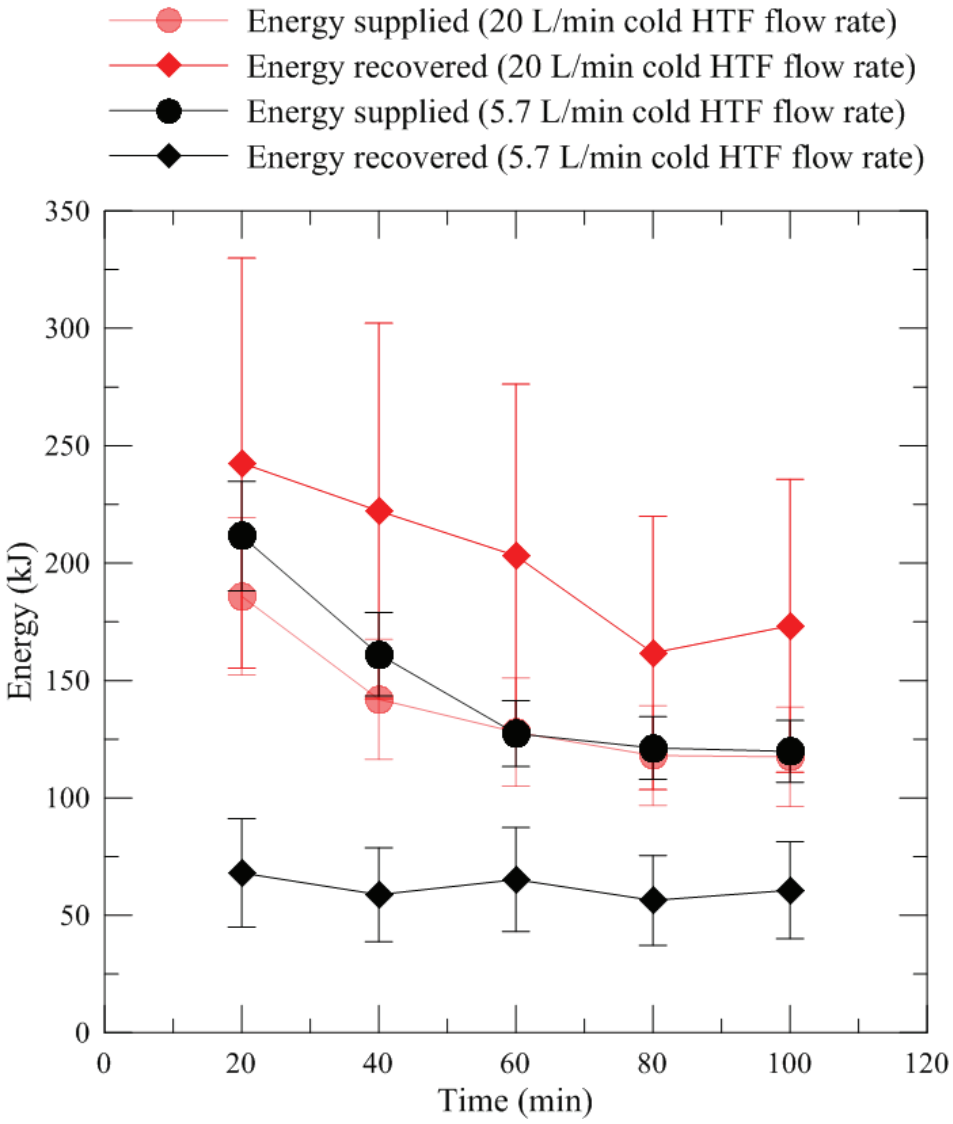


**Figure 6.14: Energy supplied and recovered each cycle during simultaneous charging/discharging with the PCM initially solid**

The energy input does not vary between the two experiments because the flow rate of the hot HTF is the same (2.75 L/min) for both experiments. In Fig. 6.12 the patterns in the PCM temperature profiles (*i.e.* how much of the PCM is melted and solid based on the probe temperature readings) are similar for both cold HTF flow rates. Therefore, similar energy trends are expected for both cold HTF flow rates. In the low flow rate experiment more energy is supplied (red circle) than recovered (red diamond), as expected, since the hot HTF can expend more energy by melting the PCM. However, for the high flow rate, more energy is recovered than supplied. The same results are found when this experiment is done using different time intervals at the high flow rate, as shown Fig. 6.15. The energy values shown in Fig. 6.15 are the average energy input/recovered for each cycle, over a total of at least 5 cycles for each experiment presented.

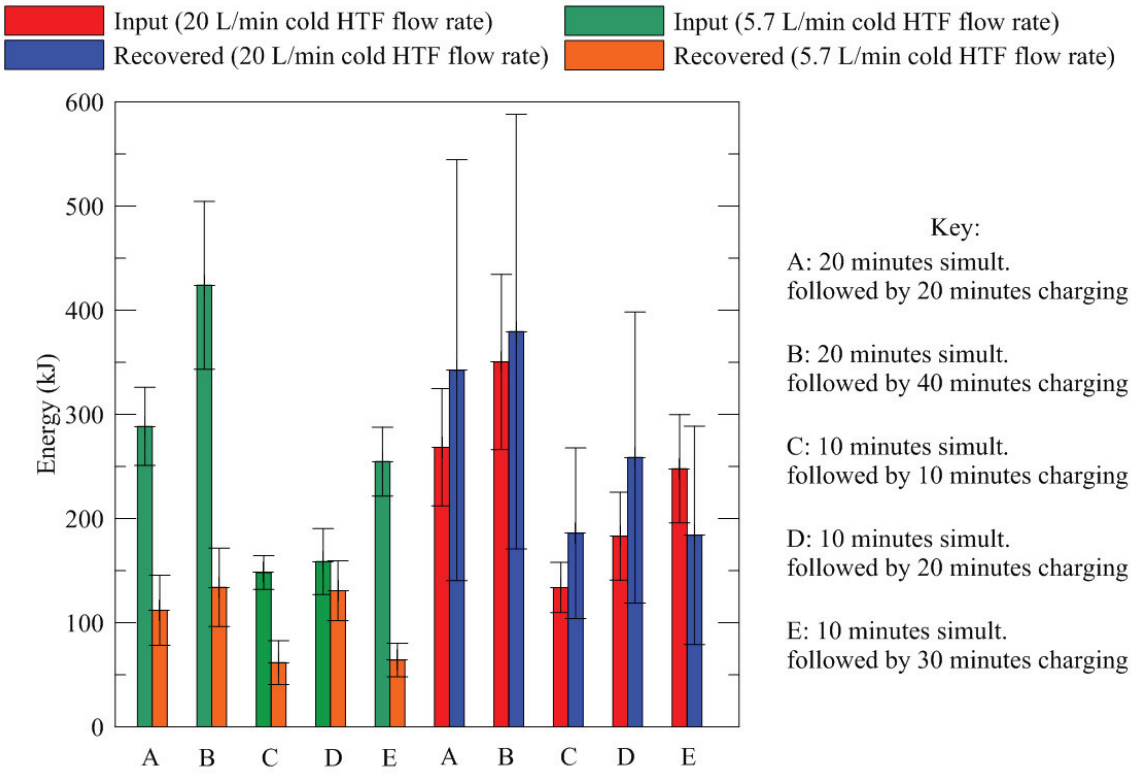


**Figure 6.15: Average energy supplied and recovered for the low water-use and the high water-use cases with the PCM initially solid**

More energy recovered than input at the 20 L/min cold HTF flow rate may be a result of the significantly higher cold HTF flow rate than hot HTF flow rate (20 L/min compared to 2.75 L/min) which may make up for the increased energy expended by the hot HTF when it melts the PCM. However, these energy trends could also be a result of the high uncertainty in the energy calculations for the high flow rate experiments, making it difficult to draw conclusions from these results. The power input and recovered for these experiments is given in Fig. 6.16. The power shown in Fig. 6.16 is the average energy input/recovered for each cycle, as presented in Fig. 6.15, divided by the time length of charging/discharging for each cycle.

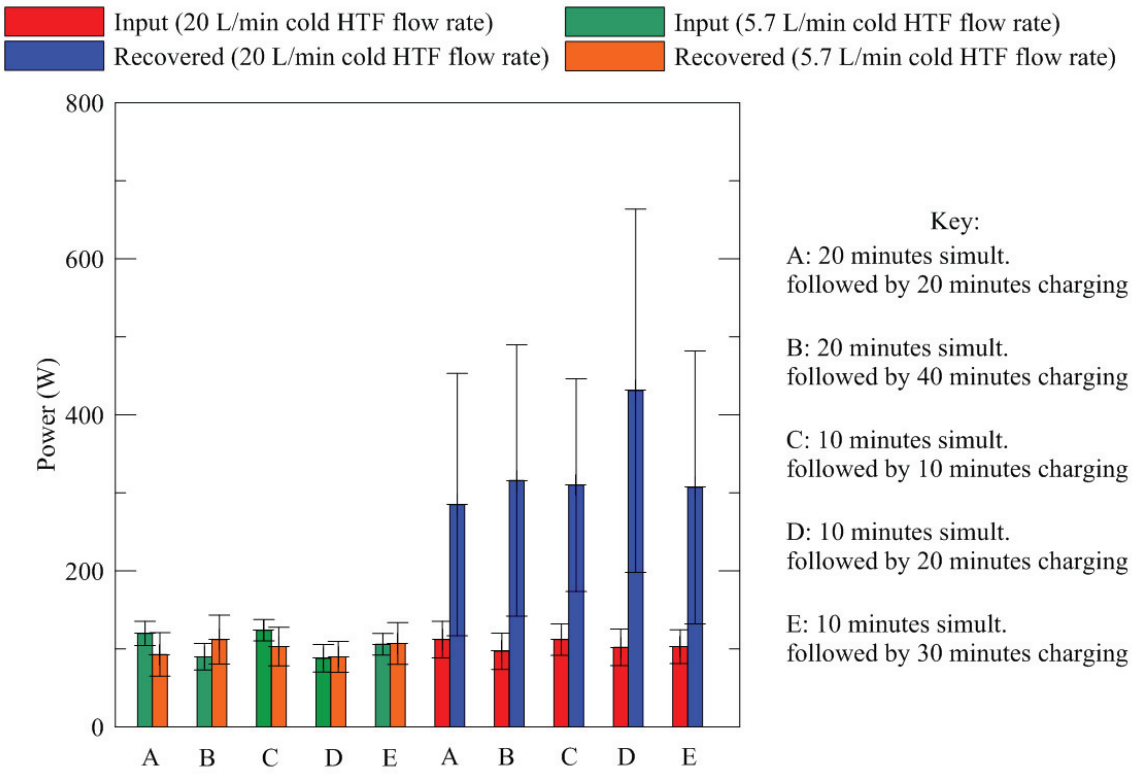


**Figure 6.16: Average power supplied and recovered for the low water-use and the high water-use cases with the PCM initially solid**

Similarly to Section 6.3.1, the same amount of power is input, independent of the flow rate of the cold HTF, because the hot HTF flow rate is the same for all the experiments. For the lower cold HTF flow rate, the same amount of power is supplied and recovered. However, for the 20 L/min

cold HTF more power is recovered by the cold HTF than input by the hot HTF, which is similar to the trend observed in Fig. 6.14.

## *6.4 Simultaneous Compared to Separate Charging and Discharging*

In Section 6.4 the energy input and recovered during simultaneous charging/discharging (Chapter 6) is compared to the energy input and recovered during separate charging/discharging (Chapter 5). This will give an indication of the impact the high thermal resistance of the PCM has on direct heat transfer between the hot and cold HTFs during simultaneous charging/discharging.

### 6.4.1 Energy Supplied

To determine the contribution of the energy supplied by the hot HTF to the cold HTF directly, the separate charging case is compared to the simultaneous charging/discharging case, as shown in Fig. 6.15.

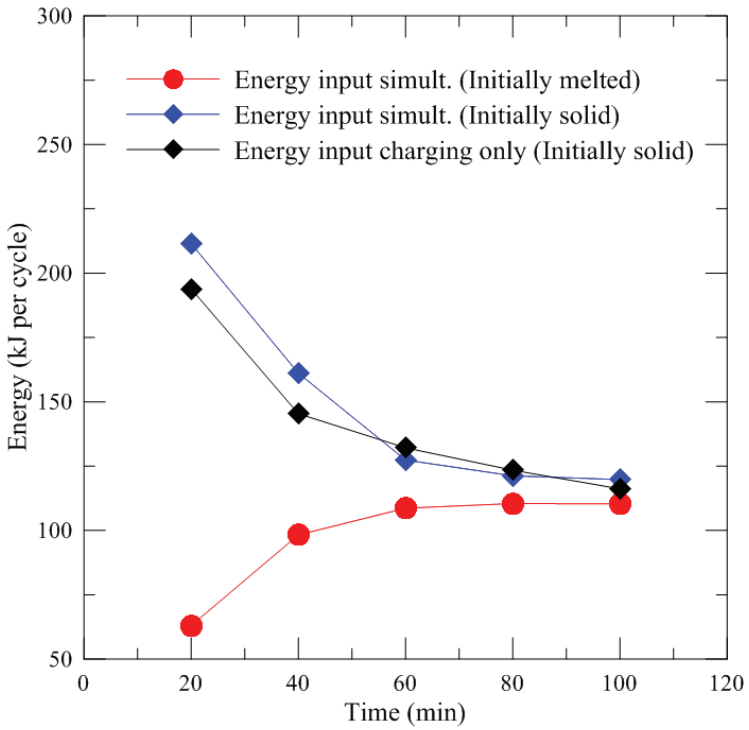


**Figure 6.17: Energy input during simultaneous charging/discharging compared to energy input during charging only (2.75 L/min hot HTF flow rate)**

In the charging experiment shown here the same hot HTF flow rate was used as in the simultaneous experiments in Section 6.3 (2.75 L/min). A 20 minute time interval for the energy input calculations in the charging only case was chosen to allow for a direct comparison to the energy input during each 20 minute charging period in a cycle of simultaneous charging/discharging (the experimental results presented in Section 6.3).

Figure 6.15 shows that only slightly more energy was input by the hot HTF during simultaneous experiments than during the charging only experiment. In Fig. 6.15 more energy is input to the LHESS when the PCM is initially solid because it goes through a phase transition. However, because the PCM is solid when charging begins, the high thermal resistance of the solid PCM limits direct energy transfer from the hot HTF to the cold HTF, therefore close to the same amount of energy is input during the simultaneous experiments as during the charging only experiment. In the initially solid simultaneous charging/discharging case, once the PCM close to the hot HTF pipe has melted the energy input by the hot HTF decreases (blue line in Fig. 6.15). In the initially melted case, once the energy recovered by the cold HTF solidifies the PCM, the energy input by the hot HTF increases (red line in Fig. 6.15). This is clear in Fig. 6.15, where after 80 minutes of simultaneous charging/discharging the same amount of energy is input in the initially melted and initially solid case.

### 6.4.2 Energy Recovered

In order to determine the contribution of the energy recovered by the cold HTF from the hot HTF directly, the separate discharging case is compared to the simultaneous charging/discharging case, as shown in Fig. 6.16.

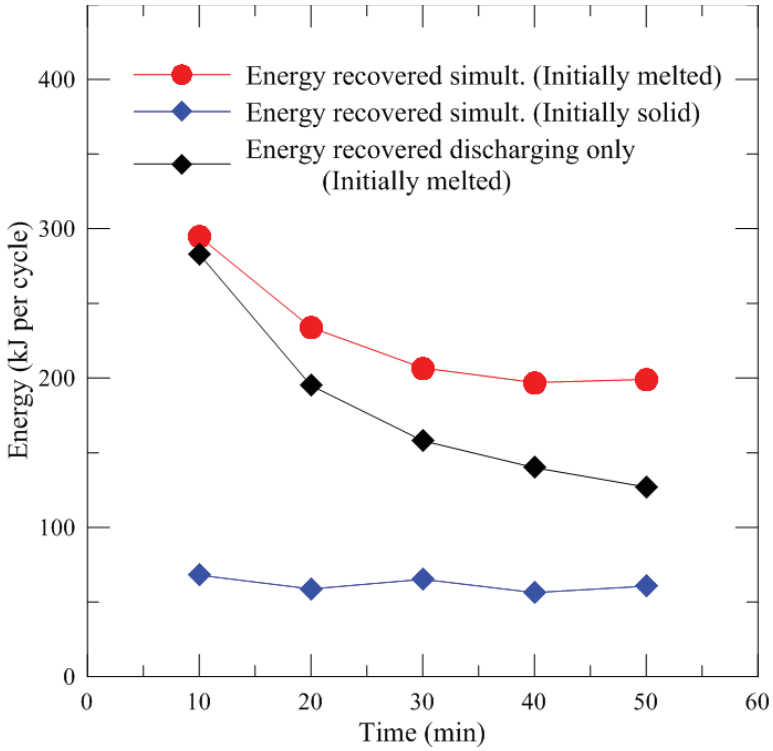


**Figure 6.18: Energy recovered during simultaneous charging/discharging compared to energy recovered during discharging only (5.7 L/min cold HTF flow rate)**

For the discharging only experiment, the same discharging flow rate was used as the low water-use flow rate used in the simultaneous experiments in Section 6.3 (5.7 L/min). A 10 minute time interval for the energy calculations in the discharging only case was chosen to allow for a direct comparison to the energy recovered during each cycle of simultaneous charging/discharging (the experimental results presented in Section 6.3), in which the system was only discharged for 10 minutes of the 20 minute cycle.

From Fig. 6.16, more energy is recovered when the LHESS is operated simultaneously and the PCM is initially melted (red line in Fig. 6.16) than during discharging only (black line in Fig. 6.16). This indicates that some of the energy recovered by the cold HTF during simultaneous operation comes directly from the hot HTF. Therefore, the thermal resistance of the initially melted PCM does not completely inhibit heat transfer between the hot and cold HTFs like it did in the initially solid case discussed in Section 6.4.1. This shows the difference in the heat transfer

characteristics of a solid and a melted PCM. Melted PCMs can accommodate increased heat transfer rates by consequently increasing natural convection throughout the melted PCM. However, heat transfer through solid PCM is clearly limited by the thermal resistance of the solid, and the absence of natural convection effects.

### *6.5 Summary*

To summarize the discussions in Chapter 6, it was found that during simultaneous charging and discharging, significant direct heat transfer between the hot and cold HTFs only occurs when the PCM is melted. The low thermal conductivity of the solid PCM limits heat transfer. These results indicate that during simultaneous operation of the LHESS, charging and discharging occurs independently when the PCM between the two HTF pipes is solid.

# Chapter 7 Conclusion

SDHW systems are a cost effective and efficient way to use a renewable thermal energy source for domestic water heating. However, large-scale deployment of SDHW systems may be limited by the space and weight required for energy storage. The work in this thesis was done to further develop PCM energy storage technology which could increase the uptake of SDHW systems by reducing the space and weight required for energy storage. The literature review in Chapter 2 clearly indicated the need for experimental studies of simultaneous charging and discharging, which is an operating mode that would be encountered when using a LHESS with SDHW. The main objective of this research was to produce and analyze experimental data for all operating modes of a LHESS used with a SDHW system. An experimental LHESS, with dodecanoic acid as the PCM, was designed and built for this research, and a conduction-only numerical model was used to demonstrate the onset of natural convection inside the system.

The experiments done throughout this thesis have provided valuable insight into the heat transfer and phase change behavior of a PCM in a LHESS. During consecutive charging and discharging experiments it was found that natural convection is the main mechanism of heat transfer during charging, and conduction is the main mechanism of heat transfer during discharging. This was also verified by comparing experimental results to the conduction-only numerical model. In many phase change problems the Stefan number is used to define the system. However, the results of this thesis show that there are more factors involved in phase change problems than just the influence of the temperatures and thermophysical properties of the PCM, which are used in the Stefan number. For example, using the experimental LHESS, it was found that the HTF flow rate affected the rate of melting, but not of solidification.

During simultaneous charging/discharging modes, more energy can be recovered from a system when the PCM is melted, and more energy can be input when the PCM is solid. It was also found

that direct heat transfer between the hot and cold HTFs is only possible when the PCM between the two HTF pipes is melted. When the PCM is solid between the HTF pipes heat transfer is limited by the high thermal resistance of the solid PCM.

### *7.1 Recommendations*

Conduction is the main mechanism of heat transfer during solidification, therefore future heat transfer enhancement designs for LHESS should be geared towards discharging, since solidification does not benefit from the effects of natural convection like melting does. As well, convection heat transfer during charging results in more melted PCM rising to the top of the container. Future LHESS designs should take this into consideration for energy recovery, because it means that more energy is available for recovery at the top of the container.

Because the LHESS designed for this research was a scaled down model of an actual LHESS for use with SDHW, the PCM in the LHESS required over 30 hours to fully melt. However, the purpose of this experiment was not be to store and recover energy quickly, but to track PCM temperatures and gain a better understanding of the heat transfer processes inside the system. Although this system was scaled down, the physical processes inside it will remain the same, as long as future designs do not impeded natural convection heat transfer. It was shown in Section 5.4 that the power output of a single flat plat solar collector is greater than the power capacity of the LHESS designed for this thesis. In order to increase the power, the time required for the LHESS to charge/discharge needs to be decreased. To decrease charging/discharging times, future LHESS designs should have more passes of the HTF pipes through the PCM to extract and store energy faster. A HTF pipe which coils through the PCM will result in a larger surface area for heat transfer, and therefore will reduce melting/solidification times. LHESS designs which have coiled HTF pipes will enable more precise energy calculations due to the larger temperature difference between the inlet and outlet; however, the more complex design will make identifying

heat transfer patterns and PCM behavior more difficult. The temperature drop over the length of the HTF pipe needed for faster charging can be used to determine the characteristic length of pipe (or surface area for heat transfer) required for the power expected from a single flat plate solar collector.

A LHESS used with SDHW should operate as a heat exchanger between the hot and cold HTFs when there is a demand for domestic hot water at the same time as solar energy is available. Based on the results presented in Chapter 6, the system designed for this thesis will not always be appropriate for this task, since when the PCM is solid in the LHESS, direct heat exchange between the hot and cold HTF is greatly limited. For this reason, design refinements must be made to improve heat transfer from one HTF to the other. Points of direct contact between the hot and cold HTF pipes, such as extended fins that attach both HTF pipes, should be added to decrease the thermal resistance between the hot and cold HTFs.

Temperature fluctuations in the inlet temperature of the hot HTF as a result of the immersion heater were observed when the hot HTF was run at high flow rates. This is not an issue for the research done in this thesis because the energy storage calculations are determined based on the inlet and outlet temperature differences. However, to correct these fluctuations for future experimental setups, a VARIAC or PID controller should be used. As well, any fluctuations in the cold HTF inlet temperature because of the municipal water source were uncontrollable; therefore, a constant temperature cold water bath using a chiller should be implemented to allow more control over the cold HTF temperature.

The model built in COMSOL was a conduction-only finite element model. In order to fully model the system, convection heat transfer needs to be implemented. A 3D model will be needed for this in order to take into account the variation in temperature with respect to the height of the LHESS.

As well, this 3D model should simulate simultaneous charging and discharging in order to further explore the effects of natural convection inside the system under this operating mode.

### *7.2 Conclusion*

Along with its other benefits, LHESS can provide a valuable solution for correcting the mismatch between the energy supply and demand of a SDHW system. However, there are many design refinements that need to be made before such a system is ready for large scale deployment. The numerical model presented in this thesis had conduction heat transfer only, which resulted in large deviations from experimental results once melting began. Natural convection was shown to play a major role during and after melting, and therefore needs to be included in numerical models of this system. Design optimization may be done using numerical models to save time and money, however without accurate experimental data, it is impossible to validate such a model. This research provides results that can be used to validate a numerical model, making it a step towards a well-designed LHESS for use with SDHW.

## References


Abhat, A. (1983). Low temperature latent heat thermal energy storage: Heat storage materials. *Solar Energy, 30*(4), 313-332.

Agyenim, F., Eames, P., & Smyth, M. (2009). A comparison of heat transfer enhancement in a medium temperature thermal energy storage heat exchanger using fins. *Solar Energy, 83*(9), 1509-1520.

Agyenim, F., Eames, P., & Smyth, M. (2010). Heat transfer enhancement in medium temperature thermal energy storage system using a multitube heat transfer array. *Renewable Energy, 35*(1), 198-207.

Agyenim, F., & Hewitt, N. (2010). The development of a finned phase change material (PCM) storage system to take advantage of off-peak electricity tariff for improvement in cost of heat pump operation. *Energy and Buildings, 42*(9), 1552-1560.

Agyenim, F., Hewitt, N., Eames, P., & Smyth, M. (2010). A review of materials, heat transfer and phase change problem formulation for latent heat thermal energy storage systems (LHTESS). *Renewable and Sustainable Energy Reviews, 14*(2), 615-628.

Agyenim, F., Knight, I., & Rhodes, M. (2010). Design and experimental testing of the performance of an outdoor LiBr/H2O solar thermal absorption cooling system with a cold store. *Solar Energy, 84*(5), 735-744.

Akgun, M., Aydin, O., & Kaygusuz, K. (2007). Experimental study on melting/solidification characteristics of a paraffin as PCM. *Energy Conversion and Management, 48*(2), 669-678.

Al-Hinti, I., Al-Ghandoor, A., Maaly, A., Abu Naqeera, I., Al-Khateeb, Z., & Al-Sheikh, O. (2010). Experimental investigation on the use of water-phase change material storage in conventional solar water heating systems. *Energy Conversion and Management, 51*(8), 1735-1740.

Alva S, L. H., GonzáLez, J. E., & Dukhan, N. (2006). Initial analysis of PCM integrated solar collectors. *Journal of Solar Energy Engineering, 128*(2), 173.

Bajnoczy, G., Gagyi, P., Prepostffy, E. O., & Zold, A. ( 2000). Heat storage by two-grade phase change material. *Periodica Polytechnica Chemical Engineering, 43*(2), 137-147.

Cabeza, L., Ibanez, M., Sole, C., Roca, J., & Nogues, M. (2006). Experimentation with a water tank including a PCM module. *Solar Energy Materials and Solar Cells, 90*(9), 1273-1282.

Cabeza, L. F., Mehling, H., Hiebler, S., & Ziegler, F. (2002). Heat transfer enhancement in water when used as PCM in thermal energy storage. *Applied Thermal Engineering, 22*, 1141–1151.

Canbazoglu, S., Sahinaslan, A., Ekmekyapar, A., Aksoy, Y., & Akarsu, F. (2005). Enhancement of solar thermal energy storage performance using sodium thiosulfate pentahydrate of a conventional solar water-heating system. *Energy and Buildings, 37*(3), 235-242.

Castell, A., Sole, C., Medrano, M., Roca, J., Cabeza, L., & Garcia, D. (2008). Natural convection heat transfer coefficients in phase change material (PCM) modules with external vertical fins. *Applied Thermal Engineering, 28*(13), 1676-1686.

C. L. Yaws, McGraw-Hill (1999) Chemical Properties Handbook, Online version available at: http://knovel.com.ezproxy.library.dal.ca/web/portal/browse/display?_EXT_KNOVEL_DISPLAY_bookid=49&VerticalID=0

Chen, Z., Gu, M., & Peng, D. (2010). Heat transfer performance analysis of a solar flat-plate collector with an integrated metal foam porous structure filled with paraffin. *Applied Thermal Engineering, 30*(14-15), 1967-1973.

Deoreo, W. B., & Mayer, P. W. (2000). *The end uses of hot water in single family homes from flow trace analysis*.Unpublished manuscript, Colorado, USA.

Desgrosseilliers, L., Murray, R., Safatli, A., Marin, G., Stewart, J., Osbourne, N., White, M. A., & Groulx, D. (2011). *Phase change material selection in the design of a latent heat energy storage system coupled with a domestic hot water solar thermal system.* Paper presented at the 2011 ASHRAE Annual Conference, Montreal, Canada.

Desgrosseilliers, L., Whitman, C., Groulx, D., & White, M. A. (2012). Dodecanoic Acid As a Promising Phase-Change Material for Thermal Energy Storage. Submitted to *Renewable Energy.*

Dutil, Y., Rousse, D. R., Salah, N. B., Lassue, S., & Zalewski, L. (2011). A review on phase-change materials: Mathematical modeling and simulations. *Renewable and Sustainable Energy Reviews, 15*(1), 112-130.

El-Qarnia, H. (2009). Numerical analysis of a coupled solar collector latent heat storage unit using various phase change materials for heating the water. *Energy Conversion and Management, 50*(2), 247-254.

Ettouney, H., El-Dessouky, H., & Al-Kandari, E. (2004). Heat transfer characteristics during melting and solidification of phase change energy storage process. *Ind. Eng. Chem. Res, 43*, 5350-5357.

Farid, M. (2004). A review on phase change energy storage: materials and applications. *Energy Conversion and Management, 45*(9-10), 1597-1615.

Fernandez, A. I., Martínez, M., Segarra, M., Martorell, I., & Cabeza, L. F. (2010). Selection of materials with potential in sensible thermal energy storage. *Solar Energy Materials and Solar Cells, 94*(10), 1723-1729.

Godarzi, A. A., Jalilian, M., Vesaghi, M. A., & Samimi, J. (2010). *Numerical analysis of the thermal behavior of a rectangular storage system using phase change materials* Paper presented at the SOLAR 2010 Conference

Gong, Z.-X., & Mujumdar, A. S. (1997). Finite element analysis of cyclic heat transfer in a shell and tube latent heat energy storage exchanger *Applied Thermal Engineering, 17*(6), 583-591.

Hamada, Y. (2003). Thermal response in thermal energy storage material around heat transfer tubes: effect of additives on heat transfer rates. *Solar Energy, 75*(4), 317-328.

Hendra, R., Mahlia, T., & Masjuki, H. (2005). Thermal and melting heat transfer characteristics in a latent heat storage system using mikro. *Applied Thermal Engineering, 25*(10), 1503-1515.

Incropera, F., Dewitt, D., Bergman, T., & Lavine, A. (2007). *Fundamentals of Heat and Mass Transfer* (Vol. 6). United States: John Wiley & Sons Inc.

Incropera, F. P. (2007). *Introduction to heat transfer*: Hobokenm NJ : Wiley, ©2007.

Ismail, K. a. R., & Abugdera, M. M. (2000). Performance of a thermal storage system of the vertical tube type. *Energy Conversion & Management, 41*, 1165-1190.

Ismail, K. a. R., & Henrõâquez, J. R. (2000). Solidification of pcm inside a spherical capsule. *Energy Conversion & Management, 41*, 173-187.

Ismail, K. a. R., Henrõâquez, J. R., Moura, L. F. M., & Ganzarolli, M. M. (2000). Ice formation around isothermal radial finned tubes. *Energy Conversion & Management, 41*, 585-605.

Jegadheeswaran, S., & Pohekar, S. D. (2009). Performance enhancement in latent heat thermal storage system: A review. *Renewable and Sustainable Energy Reviews, 13*(9), 2225-2244.

Jian-You, L. (2008). Numerical and experimental investigation for heat transfer in triplex concentric tube with phase change material for thermal energy storage. *Solar Energy, 82*(11), 977-985.

Kaygusuz, K. (1995). Experimental and theoretical investigation of latent heat storage for water based solar heating systems. *Energy Convers. Mgmt, 36*(5), 315-323.

Kaygusuz, K. (2003). Phase change energy storage for solar heating systems. *Energy Sources, Part A: Recovery, Utilization, and Environmental Effects, 25*(8), 791-807.

Kaygusuz, K., & Sari, A. (2005). Thermal energy storage system using a technical grade paraffin wax as latent heat energy storage material. *Energy Sources, 27*(16), 1535-1546.

Kenisarin, M., & Mahkamov, K. (2007). Solar energy storage using phase change materials☆. *Renewable and Sustainable Energy Reviews, 11*(9), 1913-1965.

Khodadadi, J. M., & Zhang, Y. (2001). Effects of buoyancy-driven convection on melting within spherical containers. *International Journal of Heat and Mass Transfer, 44*, 1605-1618.

Koca, A., Oztop, H., Koyun, T., & Varol, Y. (2008). Energy and exergy analysis of a latent heat storage system with phase change material for a solar collector. *Renewable Energy, 33*(4), 567-574.

Lacroix, M. (1993). Study of the heat transfer behavior of a latent heat thermal energy storage unit with a finned tube. *International Journal of Heat and Mass Transfer, 36*(8), 2083-2092.

Lamberg, P. (2004). Approximate analytical model for two-phase solidification problem in a finned phase-change material storage. *Applied Energy, 77*(2), 131-152.

Liu, Z., Wang, Z., & Ma, C. (2006). An experimental study on the heat transfer characteristics of a heat pipe heat exchanger with latent heat storage. Part II: Simultaneous charging/discharging modes. *Energy Conversion and Management 47* 967–991.

Liu, Z., Wang, Z., & Ma, C. (2006a). An experimental study on heat transfer characteristics of heat pipe heat exchanger with latent heat storage. Part I: Charging only and discharging only modes. *Energy Conversion and Management 47* 944–966.

Mehling, & Cabeza, L. (2008). *Heat and cold storage with PCM: An up to date introduction into basics and applications*. Verlag Berlin Heidelberg: Springer.

Mehling, H., & Cabeza, L. (Eds.). (2008). *Heat and Mass Transfer* Springer.

Mehling, H., Cabeza, L. F., Hippeli, S., & Hiebler, S. (2003). PCM-module to improve hot water heat stores with stratification. *Renewable Energy, 28*, 699–711.

Mettawee, E., & Assassa, G. (2006). Experimental study of a compact PCM solar collector. *Energy, 31*(14), 2958-2968.

Mettawee, E., & Assassa, G. (2007). Thermal conductivity enhancement in a latent heat storage system. *Solar Energy, 81*(7), 839-845.

Murray, R., Desgrosseilliers, L., Stewart, J., Osbourne, N., Marin, G., Safatli, A., Groulx, D., & White, M. A. (2011). *Design of a latent heat energy storage system coupled with a domestic hot water solar thermal system.* Paper presented at the World Renewable Energy Congress, Linköping, Sweden.

Murray, R., & Groulx, D. (2011). *Modeling convection during melting of a phase change material.* Paper presented at the COMSOL Conference October 2011, Boston.

Nagano. (2004). *Experiments on fin-effects for increasing heat transfer coefficients during charging heat and heat release between PCMs and thermal medium*. Paper presented at the IEA annex 17 workshop

Natural-Resources-Canada. (2012). Photovoltaic potential and solar resource maps of Canada. from http://pv.nrcan.gc.ca/, Ottawa

Ogoh, W., & Groulx, D. (2010). *Thermal behavior of phase change material during charging inside a finned cylindrical latent heat energy storage system: Effects of the arrangement and number of fins* Paper presented at the Proceedings of the International Heat Transfer Conference.

Ogoh, W., & Groulx, D. (2012). Effects of the heat transfer fluid velocity on the storage characteristics of a cylindrical latent heat energy storage system: a numerical study. *Heat Mass Transfer 48*, 439–449

Rabin, Y., Bar-Niv, I., Korin, E., & Mikic, B. (1995). Integrated solar collector storage system based on a salt-hydrate phase change material. *Solar Energy, 55*(6), 435-444.

Regin, A., Solanki, S., & Saini, J. (2006). Latent heat thermal energy storage using cylindrical capsule: Numerical and experimental investigations. *Renewable Energy, 31*(13), 2025-2041.

Regin, A. F., Solanki, S. C., & Saini, J. S. (2008). Heat transfer characteristics of thermal energy storage system using PCM capsules: A review. *Renewable and Sustainable Energy Reviews, 12*(9), 2438-2458.

Sarı, A., & Kaygusuz, K. (2002). Thermal and heat transfer characteristics in a latent heat storage system using lauric acid. *Energy Conversion and Management, 43*, 2493–2507.

Sasaguchi, K., Yoshida, M., & Nakashima, S. (1990). Heat transfer characteristics of a latent heat thermal energy storage unit worth a finned tube; Effect of fin configuration. *Journal Name: Heat Transfer - Japanese Research; (USA); Journal Volume: 19:1*, Pages: 11-27.

Seeniraj, R. V., & Lakshmi Narasimhan, N. (2008). Performance enhancement of a solar dynamic LHTS module having both fins and multiple PCMs. *Solar Energy, 82*(6), 535-542.

Sharma, A., Tyagi, V., Chen, C., & Buddhi, D. (2009). Review on thermal energy storage with phase change materials and applications. *Renewable and Sustainable Energy Reviews, 13*(2), 318-345.

Shatikian, V., Ziskind, G., & Letan, R. (2008). Numerical investigation of a PCM-based heat sink with internal fins: Constant heat flux. *International Journal of Heat and Mass Transfer, 51*(5-6), 1488-1493.

Shukla, A., Buddhi, D., & Sawhney, R. L. (2009). Solar water heaters with phase change material thermal energy storage medium: A review. *Renewable and Sustainable Energy Reviews, 13*(8), 2119-2125.

Stritih, U. (2003). Heat transfer enhancement in latent heat thermal storage system for buildings. *Energy and Buildings, 35*(11), 1097-1104.

Stritih, U. (2004). An experimental study of enhanced heat transfer in rectangular PCM thermal storage. *International Journal of Heat and Mass Transfer, 47*(12-13), 2841-2847.

Thermo-Dynamics-Ltd. (2011). Thermo Dynamics Ltd, S Series Solar Collectors Technical Specifications Data Sheet http://www.thermo-dynamics.com/ Thermo Dynamics Ltd.

Trp, A., Lenic, K., & Frankovic, B. (2006). Analysis of the influence of operating conditions and geometric parameters on heat transfer in water-paraffin shell-and-tube latent thermal energy storage unit. *Applied Thermal Engineering, 26*(16), 1830-1839.

Velraj, R., Seeniraj, R. V., Hafner, B., Faber, C., & Schwarzer, K. (1998). Heat transfer enhancement in a latent heat storage system. *Solar Energy, 65*(3), 171-180.

Zalba, B., Sánchez-Valverde, B., & Marín, J. (2005). An experimental study of thermal energy storage with phase change materials by design of experiments. *Journal of Applied Statistics, 32*(4), 321-332.

Zhang, Y., & Faghri, A. (1995). Heat transfer enhancement in latent heat thermal energy storage system by using the internally finned tube. *Inr J Heat Mass Transfer, 39*(15), 3165-3173.

Zivkovic, B., & Fujii, I. (2001). An analysis of isothermal phase change of phase change material within rectangular and cylindrical containers *Solar Energy, 70*(1), 51–61.

# Appendix A: Calibration of Thermocouples

To calibrate the thermocouples, the procedure given in the User's Guide (ftp://ftp.hartscientific.com/manuals/7102.pdf) for the Alpha FLUKE 7102 micro-was used. The "Thermocouple Calibration Module" in LabVIEW was used to create a correction factor for the thermocouples over the range of temperatures expected. To check the accuracy of the correction factor, Fig. A.1 shows temperature points recorded after the T16-T19 thermocouples were calibrated. The uncertainty of the thermocouples used in the thesis is the largest difference between the actual and the measured temperature.

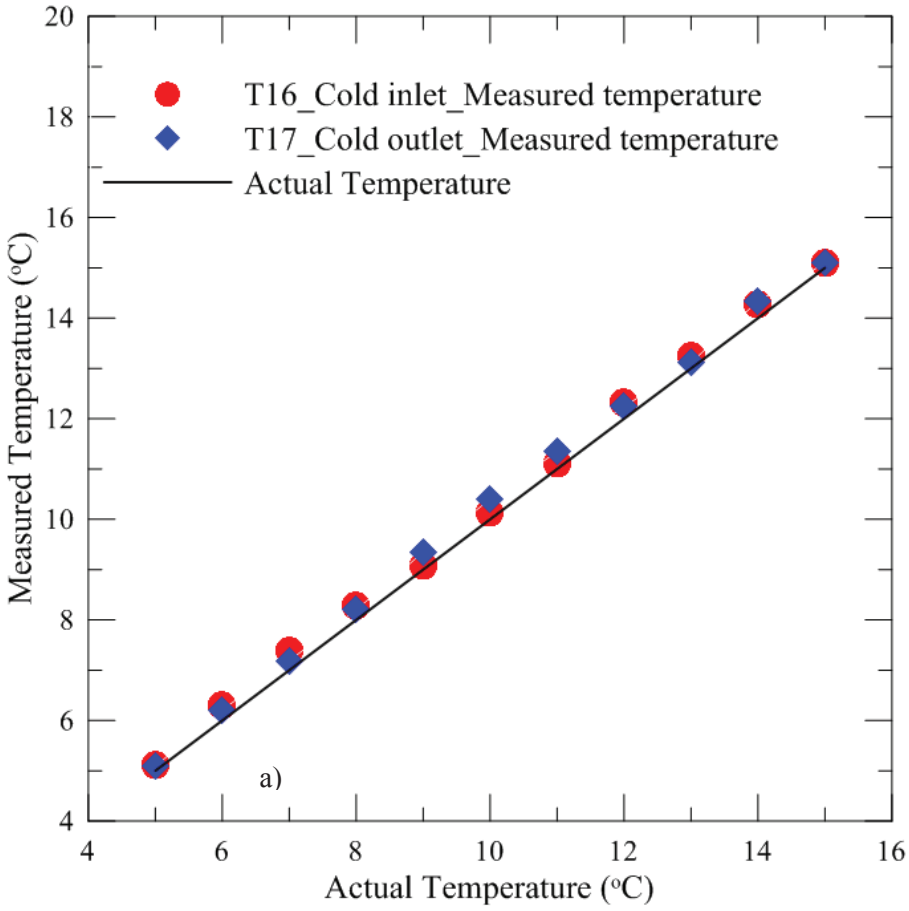


**Figure A.1: Recorded vs. actual temperature points for T16 and T17**

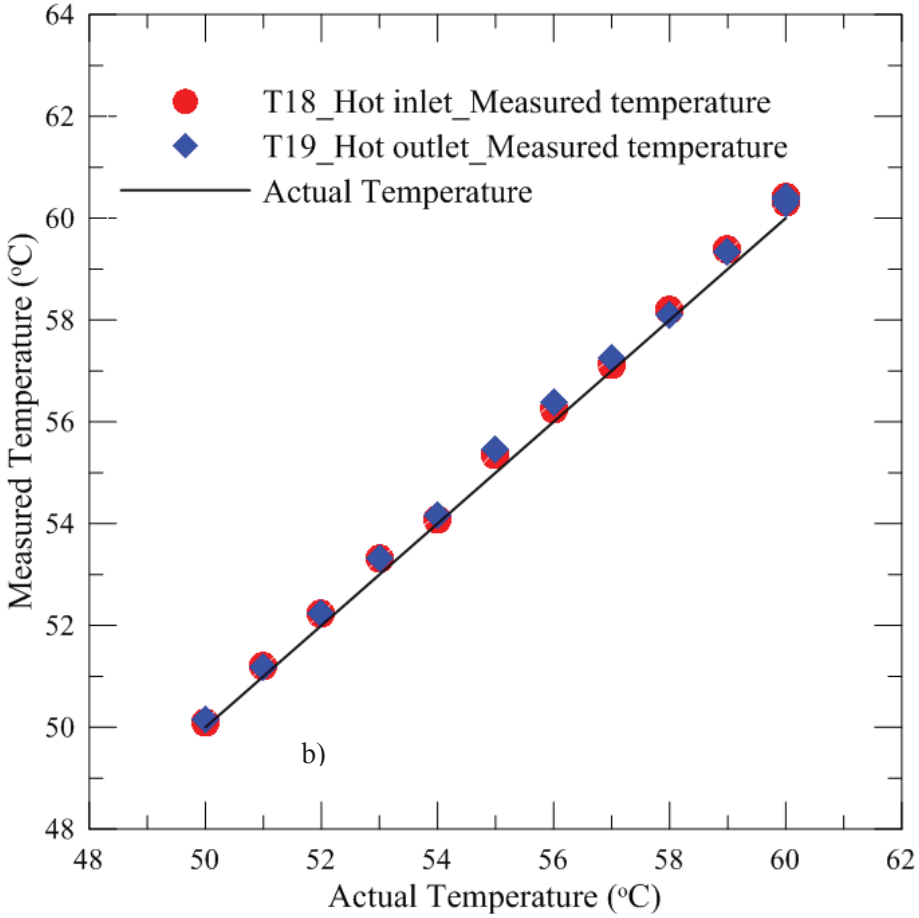


**Figure A.2: Recorded vs. actual temperature points for T18 and T19**

## Appendix B: Sizing the Pump

The inlet hot water velocity was varied during experimentation, but using a value on the high end of the spectrum of 0.5 m/s gives a Reynolds number of 318,000. To calculate the friction head, the following equation was used:

$$H_f = \frac{f\,V^2 L}{2\,d\,g}. \tag{B.1}$$

To calculate the minor head losses, a sum of the loss coefficients (k) was used in the following equation:

$$H_m = \frac{\sum k\,V^2}{2\,g}. \tag{B.2}$$

The values given in Table B-1 were used to calculate the desired head for the pump.

**Table B.1: Sizing the hot water pump**

| | |
|---|---|
| Pipe Length | 2 m |
| Pipe Diameter | 0.0127 m |
| Water velocity | 0.5 m/s |
| Water Viscosity | 1.0 $E^{-5}$ Pas |
| Water Density | 1.0 $E^{3}$ kg/$m^{3}$ |
| Roughness | 1.5 $E^{-6}$ m * |
| Friction Factor | 0.015 * |
| Total Friction Head | 0.12 m |
| Number of 90 degree angles | 2 |
| Number of Valves | 2 |
| Sum of Loss Coefficients | 5.3 * |
| Total Minor Losses | 0.27 m |
| Total Height Change | 1 m |
| *Total Head Loss* | *4.51m* |

* (F. Incropera et al., 2007)

Cole Parmer model EW-72012-10 circulator was chosen, which has a maximum head of 11 m, and maximum flow rate of 17 L/min. This is larger than the flow rates used in this experiment to represent a SDHW system, however this leaves the option of charging the system faster.

## Appendix C: Circuit Diagram for Flow Meters

Figure C.1 shows the circuit diagram used for the flow meter:

*NEW MODEL*

OMEGA
An OMEGA Technologies Company

# INSTALLATION INSTRUCTIONS
## Of Hall Effect Flow Meter

### FLOW METER INSTALLATION

1. Make sure that the inside of the pipes are totally clean.
2. Install Water Meter with union connection.
3. Make sure flow direction of water corresponds with flow indicator arrow on flow meter housing.

### ELECTRICAL CONNECTION TO HALL EFFECT

1. Make wiring connection as indicated on diagram below.
2. Please note: 3,5 V < $U_B$ < 20 V $I_{out}$ max. = 20 mA
3. The pull-up-resistor R should be a min. of 1 k ohms. On installation without C a value of 10 k ohms is recommended. In case of clicking disturbances due to the contactor (e.g. radiowave receivers being in the area) a wiring with C= 4,7 nF and R ≥ 1 k ohms should be used.

**Electrical Connection Diagram** **Impulse Counter**

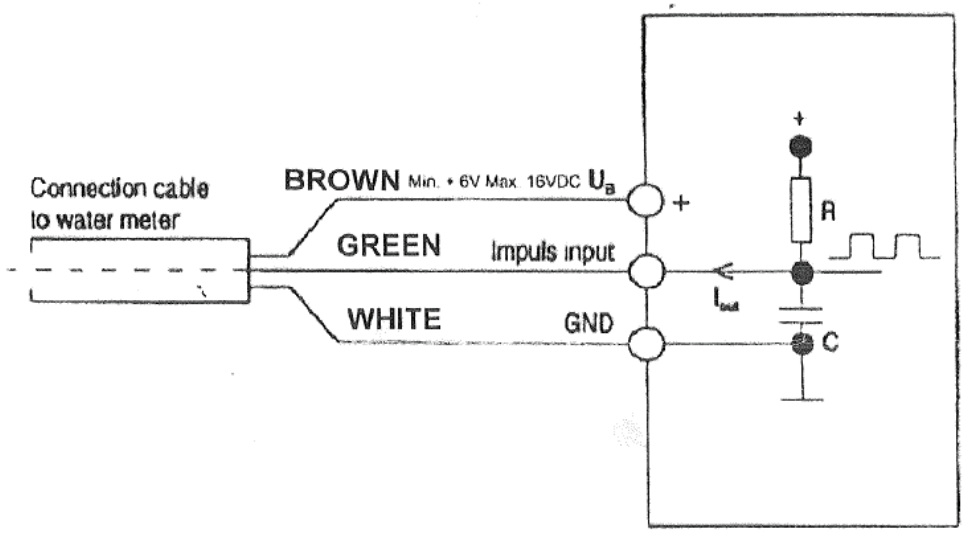


**Figure C.1: Circuit diagram used for flow meters**

# Appendix D: Additional Experimental Results

Temperature profiles for additional simultaneous charging/discharging experiments are presented in Appendix D. The energy input and recovered for these experiments is discussed in Section 6.3. Figures D.1 to D.8 show the results for experiments with the PCM initially melted, and Figures D.9 to D.16 show the results for experiments with the PCM initially solid.

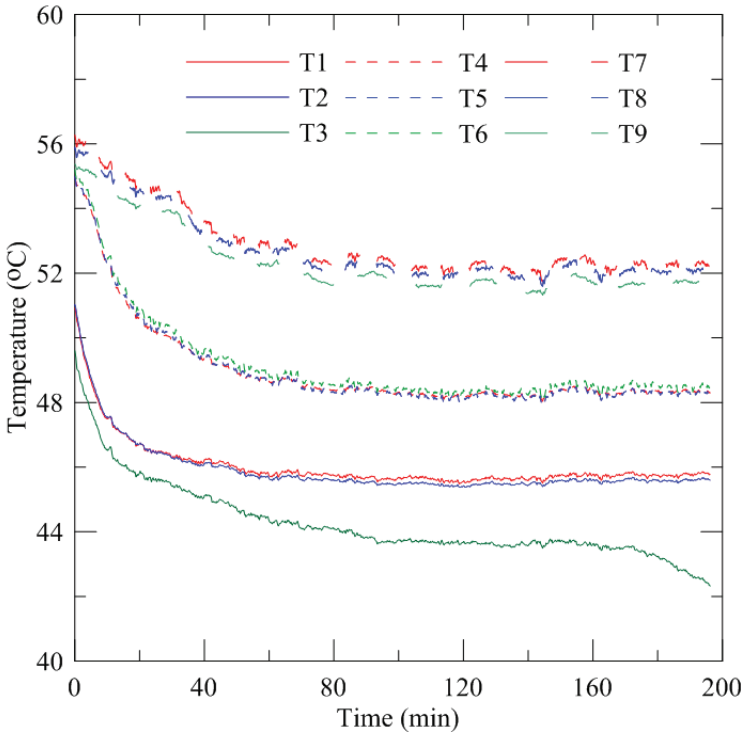


**Figure D.1: 10 minutes of simultaneous charging (2.75 L/min) and discharging followed by 20 minutes of charging only (20 L/min), initially melted PCM**

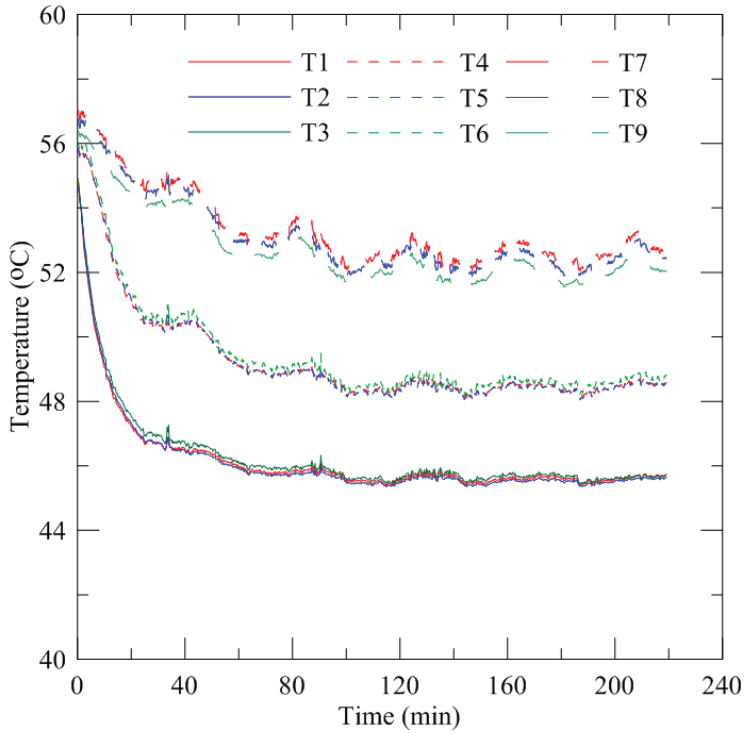


**Figure D.2: 10 minutes of simultaneous charging (2.75 L/min) and discharging followed by 30 minutes of charging only (20 L/min), initially melted PCM**

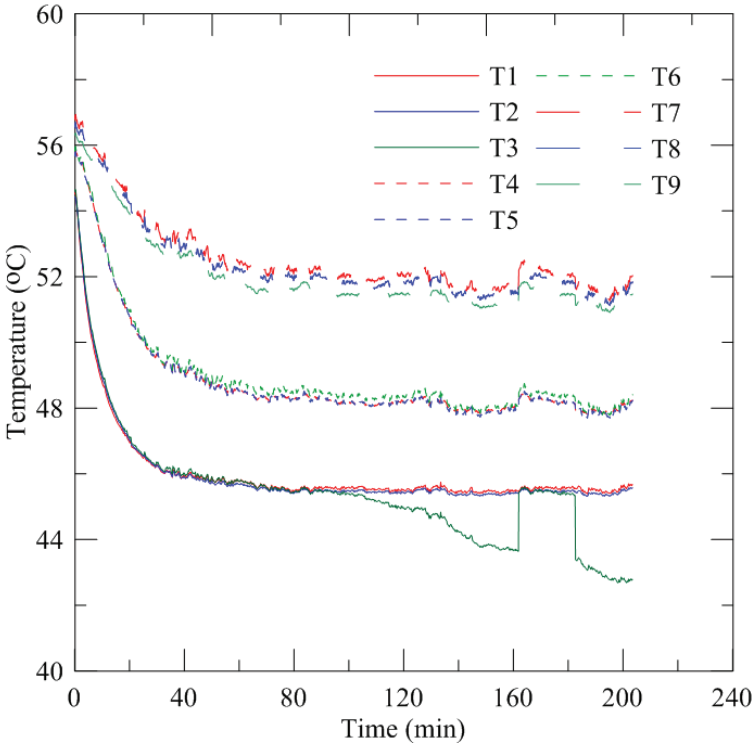


**Figure D.3: 20 minutes of simultaneous charging (2.75 L/min) and discharging followed by 20 minutes of charging only (20 L/min), initially melted PCM**

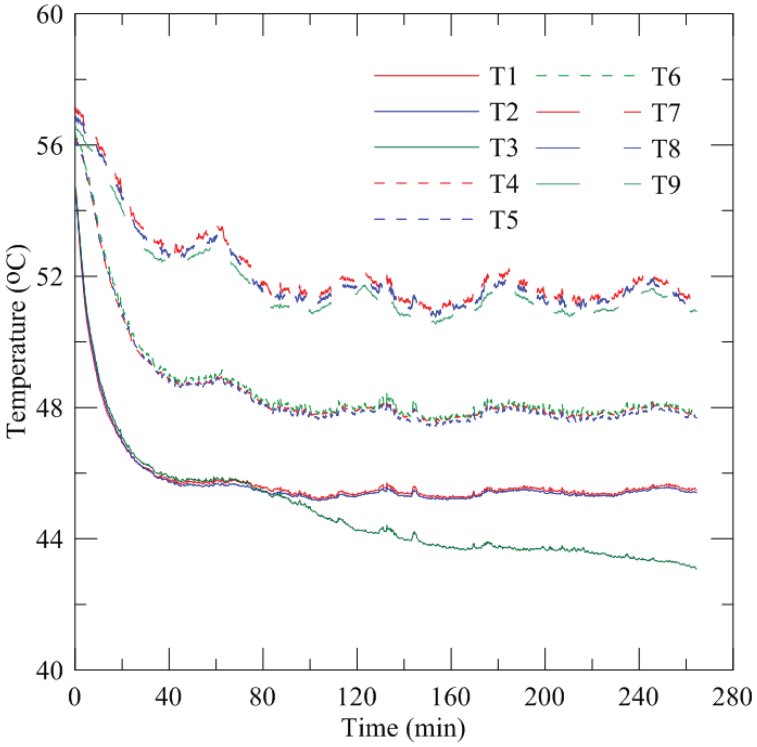


**Figure D.4: 20 minutes of simultaneous charging (2.75 L/min) and discharging followed by 40 minutes of charging only (20 L/min), initially melted PCM**

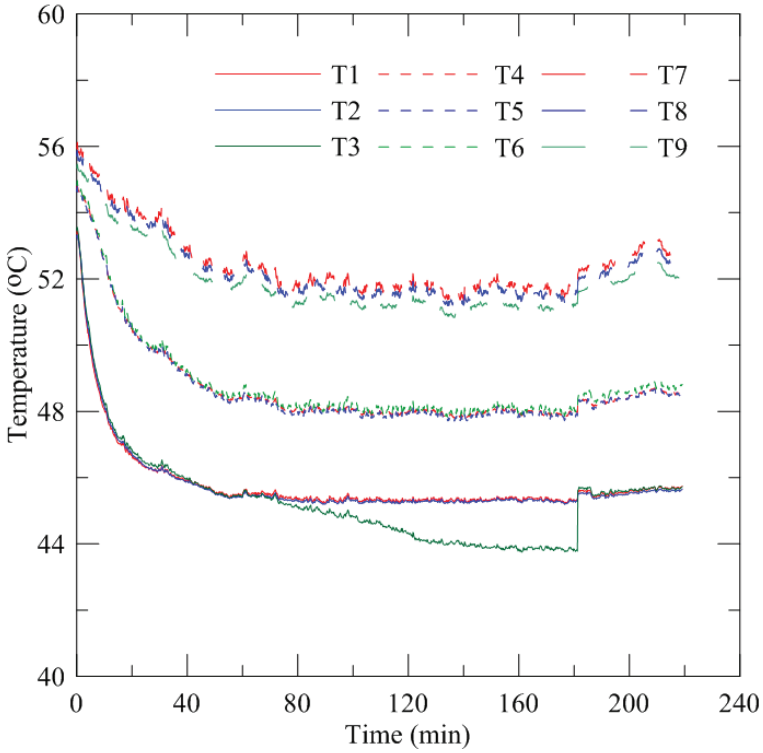


**Figure D.5: 10 minutes of simultaneous charging (2.75 L/min) and discharging followed by 20 minutes of charging only (5 L/min), initially melted PCM**

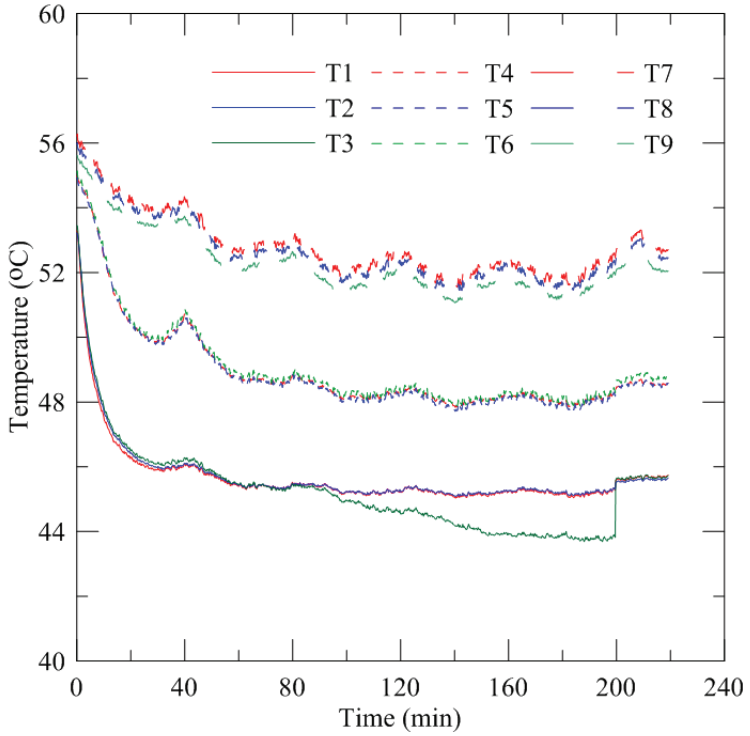


**Figure D.6: 10 minutes of simultaneous charging (2.75 L/min) and discharging followed by 30 minutes of charging only (5 L/min), initially melted PCM**

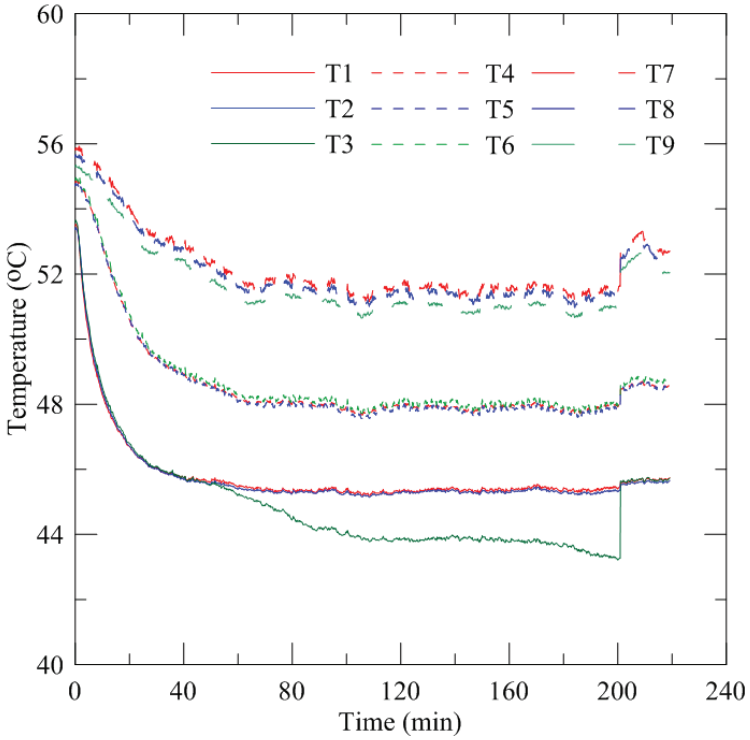


**Figure D.7: 20 minutes of simultaneous charging (2.75 L/min) and discharging followed by 20 minutes of charging only (5 L/min), initially melted PCM**

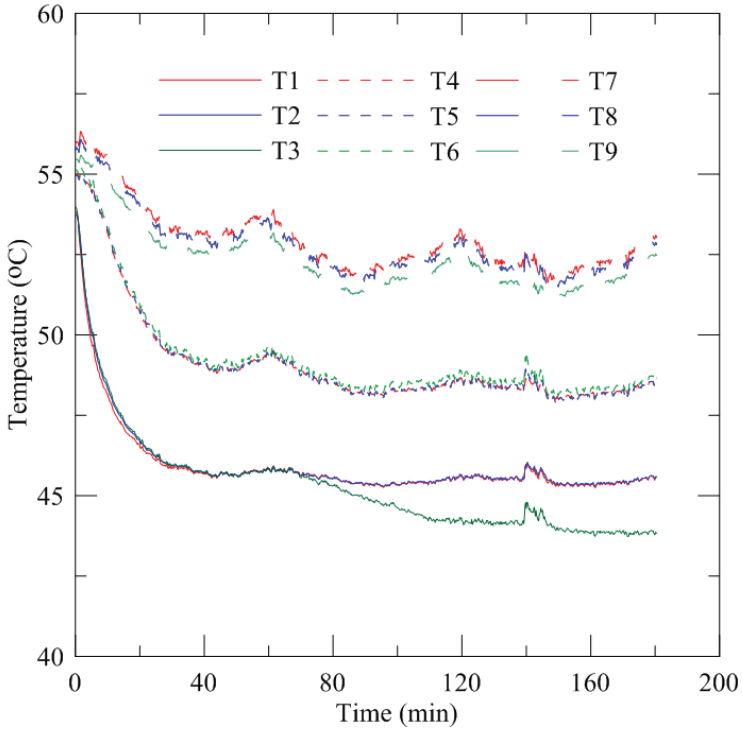


**Figure D.8: 20 minutes of simultaneous charging (2.75 L/min) and discharging followed by 40 minutes of charging only (5 L/min), initially melted PCM**

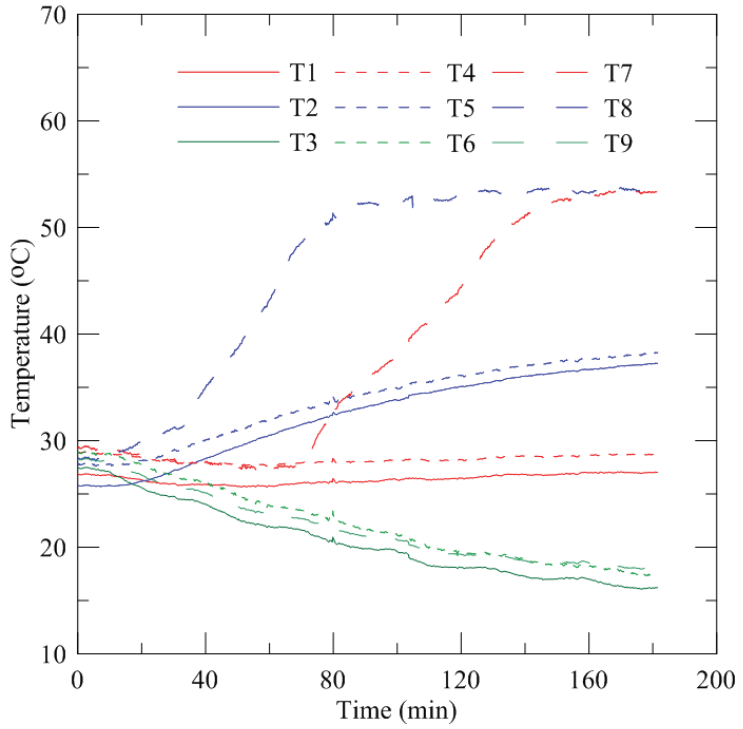


**Figure D.9: 10 minutes of simultaneous charging (2.75 L/min) and discharging followed by 20 minutes of charging only (20 L/min), initially solid PCM**

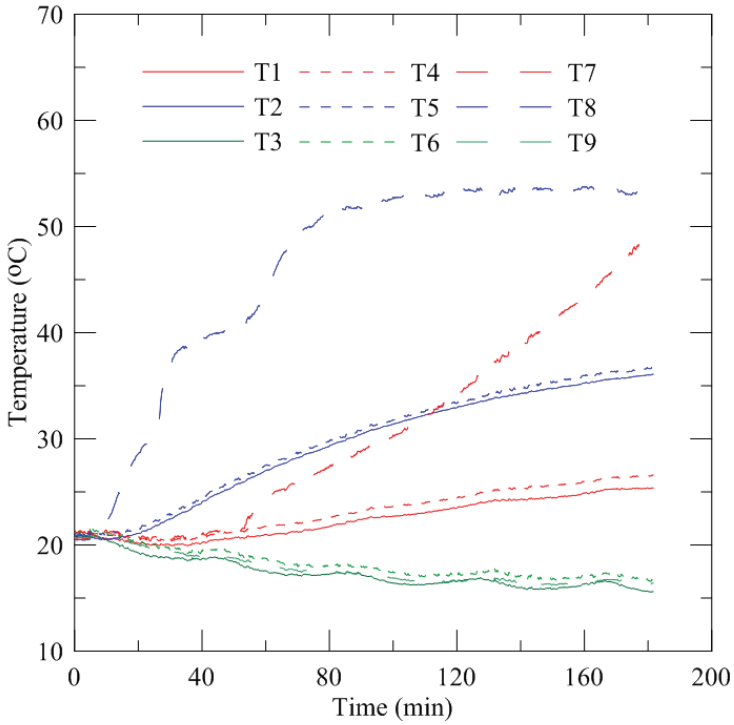


**Figure D.10: 10 minutes of simultaneous charging (2.75 L/min) and discharging followed by 30 minutes of charging only (20 L/min), initially solid PCM**

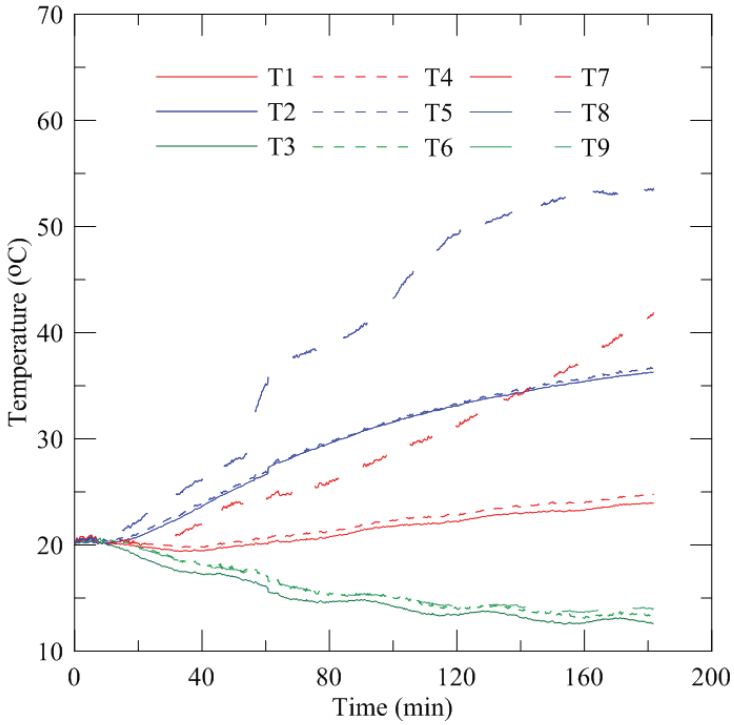


**Figure D.11: 20 minutes of simultaneous charging (2.75 L/min) and discharging followed by 20 minutes of charging only (20 L/min), initially solid PCM**

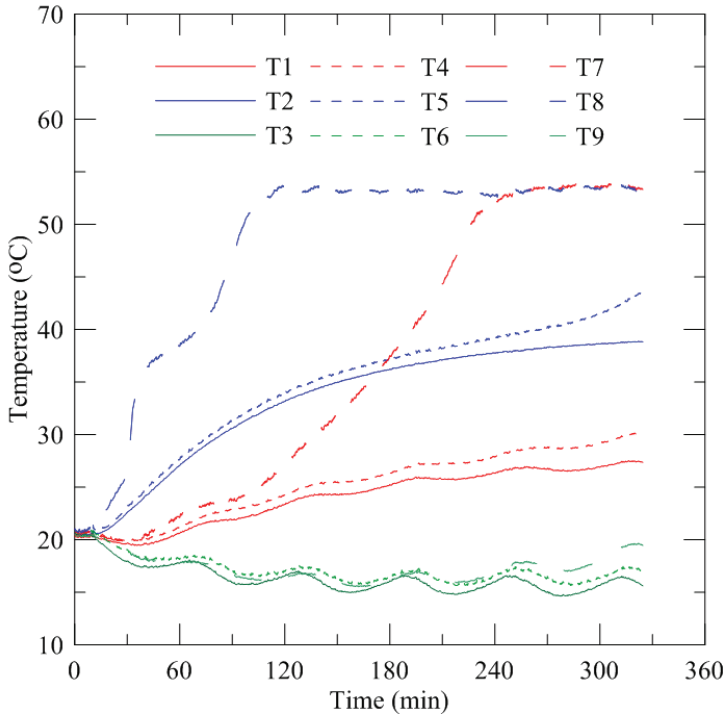


**Figure D.12: 20 minutes of simultaneous charging (2.75 L/min) and discharging followed by 40 minutes of charging only (20 L/min), initially solid PCM**

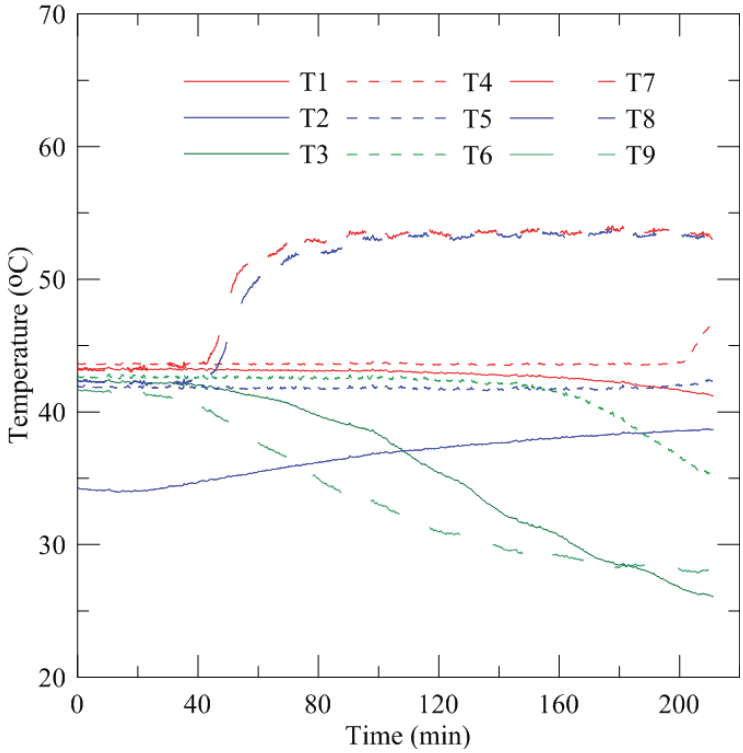


**Figure D.13: 10 minutes of simultaneous charging (2.75 L/min) and discharging followed by 20 minutes of charging only (5 L/min), initially solid PCM**

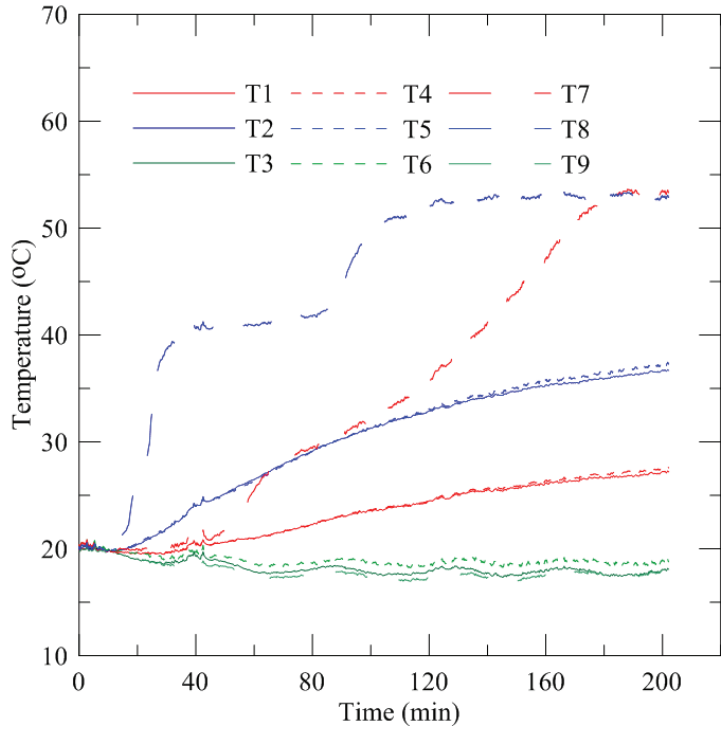


**Figure D.14: 10 minutes of simultaneous charging (2.75 L/min) and discharging followed by 30 minutes of charging only (5 L/min), initially solid PCM**

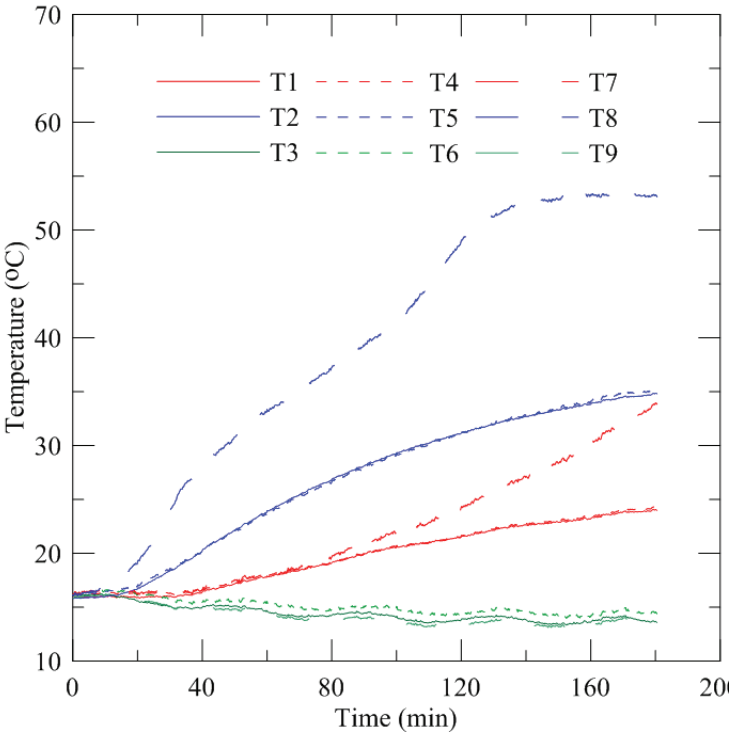


**Figure D.15: 20 minutes of simultaneous charging (2.75 L/min) and discharging followed by 20 minutes of charging only (5 L/min), initially solid PCM**

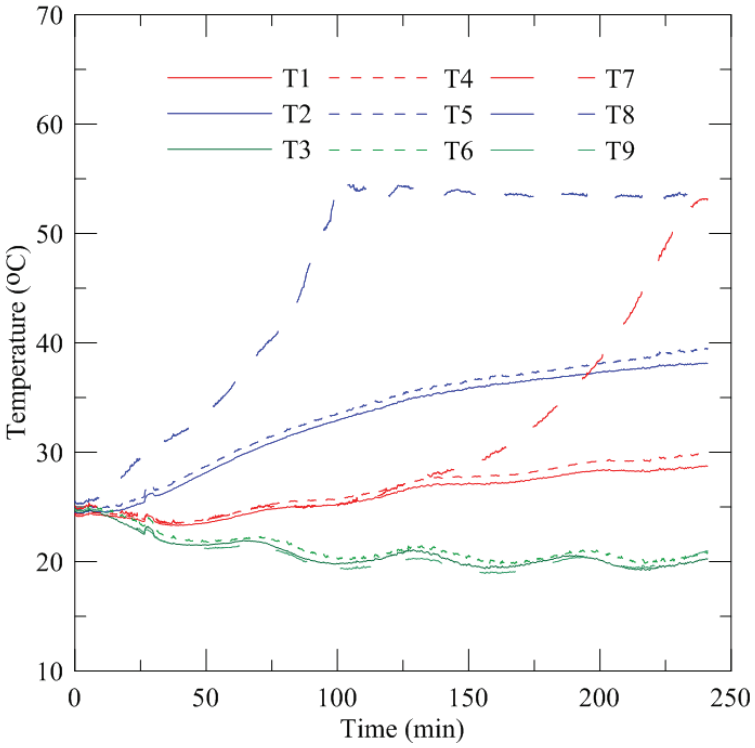


**Figure D.16: 20 minutes of simultaneous charging (2.75 L/min) and discharging followed by 40 minutes of charging only (5 L/min), initially solid PCM**

# Appendix E: Example Uncertainty Calculation

Table E.1 shows the values used in the example energy and uncertainty equations presented in Appendix E.

**Table E.1: Values used in uncertainty calculations (first row in Table E.2)**

| Parameter | Value in first 10 s time interval during charging |
|---|---|
| $t$ | 10 s |
| $\dot{m}$ | $\frac{0.56\ {}^{\mathrm{L}}/_{\mathrm{min}} * 983\ \mathrm{kg/m^3}}{60\ \mathrm{s} * 1000 \mathrm{kg/m^3}} = 0.009\ \mathrm{kg/s}$ |
| $Cp_{water}$ | 4.18 kJ/kgK |
| $\Delta T$ | 4.79 °C |
| $\delta_{T18}$ | ± 0.45 °C |
| $\delta_{T19}$ | ± 0.45 °C |
| $\delta_{\dot{m}}$ | ± 2% of reading = ± 0.00019 kg/s |

Energy input by hot HTF for first 10 s time interval:

$$Q = t\dot{m}Cp_{water}\Delta T = 10\left(\frac{0.56}{60}\right)(4.18)(4.79) = 1.84\ \mathrm{kJ}$$

Uncertainty in the energy calculation for first 10 s time interval:

$$\delta_{Qinput} = tCp_{water}\sqrt{(\Delta T\delta_{\dot{m}})^2 + (-\dot{m}\delta_{T18})^2 + (\dot{m}\delta_{T19})^2} =$$

$$(10 * 4.18)\sqrt{(4.79 * 0.00019)^2 + \left(-\frac{0.56}{60} * 0.45\right)^2 + \left(\frac{0.56}{60} * 0.45\right)^2} = 0.25\ \mathrm{kJ}$$

Total energy input for first 10 s time interval (including uncertainty):

$$Q = t\dot{m}Cp_{water}\Delta T \pm \delta_{\dot{Q}} = 1.84 \pm 0.25\ \mathrm{kJ}$$

Percent uncertainty in energy input for first 10s time interval:

$$\%\ \delta_{Qinput} = 100\left(\frac{\delta_{\dot{Q}}}{Q}\right) = 100\left(\frac{0.25}{1.84}\right) = 13.4\ \%$$

Table E.2 shows an example of the uncertainty calculations done for the charging experiment presented in Section 5.4. Row 1 shows the results presented in the example calculations shown on Page 136.

**Table E.2: Example uncertainty calculations**

| Time $t$ (hours) | Hot flow rate $\dot{m}$ (L/min) | $\Delta T$ (T18-T19) | Energy (kJ) Eq. (4.2) | Uncertainty in Energy (kJ) Eq. (4.8) | Accumulated Energy (kJ) | Accumulated Uncertainty (kJ) |
|---|---|---|---|---|---|---|
| 0.000 | 0.56 | 4.79 | 1.84 | 0.25 | 1.84 | 0.248 |
| 0.003 | 0.55 | 5.48 | 2.08 | 0.25 | 3.92 | 0.493 |
| 0.006 | 0.54 | 16.54 | 6.07 | 0.26 | 10.00 | 0.757 |
| 0.008 | 0.54 | 16.39 | 6.04 | 0.26 | 16.04 | 1.020 |
| 0.011 | 0.55 | 14.50 | 5.42 | 0.26 | 21.46 | 1.282 |
| 0.014 | 0.54 | 14.16 | 5.22 | 0.26 | 26.68 | 1.539 |
| 0.017 | 0.54 | 12.96 | 4.79 | 0.25 | 31.46 | 1.792 |
| 0.019 | 0.54 | 11.89 | 4.39 | 0.25 | 35.85 | 2.043 |
| 0.022 | 0.54 | 11.64 | 4.27 | 0.25 | 40.12 | 2.292 |
| 0.025 | 0.55 | 9.74 | 3.64 | 0.25 | 43.77 | 2.541 |
| 0.028 | 0.55 | 8.93 | 3.36 | 0.25 | 47.13 | 2.790 |
| 0.031 | 0.54 | 8.37 | 3.10 | 0.24 | 50.23 | 3.033 |
| 0.033 | 0.54 | 7.75 | 2.86 | 0.24 | 53.09 | 3.275 |
| 0.036 | 0.54 | 7.52 | 2.78 | 0.24 | 55.87 | 3.517 |
| 0.039 | 0.54 | 6.85 | 2.53 | 0.24 | 58.40 | 3.757 |
| 0.042 | 0.54 | 6.63 | 2.46 | 0.24 | 60.86 | 3.998 |
| 0.044 | 0.54 | 6.06 | 2.26 | 0.24 | 63.12 | 4.240 |
| 0.047 | 0.54 | 6.16 | 2.30 | 0.24 | 65.42 | 4.482 |
| 0.050 | 0.54 | 5.67 | 2.09 | 0.24 | 67.51 | 4.720 |
| 0.053 | 0.55 | 5.77 | 2.16 | 0.24 | 69.67 | 4.963 |
| 0.056 | 0.55 | 5.38 | 2.03 | 0.24 | 71.70 | 5.206 |
| 0.058 | 0.55 | 5.42 | 2.04 | 0.24 | 73.74 | 5.448 |
| 0.061 | 0.54 | 5.07 | 1.89 | 0.24 | 75.62 | 5.688 |
| 0.064 | 0.55 | 5.20 | 1.96 | 0.24 | 77.58 | 5.931 |
| 0.067 | 0.55 | 4.90 | 1.83 | 0.24 | 79.42 | 6.172 |
| 0.069 | 0.54 | 4.60 | 1.71 | 0.24 | 81.13 | 6.412 |
| 0.072 | 0.55 | 4.65 | 1.76 | 0.24 | 82.89 | 6.655 |
| 0.075 | 0.55 | 4.51 | 1.71 | 0.24 | 84.60 | 6.899 |

In the first 5 minutes of the charging experiment (shown in Table E.1) the temperature difference, $\Delta T$, is large, resulting in less uncertainty than later in the experiment.